SAND96-2820
Unlimited Release
Printed June 1997

Distribution
Category UC-814

Development and Experimental Evaluation of Models for Low Capillary Number Two-Phase Flows in Rough Walled Fractures Relevant to Natural Gradient Conditions

Robert J. Glass
Sandia National Laboratories
Geohydrology Department
Albuquerque, NM 87185

Michael J. Nicholl
School of Geology
Oklahoma State University
Stillwater, OK 74078

Lane Yarrington
Sandia National Laboratories
Environmental Risk & Decision Analysis Department
Albuquerque, NM 87185

ABSTRACT

The major results from SNL's Conceptual Model Development and Validation Task (WBS 1.2.5.4.6) as developed through exploration of small scale processes were synthesized in Glass et al. (1996) to give guidance to Performance Assessment on improving conceptual models for isothermal flow in unsaturated, fractured rock. There, pressure saturation and relative permeability curves for single fractures were proposed to be a function of both fracture orientation within the gravity field and initial conditions. We refer the reader to Glass et al. (1996) for a discussion of the implications of this behavior for Performance Assessment. The scientific research we report here substantiates this proposed behavior. We address the modeling of phase structure within fractures under natural gradient conditions relevant to unsaturated flow through fractures. This phase structure underlies the calculation of effective properties for individual fractures and hence fracture networks as required for Performance Assessment.

Standard Percolation (SP) and Invasion Percolation (IP) approaches have been recently proposed to model the underlying phase saturation structures within individual fractures during conditions of two-phase flow. Subsequent analysis of these structures yields effective two-phase pressure-saturation and relative permeability relations for the fracture. However, both of these approaches yield structures that are at odds with physical reality as we see in experiments and thus effective properties calculated from these structures are in error. Here we develop and evaluate a Modified Invasion Percolation (MIP) approach to better model quasi-static immiscible displacement in fractures. The effects of gravity, contact angle, local aperture field geometry, and local in-plane

interfacial curvature between phases are included in the calculation of invasion pressure for individual sites in a discretized aperture field. This pressure controls the choice of which aperture is invaded during the displacement process, and thus the growth of phase saturation structure within the fracture. Inclusion of gravity yields the formation of gravity-driven fingers in non-horizontal fractures. In-plane interfacial curvature, which is neglected in SP and IP modeling approaches, greatly affects the phase invasion structure in both horizontal and non-horizontal fractures causing the formation of macroscopic fronts. Comparison to all experimental data available at this time substantiates MIP, while invalidating IP and SP approaches applied to fractures.

ACKNOWLEDGMENTS

This work was supported in part by the U.S. Department of Energy, Office of Civilian Radioactive Waste Management, Yucca Mountain Site Characterization Project Office, under contract DE-AC04-94AL85000, WBS 1.2.5.4.6, WA-0040, Revision 2. All data referenced in this report are non-qualified. The data are archived under DTN SNL19011590002.002. We also gratefully acknowledge the support of the U.S. Department of Energy's Basic Energy Research Geoscience Program to complete the MIP model development. Finally we thank Vince Tidwell, Steve Webb and Peter Davies for their constructive criticism of the paper during internal review.

CONTENTS

FIGURES

1. INTRODUCTION

The flow and transport characteristics of individual saturated fractures within a fractured rock mass are controlled by the fracture geometry at the aperture scale. However, for two-phase immiscible fluid flow under conditions where viscous forces are small with respect to capillary forces (small capillary number, quasi-static), phase saturation geometry (or structure) within the fracture ultimately controls the permeability to each phase, fluid pressure/saturation relations, and solute dispersion within each phase. Fracture phase saturation structure also controls flow and transport into and through the surrounding rock by affecting hydraulic contact between the fracture and the rock matrix. Macroscopic effective properties that purport to describe the pressure-saturation, relative permeability, solute dispersivity and fracture-matrix interaction behavior of single fractures must be considered as a function of phase structure. Therefore, we must address the fundamental controls on phase structure within rough-walled fractures.

Using an approach based on Standard Percolation (SP) to determine phase structure with pressure, two-phase pressure-saturation and relative permeability relations for single horizontal fractures have been constructed numerically (e.g., Pyrak-Nolte et al., 1990; Pruess and Tsang, 1990). In this approach, the local aperture within the simulated fracture aperture field (often spatially correlated) entirely determines whether it is filled with the wetting or nonwetting phase at a given pressure. This approach for determining phase structure has been assumed relevant to low capillary number flows where viscous forces are negligible (e.g., mobilization of entrapped phase ganglia does not occur). Results of the SP approach suggest the importance of phase interference and trapping due to the two-dimensional nature of the aperture network. However, the mechanism underlying SP determination of the phase saturation structure requires all apertures to be in a state of mutual communication and at equilibrium within the system. Three communication processes exist: flow through the matrix which connects all apertures, film flow along the fracture walls, and diffusion processes. To satisfy equilibrium, time scales must be long with respect to that of the slowest communication process. For a large number of situations, either communication processes do not exist or phase displacement occurs rapidly with respect to them but still under quasi-static conditions where viscous forces are negligible. For these situations, accessibility of apertures to a phase, i.e. adjacency of an aperture to a phase and connection within that phase to a source or sink, places an additional control on phase displacement geometry. Models which incorporate such accessibility rules for application to low capillary number flows have been termed Invasion Percolation (IP) after the work of Wilkinson and Willemsen (1983). A form of IP has been applied to spatially correlated aperture fields by Kwicklis and Healy (1993) and by Mendoza (1992) to calculate pressure-saturation and relative permeability relations for fractures.

However, either with or without accessibility rules, these approaches do not reproduce either the qualitative or quantitative character of our experimentally measured phase structures obtained in analog fractures under small capillary number conditions. Our experiments have demonstrated macroscopic fronts, decreased phase entrapment on invasion, depressed wetting phase capillary rise, macroscopic gravity driven fingers, and compact clusters during dissolution (Nicholl et al., 1992, 1993a,b, 1994; Nicholl and Glass, 1994; Glass and Nicholl, 1995a,b). These experimental observations emphasize the importance of gravity and an interfacial smoothing mechanism that reduces the interfacial area between phases and its complication.

As a first step to incorporate these experimental observations, Glass (1993) included both gravity and the second principle radius of curvature at the phase/phase interface given by the local in-plane curvature (normal to the local aperture induced curvature) into a Modified Invasion Percolation (MIP) model. The simulations showed reasonable qualitative and quantitative agreement for the gravity-driven finger widths measured in the experiments of Nicholl et al. (1993a). However, the simplistic conceptual model used for determining in-plane curvature created artificially blocky structures oriented in the directions of the regular grid.

Here, we present a numerical implementation of MIP for fractures that includes a more versatile conceptual model for in-plane curvature than proposed previously. We apply the model to situations where we have data on phase structure from a wide variety of air-water invasion experiments (both horizontal and vertical orientations) performed within a single impermeable, analog rough-walled fracture. We consider only the measured aperture field where these experiments were conducted; however, we vary systematically the fluid/fluid/solid contact angle in order to demonstrate the constrained influence of in-plane versus aperture induced capillary forces. In vertical orientations, both gravity stabilized (water invasion from below, air invasion from above) and destabilized (water invasion from above, air invasion from below) are explored.

Comparison of SP, IP and MIP within the measured aperture field of the analog fracture shows both substantial qualitative and quantitative differences. Furthermore, comparison to experimental data substantiates MIP while invalidating IP and SP approaches for modeling phase invasion processes in our analog fracture. The combination of in-plane curvature and gravity allows us to model the macroscopic fronts, decreased phase entrapment on wetting invasion, depressed wetting phase capillary rise, macroscopic gravity driven fingers, and compact clusters during dissolution that we have found in our experiments. In addition, the importance of in-plane curvature in creating hysteretic response of the fracture is demonstrated. This in-plane curvature induced hysteresis may be the single largest cause of hysteresis in fractures and forms an hypothesized system behavior that could be tested experimentally in the future.

2. CONCEPTUAL MODEL DEVELOPMENT

Analysis of slow, quasi-static phase invasion experiments in both horizontal and non-horizontal, statistically isotropic, analog rough walled fractures (**see figure 1**) demonstrates that the invading fluid advances through the aperture network in a series of discrete "haines jumps" along the fluid/fluid interface. In horizontal fractures, this leads to directionally independent invading phase advance that entraps defending phase at the invasion front and eventually spans the fracture in all directions. In non-horizontal fractures where the denser phase invades from the top of the system, gravity-driven fingers form as the front advances causing the fracture to be spanned only in the direction of gravity unless the fracture width is less than the finger width. For gravity-driven fingers, after the front has reached a length in the gravity field given by the difference between the nonwetting and wetting fluid entry values of the hysteretic pressure potential/saturation relation (Nicholl et al., 1993a), some apertures along the interface above the advancing finger tip are re-invaded by the original defending phase. Re-invasion behind the invasion tip at this distance demonstrates that pressure within the finger is hydrostatic, gravity creates a "hanging column" or siphon within the finger.

Based on these observations, we hypothesize that growth of the invading phase under quasi-static conditions can be modeled simply by advancing the interface step by step, always choosing the invasion location to be where the combined influence of capillary and gravity forces are strongest. For this situation, a *modified* form of invasion percolation should apply.

2.1 Invasion Percolation (IP) and Modified Invasion Percolation (MIP)

Invasion Percolation (IP), introduced by Wilkinson and Willemsen (1983), models phase invasion on a network where the pressure within each phase does not vary in space. This is a reasonable assumption in the limit of infinitesimal flow rate (quasi-static) where viscous forces are negligible and the system is dominated by capillary forces (i.e., small capillary number). Invasion percolation is essentially a simplified form of the pore-scale models developed in the petroleum engineering field (e.g., Fatt, 1956; Chatzis and Dullien, 1977) that allows application to much larger networks (10^4 and greater pores).

Invasion percolation is implemented on a pore network of given connectivity with each pore given a probability of invasion. Selected pores are filled with the invading phase at the boundary surface, often either an edge of a rectangular network or a disk at the center. All pores connected to the invaded phase are available for invasion. The one with the highest assigned probability of invasion is found and invaded. This modifies the list of pores available for invasion, which is sorted to find the next pore with the highest assigned probability of invasion, and so on. If the defender phase is incompressible, then pores that become surrounded by the invader (entrapped) are removed from the list. Conversely, if the defender fluid is infinitely compressible or will dissolve in the invading phase then entrapped pores should not be removed. Invasion is stopped when no pores are found that are above a specified cutoff in assigned invasion probability.

Invasion percolation has been shown to conform reasonably well to the invasion of a random, spatially uncorrelated, two-dimensional pore network by a non-wetting fluid. Under these conditions the fluid-fluid interface exhibits structure on all scales down to the pore scale and has been shown to be fractal (Lenormand and Zarcone, 1985). However, wetting fluids invading

porous networks show smooth interfaces that form macroscopic saturation fronts. In addition, when a denser/lighter fluid displaces another from above/below, gravity/buoyancy driven fingering occurs under conditions of low flow. These fingers are found to be macroscopic under wetting invasion and microscopic under nonwetting invasion. Invasion percolation was modified by Glass and Yarrington (1989, 1996) to include gravity and the influence of multiple-adjacent-neck-pore-filling to increase the curvature required to fill a pore with the wetting fluid. This Modified Invasion Percolation (MIP) model was able to capture the essence of the wetting fluid advancement into a porous media. For horizontal invasion, macroscopic fronts formed, their complication a function of pore size distribution. For IP, fronts do not form and the invasion structure is not influenced by the pore size distribution, only its hierarchy. With gravity, macroscopic gravity-driven fingers formed instead of the pore scale fingers predicted from simple inclusion of gravity in IP. To accommodate a variety of additional processes including gas diffusion (Prat, 1993) and film flow (Blunt and Scher, 1995), others have modified IP.

2.2 MIP applied to fractures

In fractures, an MIP model was developed by Glass (1993) to include gravity and an interfacial smoothing mechanism similar to multiple-adjacent-neck-pore-filling. The fracture aperture field is conceptualized as a planar checkerboard of individual elements with a four-fold connectivity (five point stencil); the center of each element has a known local aperture. After Wilkenson (1984), gravity is included in proper magnitude relative to capillary forces by recasting the probability of invasion in terms of a total aperture invasion pressure. The total aperture invasion pressure, P_t, is calculated as the sum of the capillary pressure and hydrostatic pressure induced by the differential phase densities. Capillary pressure, P_c, is a function of the two principal radii of interfacial curvature r_1 and r_2, and the surface tension σ, as given by the Laplace-Young relation

$$P_c = -\sigma\left(\frac{1}{r_1} + \frac{1}{r_2}\right) \qquad (1)$$

Hydrostatic pressure, P_g, is simply given by

$$P_g = -\Delta\rho g z \cos(\theta) \qquad (2)$$

where $\Delta\rho$ is the differential fluid density, g the gravitational acceleration, z the spatial coordinate defined in the plane of the fracture to be positive into the aperture network from the invasion edge, and θ the angle between vertical and the plane of the network.

As shown in **figure 2a**, we take one principal radius of curvature, r_1, to be normal to the plane of the fracture (given by half the local aperture, *a*) and the other, r_2, to be in-the-plane of the fracture. Note that the curvature defined by r_1 will intersect the fracture walls while that defined by r_2 will not. Therefore, wettability affects only r_1. As shown in **figure 2b**, r_1 is related geometrically to the local aperture (*a*) and local convergence/divergence angle of the fracture surfaces (β) through the contact angle (α) at the fluid/fluid/fracture surface.

$$r_1 = \frac{a}{2\cos(\alpha+\beta)} \qquad (3)$$

Wettable fractures are given by $0<\alpha<90$ and nonwettable by $90<\alpha<180$ with $\alpha=90$ as neutral. The convergence/divergence angle of the two fracture surfaces, β, will be positive for widening aperture and negative for narrowing. Incorporating smooth local aperture geometry variation creates a local directional dependency of the aperture invasion potential.

Glass (1993) approximated the local effect of r_2 when an aperture is invaded by considering three configurations evaluated by the number of adjacent apertures filled with water (see **figure 3**). For one adjacent filled aperture, invading the aperture in question yields a final local r_2 that is negative and approximately equal to d, the distance between aperture locations. For two and three adjacent filled apertures, the local interface will be nearly flat after the aperture is invaded and thus r_2 is considered to add a negligible influence (i.e., r_2 is large). This local approach, while yielding reasonable qualitative (i.e., macroscopic invasion fronts) and quantitative (i.e., gravity-driven finger widths) results, overly emphasized the local curvature yielding grid oriented, blocky fronts atypical of the experimental data.

The proper calculation of r_2 includes information from further away than the adjacent apertures. Experimental observations show that as the front moves into a new aperture location it also moves partially into apertures on either side, thus decreasing the local curvature. In addition, the discritization of a continuous fluid/fluid interface onto a gridded aperture field yields many local discontinuities (steps), no matter the resolution of the grid.
These discontinuities can be misattributed to large local in-plane curvatures. Here we propose a simple model for estimating r_2 that both avoids discontinuity focusing and incorporates information from a selected number of nearby apertures along the interface.

Consider r_2 as a function of the included angle, γ, between two vectors representing the average interface once an aperture is invaded (see **figure 4a**). Noting that r_2 should become infinite or zero when γ approaches 180 or 0 degrees, respectively, we propose r_2 as

$$r_2 = d_* \tan\left(\frac{\gamma}{2}\right) \qquad (4)$$

where d_* is a constant of proportionality that can be thought of as a representative r_2 for the grid. To estimate d_*, we evaluate (4) for $\gamma = 90$ degrees to yield $r_2 = d_*$. If we represent the curvature in this geometry as a circle constrained to be tangent to the two vectors defining the front (see **figure 4b**) we see that a value of d_* above 3 times the grid spacing d does not invade the aperture while a value below d gives a curvature which is too large. By inspection, a representative d_* might be taken between 1 and 3 as the curvature interacts with the adjacent apertures yet still invades the aperture in question.

γ can be determined as a weighted average of unit vectors extending from the subject aperture to each of a chosen number of aperture locations along the filled interface in each direction. Here we calculate the weighting factor as the reciprocal of the neighbor number (1 for nearest, 2 for next nearest, etc.) raised to a power. While the power could be chosen to be any value, positive

values that weight closer locations heavier seem more reasonable than negative values that do the opposite. A power of zero gives equal weighting to all vectors.

Incorporating α, β, and in-plane curvature into the total invasion pressure for a given aperture, P_t, gives

$$P_t = -\sigma\left(\frac{2\cos(\alpha+\beta)}{a} - \frac{1}{d_* \tan\left(\frac{\gamma}{2}\right)}\right) - \Delta\rho g z \cos(\theta) \qquad (5)$$

Note that the numerical implementation of MIP to include in-plane curvature requires a simple modification of IP. After an aperture fills, P_t must be recalculated for the neighboring apertures along the interface within the distance where the in-plane curvature change is felt (i.e., the number of locations chosen to determine γ).

3. MODEL APPLICATION

As a first step in evaluating the MIP model, we consider the interplay between gravity and the two capillary terms that result from the two principal radii of curvature (equation 5). In order to facilitate model evaluation though comparison to physical observations, simulations are performed using an aperture field and fluid properties that are consistent with our previous experimental studies where air/water displacements in an analog rough-walled fractures were considered (Nicholl et al., 1992, 1993a,b, 1994; Nicholl and Glass, 1994; Glass and Nicholl, 1995a,b). In our experiments, which are detailed in a subsequent section, two pieces of textured glass (flat on one side) were placed in a test cell such that an aperture field was formed between the two textured surfaces; digital images were then used to record phase structure during fluid/fluid displacement. Subsequent to the above referenced experiments, a high-resolution digital imaging system was used to measure the fracture aperture using a light transmission technique; those measurements were then used in the simulations reported here.

3.1 Aperture field determination and analysis

Representative portions of the analog fracture's aperture field were previously measured at 0.1 mm spatial resolution both with a laser profilometer (2.5 x 2.5 cm portion 256x256 points) and with a light absorption technique (20 x 10 cm portion, 2048x1024 points) (Glass, 1993). Direct application of the Lambert-Beer law to light intensity field data collected by the CCD camera (2048x2048, 4096 gray scale) yielded an aperture field much narrower than measured with a profilometer at the same 0.1 mm spatial resolution. In this early work, the mean aperture was subtracted from the data and the resulting field was "stretched" with a constant factor and then shifted back by the mean aperture. The stretch factor was chosen to yield a maximum aperture given as twice the mean (as found in the profile data). Apertures less than zero after this process were set to zero. In recent studies focused on aperture measurement in transparent fractures (in preparation), we have found that the absorption characteristics of the dye deviates substantially from the Lambert-Beer law for the concentrations in the images analyzed by Glass (1993). Fortunately, other images had been taken at a lower dye concentration where the discrepancy with theory is found to be less. We analyzed these lower concentration images and stretched the resulting aperture distribution using a linear stretch factor (takes minimum and maximum prestretched aperture to 0 and twice the mean aperture, respectively) to match the profile data. **Figure 5b** shows a histogram of the aperture field measured with the profilometer, that used by Glass (1993), and our current aperture field; a representative 25.6 mm square section of our current aperture field is shown in **figure 5a**.

The roughened glass plates produced an apparently homogeneous aperture field with a mean aperture of 0.215 mm and a standard deviation of 0.075 mm; the center 102.4 x 51.2 mm (1024 x 512 pixel) section of this aperture field was selected for use in the simulations. As a test of homogeneity, population statistics were measured on 6.4 mm^2 sub-samples of the selected aperture field; statistics of the sub-samples are consistent with those of the population (see **figure 6**). Point-to-point variance of the aperture field was measured as a function of separation length on both primary axes and on the principal diagonals. Measured data implies a correlation length on the order of 0.8 mm, or 8 grid points (see **figure 7**). In order to assure that the strong correlation observed at small scale (<0.8 mm) was not obscuring longer range correlation, aperture resolution was reduced through arithmetic averaging (128 x 256, 64 x 128, 32 x 64, 16 x

32) and the point-to-point variance re-measured. This analysis reconfirmed the short range correlation length, and did not reveal any longer scale correlation. Average transects were used to further explore potential large scale features. The data (see **figure 8**) show no trends, but implies a very slight sinusoidal variation in the row and column means. Spectral analysis (see **figure 9**) was inconclusive with respect to sinusoidal variation at long wavelength. While deviating slightly from perfection, it is apparent that above the correlation length this aperture field exhibits a very high degree of both homogeneity and isotropy.

Equation 5 incorporates the local deviation of the fracture surface from the mean plane (β). By assuming that the fracture aperture varies symmetrically about its mean plane we can measure the maximum deviation from that plane at every point in the aperture field (see **figure 10**). This data shows that for the aperture field considered here, β will be relatively small and is therefore expected to have minimal impact on the invasion process away from neutral wettability (α=90).

As a final analysis of the aperture field, we characterize the equilibrium phase saturation field with SP assumptions. Apertures are filled in strict order of aperture size without accessibility rules; from smallest to largest for wetting fluid invasion and vice-versa for nonwetting invasion. This process does not allow entrapment of the defending phase. Fracture saturation for a given invading phase is assumed to be solely a function of pressure as defined by the LaPlace-Young equation with only r_1 included (see **figure 11**). If the aperture field was entirely random with no spatial correlation, one would expect a single percolation threshold; i.e., only one of the two phases could span the system at a time. Conversely, correlation within the aperture field can lead to separate percolation thresholds for each phase. The pressure range between the two thresholds will correspond to either a gap (neither phase spans) or an overlap (both phases span). In this homogeneous, isotropic system that is much larger than the correlation length there is a range of pressures for which neither phase spans the system (**figure 11**). The width of this gap is expected to vary with system scale and may disappear or become an overlap as the system scale decreases. Phase structures for the 1024 x 512 portion of the aperture field at the percolation threshold are shown as **figure 12** for wetting and nonwetting invasion.

3.2 Choice of in-plane curvature parameters

The in-plane curvature algorithm requires that we choose the number of front locations on either side of the subject aperture to consider in calculating γ, the weighting power, and the representative r_2 given by d_*. For non-negative weighting powers, the number of locations considered and the weighting factor are correlated. To decrease the degrees of freedom, we therefore chose to give equal weighting to each location (weighting power of 1). A series of simulations were then conducted to consider sensitivity to the number of locations and choice of d_* on our measured aperture field. Simulations demonstrated that as the number of locations is increased, the simulation moves gradually from blocky (one location) to qualitatively similar to experimental data at just below the spatial correlation length of the aperture field (6 locations, .6 mm). These results support the notion that the spatial correlation length (.8 mm) should give a maximum distance over which a local in-plane curvature estimate should be defined. We therefore chose 6 locations on each side of the subject aperture for the calculation of the included angle γ. Increasing d_* from the grid resolution, d, to above the correlation length moves the simulation from smooth to independent of r_2. Qualitative comparison to experiments suggested that d_* taken to be d was too smooth while 2 or 3 times d gave reasonable results. d_* was

therefore chosen as 2 times d for our application simulations. Note that this choice is also consistent with the general results obtained from simple geometric arguments show in **figure 4c**.

While comparison to data suggests that our current choices of in-plane curvature parameters are reasonable for our analog fracture, more detailed consideration of these parameters is required. However, this detailed consideration must be deferred until data is gathered that yields high resolution frontal dynamics where curvature can be calculated and compared to our algorithm. In addition, characteristics of the aperture field spatial structure should be considered and varied in the future so that the connection between in-plane curvature and aperture field structure (spatial correlation) is resolved.

3.3 Numerical simulations

Within the aperture field of our analog fracture, we explore for the water-air system (fixed density difference) the influence of each component of the capillary force both with and without the presence of gravity, i.e., horizontal and vertical fracture orientation, respectively. To vary the influence of the local aperture induced curvature, r_1, the contact angle, α, is changed to yield cosine α of 1.0, 0.75, 0.5, 0.25, 0, -0.25, -0.5, -0.75, and -1.0 (i.e., 0, 41, 60, 76, 90, 104, 120, 139, and 180 degrees). The in-plane curvature, r_2, was either neglected or included. For vertical cases, both upward invasion (gravity stabilized and destabilized) and downward invasion (gravity stabilized and destabilized) are considered. The surface tension and density were held constant at their standard temperature and pressure values. Invasion was initiated along a short axis of the field and orientation within the gravity field (tilt or inclination) was imposed along the long axis. Because of the small range of pressures considered in our simulations, we treat both air and water as incompressible and implement a trapping algorithm. Free flow conditions were imposed for the defending phase on the bottom and each side of the aperture field.

For all situations (horizontal, vertical gravity stabilized and destabilized) we conducted simulations that either included or neglected the convergence/divergence angle β. β has an increasing influence on the invasion process as α approaches 90 from either 0 or 180 degrees. At neutral wettability (α = 90), β shifts the sign of r_1 such that some apertures become intrinsically nowetting (r_1 negative) while others wetting (r_1 positive). Away from neutral wettability however, for our aperture field, the effect of convergence/divergence within the local aperture field was found to be small in terms of the general behavior of the MIP model. This is to be expected due to the primarily small values of β found in our aperture field (mean of absolute value of β was 7 degrees, **see figure 10**). While the exact phase invasion structures differed, they were qualitatively very similar and gave similar macroscopic values for phase saturations. The difference in the evolving phase invasion structures is due to the fact that β slightly modifies the aperture hierarchy within the field depending on the invasion direction of a particular aperture. Because of the small effect of β away from neutral wettability, we will not consider its influence further in this paper.

Finally, for simplicity, the simultaneous invasion of both wetting and nonwetting phases within a simulation is also not implemented here. Simulations, therefore, yield the saturation structure swept by the invading phase. The inclusion of simultaneous invasion of wetting and nonwetting phases is required to simulate drainage behind advancing gravity/buoyancy driven finger tips and will be explored in the future.

4. SIMULATION RESULTS

For each of our simulations, the wetted structure when water first reaches the other side of the aperture field (breakthrough for horizontal and vertical gravity destabilized cases) or when gravity forces just offset capillary forces (vertical gravity stabilized cases) was analyzed. Color printouts of these structures are included in **Appendix A** for completeness. For all of the simulation phase structures presented in this paper, the color sequence from violet to blue to green to yellow to orange to red depicts the order of invasion from first to last, black denotes defending fluid remaining that can still escape the network, and gray the entrapped defending fluid. For the horizontal cases, final structures at the completion of the invasion process (all apertures filled either with invading fluid or entrapped defending fluid) were also analyzed.

4.1 Horizontal invasion

Where in-plane curvature is neglected, a single phase invasion structure results for the nowetting or the wetting invasion process, respectively **(see figure 13)**. These are the results of IP as applied to our aperture field containing spatial correlation. Capillary fingering (exhibiting directional independence) and subsequent phase entrapment is suppressed at scales below the correlation length. Above the correlation length, capillary fingering results in macroscopic capillary fingers with width on the order of the correlation length. The aperture field consists of small rounded regions or "basins" of correlated aperture, large and small. A phase will tend to fill up a basin before breaking over the surrounding basin "edge" and entering a new basin. On close inspection, capillary fingers are often seen to reduce to a single pixel wide where the finger reaches an edge in the local aperture field basin. Observing the dynamics of the invasion process as the finger "spills" over this edge shows a single aperture wide tendril to grow to the bottom of the next aperture basin and then expand laterally as the basin is filled up from its center. The resulting character of phase occupancy for nonwetting invasion (more "wormy") is slightly different from wetting invasion (more "ball and stick") due to the details of the correlated aperture field structure (**see figures 5 and 10**)

With aperture field structure dominating the invasion sequence, phase entrapment of the defending fluid occurs at or above the correlation length. This macro entrapment yields nearly identical final saturations (at invasion completion) regardless of which phase is invading of 0.64 - 0.68 and 0.36 - 0.32 for the nonwetting and wetting invasion, respectively. Phase occupancy aperture distributions for either wetting or nonwetting invasion at the final state are nearly identical; again demonstrating that the correlated aperture field structure significantly controls phase occupancy independent of which fluid is invading or defending.

Inclusion of in-plane curvature (r_2) results in a dramatically altered invasion phase structure (**see figures 14 and 15**). For both wetting and nonwetting invasion, the edge spill-over, tendril formation and basin fill-up dynamics seen when r_2 is neglected are suppressed. A tendril one pixel wide would result in extreme curvature (**see figure 4)** causing the in-plane curvature term to be very large in equation 5; it is obvious that such features will be suppressed and hence the front advances macroscopically. For nonwetting invasion, while the details of the aperture field are still apparent, the macroscopic capillary fingers have widths several times that observed without in-plane curvature and never decrease to a single aperture wide. For wetting invasion,

the front is fully macroscopic with "fingers" many times the correlation length in width reflecting little of the underlying structure in the correlated aperture field.

The influence of in-plane curvature increases as contact angle changes from fully nonwetting (180) or wetting (0) toward neutrality (90) (i.e., aperture field dependent capillary forces decrease in importance). Fingers become increasingly wide until at 90 degrees (where aperture field capillary forces are zero), an invasion structure results with no fingers at all. At $\alpha = 90$ and $\beta = 0$, equation 5 shows that P_t will be independent of aperture and the invasion front will widen to the system width. The control of the in-plane curvature term on the structure is also seen in the distribution of apertures filled with each phase at the final state. The more macroscopic the structure (with respect to the correlation length) the broader the distribution of apertures filled with each phase. In addition, as in-plane curvature becomes more important (contact angle approaching 90 degrees from either direction) final invading phase saturation increases (**see figure 16**).

The character of the entrapped defending phase is different between wetting and nonwetting phase invasion. For wetting invasion, the entrapped clusters have no resemblance to the details of the aperture field, while for nonwetting invasion, entrapped clusters maintain aperture field like structures for all contact angles considered ($180<\alpha<90$). Since in-plane curvature is independent of contact angle, this observation may reflect a difference in the connectivities within the small apertures versus the large apertures (note that this cannot be evaluated through the standard analysis of spatial correlation within our aperture field presented above).

4.2 Gravity destabilized invasion

The addition of a gravitational potential within the vertical fracture creates a single gravity-driven finger oriented downward or upward depending on whether the invading fluid is heavier (water above air) or lighter (air below water) than the defending fluid. Where r_2 is neglected, gravity essentially selects a single "branch" of capillary fingers for preferential growth in the direction of the density driven resultant body force (**see figure 17**). Near the growing tip of the branch, capillary fingers grow in all directions, however, they loop back on themselves preferentially in a downward direction with outward and upward growths starving as the overall branch tip moves downward. We define this primary branch as the gravity-driven finger. Because it is composed of capillary fingers, the gravity-driven finger shows the detail of the aperture field and in many places reduce to a single pixel wide. The small scale invasion dynamics are identical to the horizontal case where r_2 is neglected; however, gravity selects which "edge" is spilled over once a local "basin" is filled and thus imparts the preferential direction for the gravity-driven finger.

Without in-plane curvature, the character of the gravity-driven fingering is influenced weakly by wettability until close to neutral ($\alpha = 90$). Finger widths which are dependent on looping back of the individual capillary fingers that compose the gravity finger, are seen to vary only slightly as contact angle varies from 0 to 76 and 104 to 180 degrees (**see figure 19**). Large scale finger "meandering" is also indicative of the interplay of gravity and local capillary forces within the fracture; increased influence of capillary forces (and capillary fingering) yields increased meandering. As the contact angle increases from 104 to 180 degrees, increased capillary fingering and gravity finger meandering does occur. However, for the wetting invasion, such a

trend from 76 to 0 degrees is either absent or very weak. Near neutral wettability (above and below 76 and 104 degrees, respectively), the influence of gravity overwhelms capillary forces and fingers decrease dramatically in complication until at neutral wettability, the finger falls vertically with a width of a single aperture.

As in horizontal invasion, the addition of in-plane curvature creates macroscopic fingers now oriented in the direction of the gravity induced resultant body force (**see figure 18**). Average finger width is over an order of magnitude greater than the correlation length (**see figure 19**), invaded apertures thus spanning the entire aperture distribution. Meandering and finger edge complication increases as the contact angle varies from 90 to either 180 or 0 degrees. Entrapment, while slight, also increases as aperture induced (r_1) capillary forces increase. Note that finger edge complication and entrapment structure is higher for the nonwetting invasion process, once again emphasizing a possible difference in small aperture versus large aperture spatial connection.

4.3 Gravity stabilized invasion

Where r_2 is neglected, gravity stabilized invasion suppresses the scale of capillary fingering (**see figures 20 and 21**). Capillary fingers now more actively connect back on each other as the invasion process progresses, immediately entrapping the defending phase in a large number of small clusters and creating an advancing "front" oriented normal to the gravitational field. Both the maximum size of the entrapped clusters and the width of the advancing front (defined as the zone where the defending phase transitions from fully saturated to fully entrapped) increase slightly as contact angle varies from 90 to either 180 or 0 degrees (i.e., local capillary forces increase). While phase saturation behind the front varies only slightly as a function of contact angle (**see figure 24**), phase entrapment is extreme. For wetting invasion, average saturations of only 0.4 are achieved while for nonwetting invasion, higher saturations of approximately 0.7 result. When r_2 is included, once again, the invasion structure is greatly altered (**see figures 22 and 23**). The invasion front narrows and phase entrapment decreases (**see figure 24**). In fact, for wetting invasion, appreciable phase entrapment does not occur at all.

4.4 Pressure-saturation curves

The gravity stabilized simulations were analyzed to build wetting and drainage pressure-saturation curves for the air-water system within the fracture. We apply a boundary invasion pressure (expressed as a length of water) at the bottom (wetting imbibition) or the top (nonwetting drainage) and allow the invasion process to proceed to equilibrium (pressure hydrostatic within each phase). The resulting phase occupancy structures are reduced to yield saturation profiles which are then plotted with respect to pressure head. Assuming no contact angle hysteresis, representative plots for the structures formed for contact angle pairs of 0 and 180 (fully wetting/nonwetting) and 60 and 120 degrees are shown in **figures 20 through 23.** When r_2 is neglected, we see that no hysteresis is induced by the aperture field. In porous media, "ink bottle" and "grouped" pore emptying/filling mechanisms have been presumed to create hysteretic behavior due to the juxtaposition of individual pores. However, hysteresis does not result from these mechanisms in our aperture network. Instead, with r_2 neglected, hysteresis can only be induced by the often considered weak influence of contact angle hysteresis. However,

when r_2 is included, strong hysteresis results (**see figures 22 and 23**) independent of assumptions of contact angle hysteresis.

For porous media, pressure head-saturation curves have been assumed to scale with contact angle. However, for fractures, because r_2 is independent of contact angle, such a scaling will not be wholly effective where r_2 is non-negligible. We demonstrate this in **figures 25 and 26** where pressure head-saturation curves have been scaled by the contact angle with r_2 included and neglected, respectively. Notice that even though the scaling is quite effective when r_2 is neglected, it is not entirely perfect because the residual phase saturations are influenced by the ratio of gravity to capillary forces (bond number) and thus also be a function of fracture inclination within the gravitational field. Including r_2, the scaling moves the curves reasonably well "on average" but, of course, cannot scale the r_2 induced hysteresis (see equation 5).

5. COMPARISON TO PREVIOUS EXPERIMENTS

In recent years we have conducted a large number of physical experiments exploring air-water invasion processes in analog fractures formed from the same material as the one considered in these simulations. In our experiments, two pieces of hydrophilic textured glass (flat on one side with a 'star' shaped pattern on the other, 305 mm by 152 mm) were placed in a test cell (**figure 27**) such that the two textured surfaces formed an aperture field. In order to minimize large scale variations in the aperture field, a confinement pressure (20 psi) was applied normal to the fracture plane. Windows in the test cell allow viewing of the transparent sample, which was backlit with high frequency fluorescent lamps. Data was collected in the form of digital images of the fracture plane; contrast between the phases (air, water) was enhanced by adding dye to the water. Gaskets forming the confinement cell obscure the outer edges (~10 mm) of the fracture plane, so the full fracture could not be viewed. A rotating test stand (**figure 27**) allowed controlled variation in the fracture inclination while maintaining orientation between the sample, light source, and digital CCD camera. After each experiment, the cell was disassembled, the fracture plates washed with DI water followed by isopropyl alcohol, and the cell reassembled. Occasionally, the fracture plates broke and were replaced with pieces cut from the same textured glass stock. We measured the contact angle on pieces of new and broken (after retiring) textured glass surfaces from visual inspection of a water drop to be between 35 and 55 degrees. Because the aperture field was formed from a relatively homogeneous material with a consistent surface cleaning procedure that was placed under a repeatable confinement pressure, we expect that aperture fields used in our previous experiments were statistically equivalent to the one measured and used for our simulations presented above.

While these past experiments were not specifically designed to challenge the MIP model, they do provide data for qualitative and some quantitative evaluation of model validity. We first consider horizontal and vertical (both gravity destabilized and stabilized) phase displacement experiments where phase invasion structure images were collected at low spatial resolution (512x512 points with 256 gray levels, then state-of-the-art). For these experiments the aperture field for any particular experiment was not measured; behavior can be compared to the model results qualitatively and supported by a limited number of gross quantitative measurements. We then consider an entirely different invasion mechanism, air dissolution into flowing water and compare to the data of Glass and Nicholl (1995a) where both the aperture field and the phase invasion structure were measured at high resolution (2048 x 2048 pixels, 4096 gray levels) at the time of the experiment in a fracture formed from this same material; in this case, the details of model performance can be directly compared to physical measurements.

5.1 Horizontal invasion

Experimental images showing phase structure development during slow imbibition of water into an air filled analog fracture (wetting invasion) from a point source in the absence of gravitational forces (horizontal) are shown as **figures 28-30**. Note that the scale of the experiment (152 x 305 mm) is three times that of the numerical simulation (51.2 x 102.4 mm) and that the inflow boundary condition consisted of a point source located at the center of the short edge. Despite the differences in both scale and boundary condition, qualitative comparisons can be made between model simulation and experiment. In order to facilitate comparison between experiment and simulation, the final images shown in **figures 28-30** are composites of experimental observations

that illustrate growth of the invasion structure. The compact structure of the experimental wetting fronts is notably dissimilar to simulations that neglect r_2 (**see figure 13**). Entrapment of the defending phase and complexity of the invading phase structure are grossly overestimated in the simulations. The simulations also display a characteristic length scale that is on the order of the correlation length; a feature that is not seen in the physical experiment. Simulations where r_2 was included much more closely reflect the compact nature of the physical invasion process (**see figures 14,15**). Simulations with contact angles between 41 and 60 degrees give the closest qualitative match to the experimental data. The physical experiment also appears to entrap larger clusters of defender fluid than does the simulation; however, this is likely a scale effect of the larger experimental fracture.

Slow displacement of water by air (nonwetting invasion) in the analog fracture is shown in **figure 31.** In this experiment, the long sides of the fracture were sealed and flow manifolds placed across the full width of the upstream and downstream boundaries. Air was supplied slowly to the upstream boundary using a positive displacement pump while the downstream boundary was vented to atmospheric pressure. In order to facilitate comparison between experiment and simulation, the final image shown in **figure 31** is a composite of experimental observations that illustrate growth of the invasion structure. Compared with wetting invasion shown in **figures 28-30**, the complexity of the phase structure at breakthrough is much higher. Noting that this experiment is also a factor of three larger than our simulations, it is apparent that simulations neglecting r_2 (**see figure 13**) do not well represent the phase invasion structure, while those that include r_2 do quite well for contact angles in the range of 120 to 180 degrees (**see figures 14,15**). Again, complexity of the phase structure is grossly overestimated and characteristic length scale underestimated in the simulations where r_2 is ignored.

5.2 Gravity destabilized invasion

Images showing the development of gravity-driven water fingers during three experiments from Nicholl et al. (1993a) are shown in **figures 32-34**. The air-filled analog fracture was inclined to vertical, then slow steady flow of water was initiated from a point source located on the upper boundary; note again that the width and length scales of these images are three times larger than the numerical simulations. In each experiment, a single gravity-driven finger initiates from a hanging column that is pinned to the upper boundary of the fracture by capillary forces. The gravitational body force places the hanging column under suction, which increases in magnitude with distance from the advancing tip. As the column grows downward, suction along the top increases. When that pressure becomes sufficient to allow the re-invasion of air, the phase saturation structure above the advancing tip becomes more complicated. As previously stated, the simulations presented here only consider the area swept by the advancing finger tip and not the re-invasion of air behind the finger tip. In order to facilitate comparison between experiment and simulation, the final images shown in **figures 32-34** are composites of experimental observations that illustrate growth of the region swept by the advancing finger. Again, on a qualitative basis it is apparent that inclusion of r_2 in calculation of invasion potential is necessary. Where r_2 is not included (**see figure 17**), the simulation forms fingers that entrap the defending phase, meander significantly about the fracture, and demonstrate an aperture field structure dominated complexity in their structural form; all of these discrepancies from experiment are ameliorated by inclusion of r_2 in the calculation of invasion potential (**see figure**

18). Quantitatively, when r2 is included, the macroscopic fingers have widths that are underestimated by 25 to 30% (**see figure 19**).

The occurrence of buoyant air fingers within water saturated fractures was demonstrated by Glass and Nicholl (1995b). The 152 by 305 mm analog fracture was filled with water and then all four boundaries were sealed. After inclining the fracture to vertical, air was allowed to pass along the bottom boundary. The resultant evaporation led to gravity destabilized air (nonwetting phase) invasion. **Figure 35** shows a blowup of an individual finger growing upward within this field at a scale roughly the same as that of the simulations. The finger moves into the field of view in a sub-horizontal direction; it then moves sharply upward. Influence of the aperture field is clearly seen as well as phase entrapment within the finger. As with the gravity-driven water fingers described above, the defending phase was observed to re-invade the aperture field a distance behind the leading edge of the invading phase. **Figure 36** shows the large scale pathways formed by a number of fingers that slowly formed through the fracture during the course of the experiment. These limited experimental observations imply that inclusion of r_2 in calculation of the invasion potential provides qualitatively superior simulations. A range of measured finger widths are shown in **figure 19;** as with the wetting phase invasion, simulated finger width is closer to the observed values with inclusion of r_2 in the MIP model.

5.3 Gravity stabilized invasion

At the end of each gravity-driven fingering experiment performed by Nicholl et al. (1993a), water rose in the fracture from its bottom edge resulting in an equilibrium gravity stabilized wetting invasion structure. The lower boundary of the fracture was held open to atmospheric pressure. When the finger reached this boundary, the water spread out along the boundary and began rising until capillary forces just offset gravity. Equilibrium was assumed to occur when water began to drip out the bottom of the fracture. The position of the phase interface resulting from such capillary rise within the 305 by 152 mm fracture is shown in **figure 37.** Unfortunately, the fracture gasket obscured much of the rise. However, enough was observed to determine that capillary rise formed a very compact phase structure that was not observed in the simulations unless r_2 was included in calculation of invasion potential (compare **figures 20 and 22**). Capillary rise height in the fracture was measured this way in over 100 experiments, yielding a value of 22.5 +/-2.6 mm. MIP simulations with a contact angle of 41 and 60 degrees yield capillary rises of approximately 18 and 32 mm, respectively.

For the work reported in Nicholl et al. (1993b) on the influence of initial moisture content on gravity-driven fingering, several preliminary experiments were conducted in the 305 by 152 mm analog fracture that can be used to consider gravity stabilized nonwetting invasion by the air phase. In these experiments (**figure 38**) the analog fracture was saturated with water and then rotated to vertical with all boundaries open to atmospheric pressure. The air phase invaded vertically downward as water drained out the fracture bottom. Drainage ceased when pressure at the interface reached equilibrium. The residual phase structure closely resembles simulation results when r_2 is considered (**figure 22**). Without r_2, the simulations overestimate the size, number, and complexity of the residual defender phase; penetration of the invading phase is also much less uniform (**figure 20**). Drainage heights for the experiments ranged from 56 to 60 mm, and from the simulations, 110 to 65 for contact angles of 180 and 120, respectively.

5.4 Horizontal invasion gas dissolution order

Within our fracture, the dissolution of entrapped air into a flowing water phase was also studied by Glass and Nicholl (1995a) **(see figure 39**). Slow air invasion of a water saturated, horizontal fracture (e.g., **figure 31 above**) followed by water flow, entrapped the initial air phase within the analog fracture. Images of the fracture taken with a high resolution CCD camera (2048x2048 pixels, 12 bit gray scale) allowed us to track the shrinkage (dissolution) of the entrapped phase in time as the flowing phase was switched to de-aerated water. The aperture field on this particular fracture was measured with the same techniques and analysis procedures as described above but at a lower spatial resolution of 0.15 mm per pixel.

The dynamic shrinkage of individual entrapped air blobs on a known aperture field affords us our most rigorous test (with previously reported data) of percolation based approaches to model phase invasion within a fracture. **Figure 40** shows the shrinkage of a typical entrapped air cluster along with shrinkages predicted by SP, IP and MIP applied with the same constraints on in-plane curvature parameters as chosen for the previous simulations reported above. For SP, water can invade any aperture within the air blob regardless of whether it is along the outer water interface. For IP and MIP, water can only enter the air blob around it's outer edge. We see that both IP and SP yield results very similar to those seen above for phase invasion from edges and do not predict well the experimental data. MIP, however, does a very good job at representing the shrinking order dynamics.

6. CONCLUSION

We have found that the inclusion of gravity in invasion percolation approaches applied to fractures yields the formation of gravity-driven fingers in non-horizontal fractures and that in-plane interfacial curvature, which is neglected in SP and IP modeling approaches, greatly affects the phase invasion structure in both horizontal and non-horizontal fractures causing the formation of macroscopic fronts and macroscopic gravity-driven fingers. Comparison to all experimental data available at this time, substantiates MIP while invalidating IP and SP approaches applied to our fracture. While we have met with some success in developing and evaluating a new form of invasion percolation for application to fractures, a number of issues remain. In the following, we address a series of issues, implications, extensions and hypothesized system behavior around which future studies must be focused.

6.1 Hypothesized behavior of the general fracture

Consideration of the total invasion pressure equation suggests model and physical systems to behave generally as follows. Aperture variability (including β), gravity, and in-plane interfacial curvature all compete to determine filled aperture structure. Choices of values of the parameters describing each can be made such that one dominates over the others. Where gravity dominates, fingers move through the network. Where in-plane interfacial curvature dominates, water moves across the network from the supply surface with one macroscopic front. Where aperture variability dominates, the structure conforms to IP. In order to evaluate this hypothesized interplay of gravity, capillarity, and aperture field (distribution, spatial structure and heterogeneity) in determining phase saturation structure under non-equilibrium conditions, additional simulations verified with physical experimentation are required.

6.2 Necessity of model comparison to physical experiments

SP, IP and MIP models give substantially different predictions of phase structure during phase displacement in our analog rough-walled fracture. The critical evaluation of these models requires direct observation of phase structure within the fracture tied to fracture scale measurements. Without such comparison, misapplication will yield erroneous results. We illustrate this point through comparison of the work of Reitsma and Kueper (1994) and Glass and Norton (1992).

Reitsma and Kueper (1994) measured pressure-saturation curves for an induced horizontal fracture in permeable rock where a nonwetting phase (NAPL, air) was introduced around the edge of the fracture initially filled with a wetting phase (water). The pressure saturation relations measured were abrupt. Assuming an SP model for phase invasion structure, they extrapolated the aperture distribution from the pressure-saturation curves. Glass and Norton (1992) measured pressure saturation relations in a similar horizontal fracture-matrix system formed by a roughened glass plate mated with a porous slab matrix. Again, the wetting phase (water) could enter and exit the fracture through the matrix while the nonwetting phase (air) could only enter or exit through the fracture edges. In their experiment, however, the phase structure within the fracture was recorded and showed threshold behavior with pressure both in phase spanning of the fracture and in nonwetting phase entrapment. This threshold behavior yielded abrupt pressure

saturation relations and the inferred relative permeability. In addition, water could be seen to enter the fracture from nucleation points, presumably locations where the matrix touched the other side of the fracture (contact points), after which it grew within the fracture through connection to these points. Clearly assumptions of either SP or IP are incorrect and cannot explain the behavior of the fracture/matrix system. Interpretation of experimental pressure-saturation results using an SP model to yield aperture distributions as was done by Reitsma and Kueper (1994) is therefore highly suspect.

6.3 Implications for effective fracture properties

In terms of macroscopic effective properties for single fractures, we have demonstrated the influence of in-plane curvature on pressure-saturation relations. Local and fracture scale hysteresis independent of contact angle hysteresis is imposed by the in-plane curvature as created by the local, small scale aperture field heterogeneity. Thus, the phase entry and spanning pressures for the fracture and the full pressure-saturation curves, cannot be scaled by the contact angle. It should also be noted, that since phase entrapment will increase as the fracture orientation within the gravitational field changes from vertical to horizontal, the residual values of each phase in the pressure saturation relation will also be a function of fracture inclination. Thus, not only will these macroscopic relations between pressure and saturation within a single fracture be hysteretic (thus a function of initial condition) but they also will be a function of fracture orientation within the gravitational field through the residual phase saturations.

Because phase invasion structure influences the flow field tortuosity, effective relative permeability and solute dispersivity relations for fractures will also be a function of fracture orientation. The orientation of the fracture within the gravity field has been previously proposed by Glass et al. (1995, 1996) to influence fracture relative permeability given by $k \sim S^n$ from n=1 for vertical fractures where gravity-driven fingers form to n = 4 or higher for horizontal fractures. Their assumption for the vertical case that gravity-fingers sample the full range of apertures within the field is substantiated for small capillary number by our MIP model results. For the horizontal case, they relied on the data of Glass and Nicholl (1995a) where a nonwetting phase first invaded the fracture followed by wetting invasion and subsequent entrapped nonwetting phase dissolution. Our modeling has not yet addressed these precise conditions. We can, however, propose from our current simulations that the final permeability when the fracture becomes satiated with one phase (completely entrapping the other) will be a function of contact angle, increasing as the contact angle approaches 90 from either 0 or 180 degrees, and for our particular fracture, be lowest for the fully nonwetting invasion process (180). In addition, because phase entrapment is also a function of orientation in the gravity field, the final permeability will transition from lowest for horizontal cases to highest for vertical cases (either gravity stabilized or destabilized). Note that IP yields a phase saturation structure and thus a permeability independent of both the contact angle (i.e., one phase structure for less than 90 and another for greater than 90 degrees) and the orientation within the gravitational field (i.e., it does not include gravity).

6.4 Including viscous forces

MIP applies in the quasi-static limit, i.e., for low flow conditions where capillary and gravity forces dominate viscous forces. However, as with in-plane curvature, viscous forces are found to suppress capillary fingering (for stabilizing mobility ratio), create macroscopic fronts and, therefore, decrease final phase saturations and entrapped phase cluster sizes. It is possible that the first order effects of viscous forces for some situations could be included simply by changing the contact angle (dynamic contact angles are greater than equilibrium). From our simulations, increasing the contact angle for wetting invasion decreases the phase entrapment as is found in experiments within porous media.

6.5 Including permeable walls

The simulations presented in this paper consider only the process of phase invasion from the edges of a fracture with impermeable side walls. Modifications of boundary conditions are straightforward to model phase invasion where one of the phases can enter or exit through permeable side walls. Mendoza (1992) used combinations of IP and SP to model the condition where the wetting phases could enter or exit the fracture via the matrix while the nonwetting phase (NAPL) could only enter or exit the fracture through its edge. However, data from the experiments of Glass and Norton (1992) discussed above indicate that the wetting phase enters the fracture at a number of "nucleation points" from which the invasion process proceeds as if the matrix was no longer present. Thus, for permeable walls, SP and IP approaches are inappropriate analysis requires application of MIP.

6.6 Miscellaneous

In addition, we must further study MIP behavior as a function of the in-plane curvature parameters and the spatial resolution requirements for aperture field data. Following determination of the algorithmic constraints, we must then systematically study both in the laboratory and on the computer, the interplay between the characteristic length scales governing the behavior: gravity scale, in-plane curvature scale, mean aperture (and variance), and spatial correlation length of the aperture field. As part of this study, experiments in fractures that have micro roughness that can support film flow in the wetting fluid must be considered

Finally, the simultaneous invasion of wetting and nonwetting fluids within the simulation field is required to fully model phase saturation structure in non horizontal fractures larger than the saturated finger tip length. Once fully tested, numerical models such as this can be used to systematically explore the effects of fracture aperture heterogeneity, contact angle variability and other system parameters on phase saturation structure. Such process oriented physical and numerical modeling is a necessary step toward including phase saturation processes such as gravity-driven fingering in models of two-phase flow in large-scale fractured systems.

This page intentionally left blank.

7. REFERENCES

Blunt, M.J., and H. Scher, Pore-level modeling of wetting, *Physical Review E*, 52(no.6, pt. B):6387-6403, 1995.

Chatzis, I., and F.A.L. Dullien, Modeling pore structure by 2-D and 3-D networks with application to sandstones, *Journal of Canadian Petroleum Technology*, 16(1):97-108, 1977.

Fatt, I., The network model of porous media I. Capillary pressure characteristics, *Journal of Petroleum Technology (Petroleum Transactions, AIME)*, 207:144-159, 1956.

Glass, R.J., and L. Yarrington, Analysis of wetting front instability using modified invasion percolation theory, *EOS*, 70:1117, 1989.

Glass, R.J., and D.L. Norton, Wetted-region structure in horizontal unsaturated fractures, *High Level Radioactive Waste Management, Proceedings of the Third Annual International Conference,* American Nuclear Society, April 12-16, Las Vegas, NV, pp. 717-726, 1992.

Glass, R.J., Modeling gravity-driven fingering in rough-walled fractures using modified percolation theory, *High Level Radioactive Waste Management, Proceedings of the Fourth Annual International Conference,* American Nuclear Society, April 26-30, Las Vegas, NV, pp. 2042-2053, 1993.

Glass, R.J., and M.J. Nicholl, Quantitative visualization of entrapped phase dissolution within a horizontal flowing fracture, *Geophysical Research Letters*, 22(11):1413-1416, 1995a.

Glass, R.J., and M.J. Nicholl, Near drift two-phase flow processes within regionally saturated fractured rock, *High Level Radioactive Waste Management 1995, Proceedings of the Sixth Annual International Conference,* American Nuclear Society, April 30-May 5, Las Vegas, NV, pp. 212-216, 1995b.

Glass, R.J., M.J. Nicholl, and V.C. Tidwell, Challenging models for flow in unsaturated, fractured rock through exploration of small scale processes, *Geophysical Research Letters*, 22(11):1457-1460, 1995.

Glass, R.J., and L. Yarrington, Simulation of gravity fingering in porous media using a modified invasion percolation model, *Geoderma*, 70(2-4):231-252, 1996.

Glass, R.J., M.J. Nicholl, and V.C. Tidwell, Challenging and improving conceptual models for isothermal flow in unsaturated, fractured rock through exploration of small- scale processes, SNL report SAND95-1824, 1996.

Kwicklis, E.M., and R.W. Healy, Numerical investigation of steady liquid water flow in a variably saturated fracture network, *Water Resources Research*, 29(12):4091-4102, 1993.

Lenormand, R., and C. Zarcone, Invasion percolation in an etched network: measurement of a fractal dimension, *Physical Review Letters*, 54(20):2226-2229, 1985.

Mendoza, C.A. Capillary pressure and relative transmissivity relationships describing two-phase flow through rough-walled fractures in geologic materials, Ph.D. dissertation, Department of Earth Sciences, University of Waterloo, Waterloo, Ontario, 1992.

Nicholl, M.J., R.J. Glass, and H.A. Nguyen, Gravity-driven fingering in unsaturated fractures, *High Level Radioactive Waste Management, Proceedings of the Third Annual International Conference,* American Nuclear Society, April 12-16, Las Vegas, NV, pp. 321-331, 1992.

Nicholl, M.J., R.J. Glass, and H.A. Nguyen, Small-scale behavior of single gravity-driven fingers in an initially dry fracture, *High Level Radioactive Waste Management, Proceedings of the Fourth Annual International Conference,* American Nuclear Society, April 26-30, Las Vegas, NV, pp. 2023-2032, 1993a.

Nicholl, M.J., R.J. Glass, and H.A. Nguyen, Wetting front instability in initially wet fracture, *High Level Radioactive Waste Management, Proceedings of the Fourth Annual International Conference,* American Nuclear Society, April 26-30, Las Vegas, NV, pp. 2061-2070, 1993b.

Nicholl, M.J., and R.J. Glass, 1994, Wetting phase permeability in a partially saturated horizontal fracture, *High Level Radioactive Waste Management, Proceedings of the Fifth Annual International Conference,* American Nuclear Society, May 22-26, Las Vegas, NV, pp. 2007-2019, 1994.

Nicholl, M.J., R.J. Glass, and S.W. Wheatcraft, Gravity-driven infiltration instability in initially dry nonhorizontal fractures, *Water Resources Research,* 30(9):2533-2546, 1994.

Prat, M., Percolation model of drying under isothermal conditions in porous media, *International Journal of Multiphase Flow*, 19(4):691-704, 1993.

Pruess, K., and Y.W. Tsang, On two-phase relative permeability and capillary pressure of rough-walled rock fractures, *Water Resources Research*, 26(9):1915-1926, 1990.

Pyrak-Nolte, L.J., N.G.W. Cook, and L.R. Myer, Stratified percolation model for saturated and unsaturated flow through natural fractures, *High Level Radioactive Waste Management, Proceedings of the International Topical Meeting,* American Nuclear Society, April 8-12, Las Vegas, NV, pp. 551-558, 1990.

Reitsma, S., and B.H. Kueper, Laboratory measurement of capillary pressure-saturation relationships in a rock fracture, *Water Resources Research,* 30(4):865-878, 1994.

Wilkinson, D., Percolation model of immiscible displacement in the presence of buoyancy forces, *Physical Review A,* 30(1):520-531, 1984.

Wilkinson, D., and J.F. Willemsen, Invasion percolation: a new form of percolation theory, *Journal of Physics A (Mathematical and General),* 16 (no.14):3365-3376, 1983.

APPENDIX

For each of the simulations conducted in this study, the phase invasion structure was printed when invading phase first reaches the other side of the aperture field (breakthrough for horizontal and vertical gravity destabilized cases) or when gravity forces just offset capillary forces (vertical gravity stabilized cases). In all cases, the invasion boundary is the edge at the top of the page and the grayscale sequence from dark to light depicts the order of invasion from first to last, black denotes defending fluid remaining that can still escape the network, and white the entrapped defending fluid. For all simulations, the surface tension and densities for the air water system at Standard temperature and pressure were used. Figure A1 and A2 show the baseline case of standard IP (r_2 neglected) in the horizontal fracture for fully wetting ($\alpha = 0$) and nonwetting ($\alpha = 180$) invasion processes. Subsequent figures display the effects of the modifications to invasion percolation introduced in this paper and the influence of α varied between 0, 41, 60, 74, 104, 120, 139, and 180 degrees.

Figures A3-A11: Horizontal invasion including in-plane curvature, r_2 ($\alpha = 0$, 41, 60, 74, 104, 120, 139, and 180 degrees)
Figures A12-A20: Gravity-destabilized vertical invasion neglecting in-plane curvature, r_2 ($\alpha = 0$, 41, 60, 74, 104, 120, 139, and 180 degrees)
Figures A21-A29: Gravity-destabilized vertical invasion including in-plane curvature, r_2 ($\alpha = 0$, 41, 60, 74, 104, 120, 139, and 180 degrees)
Figures A30-A38: Gravity-stabilized vertical invasion neglecting in-plane curvature, r_2 ($\alpha = 0$, 41, 60, 74, 104, 120, 139, and 180 degrees)
Figures A39-A47: Gravity-stabilized vertical invasion including in-plane curvature, r_2 ($\alpha = 0$, 41, 60, 74, 104, 120, 139, and 180 degrees)

For gravity destabilized cases, as invasion proceeds into the network from the edge at the top of the page, each simulation can be interpreted as either water moving downward into a air filled vertical fracture above the water table or, by reversing orientation within the gravity field, air moving upward into a water filled fracture below the water table.

For gravity stabilized cases, we stop invasion for the gravity stabilized cases when gravitational forces just offset capillary forces thereby yielding an equilibrium capillary rise (or depression) structure for the fracture. As invasion proceeds into the network from the edge at the top of the page, each simulation can be interpreted as either water moving upward or air moving downward. The reference point for the gravity potential at the supply surface (top of the page) and at the far end of the network (bottom of the page) is given in each figure; gravity forces increase linearly with distance into the fracture. Zero gravity potential references where a free surface for the air-water system would lie without capillary forces.

The gravity stabilized simulations can be interpreted for water invasion as follows. Consider the fracture oriented vertically at a location with respect to the free water surface given by the supply potential (i.e., rotate the figure 180 degrees and hold it up vertically so that the water enters from the bottom of the fracture). The invading water is connected hydraulically to the free water at the entry potential while the air is hydraulically connected to the air above the free surface. A supply potential of 0.0 means that the invasion boundary is just touching the free water surface while a negative or positive supply potential means that the fracture invasion boundary is either below or above the free water surface, respectively. Invasion above 0.0 indicates that capillary forces pull

the water above the free water surface to a height given by the distance of invasion into the network (the situation for water as the wetting phase). Invasion from a negative potential at the supply edge to a location that does not reach 0.0 indicates that capillary forces oppose invasion of water into the network causing a capillary depression below the free water surface given by sum of the distance of invasion into the network and the supply potential (the situation for water as the nonwetting phase).

To interpret gravity stabilized simulations for air invasion, the reverence locations are reversed (multiply all positions by -1, hold the figure up vertically in its current orientation). The defending water is connected hydraulically through the bottom of the fracture network to the water table and air enters the fracture from above. Invasion from 0.0 to a positive value becomes invasion from 0.0 to a negative value indicating that capillary forces pull the air into the fracture to a depth below the free surface given by the distance into the network (the situation for air as the wetting phase). Invasion from a negative potential to below 0.0 now becomes invasion from a positive potential to above 0.0 indicating that capillary forces work to repulse invasion of the fracture with air yielding air invasion that stops above the free surface (the situation for air as the nonwetting phase).

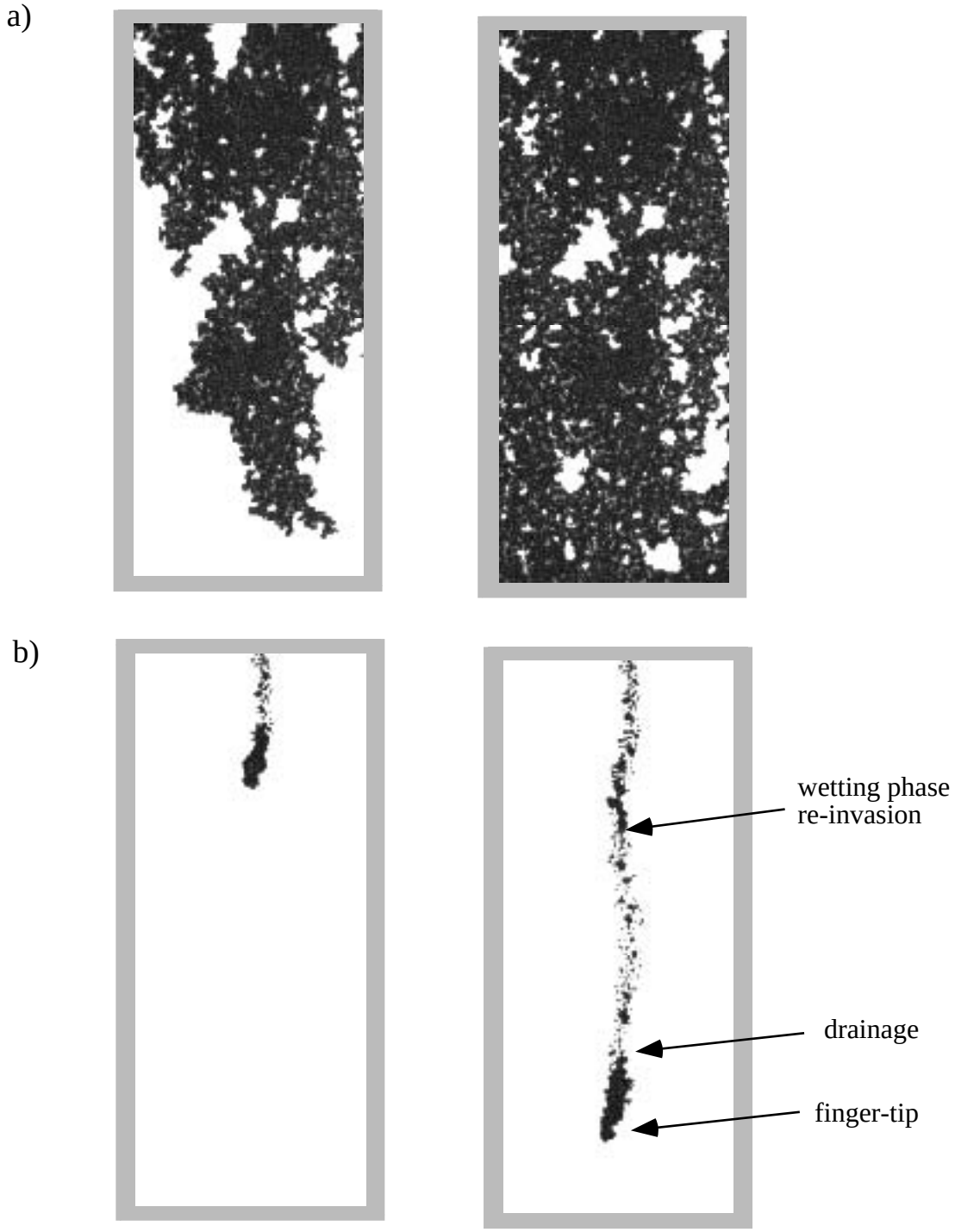

Figure 1: Experimental observation of slow wetting phase invasion. A transparent analog fracture filled with a clear nonwetting fluid (air) is invaded by a denser dark wetting fluid (dyed water) supplied at low flow rate from a single point source on the top edge of the fracture; an approximately 116 by 280 mm section of the 152 by 305 mm fracture is shown. a) Where the fracture is horizontal, wetting phase invasion forms complicated but macroscopic phase structures in which significant amounts of the defending fluid are entrapped (experiment F109, flow rate = 0.024 ml/minute) images shown were collected 260 and 380 minutes after the initiation of flow (near breakthrough and satiated end point, respectively). b) Where the fracture is vertical, gravity-driven fingers result (experiment F41, flow rate = 0.025 ml/minute); images shown were collected at 150 and 450 seconds after the initiation of flow (from the experiments of Nicholl et al., 1993a).

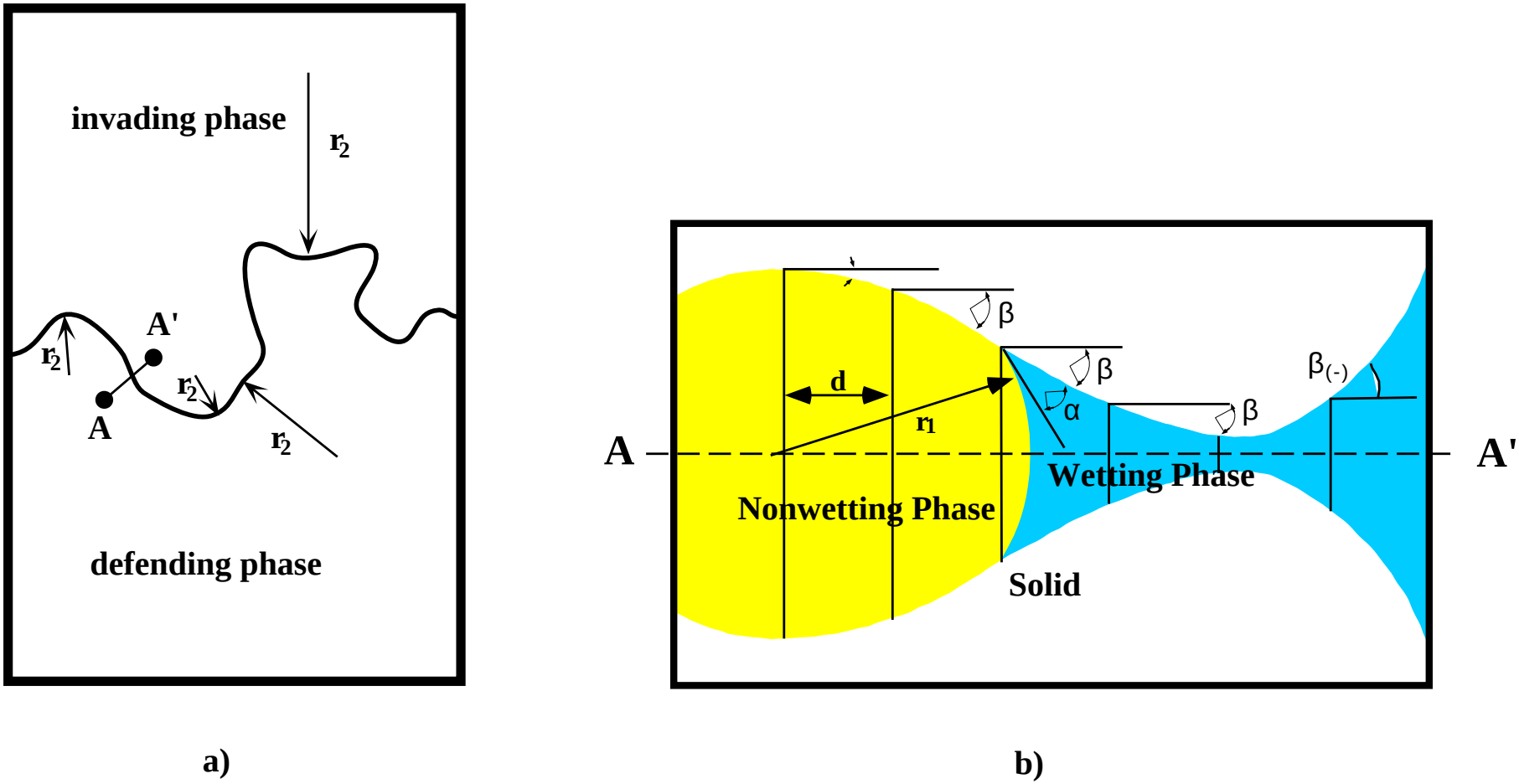

Figure 2: Definition of r_1 and r_2. The interface within a fracture as seen looking down on (perpendicular to) the fracture plane is shown in a). This view is the same as seen in **figure 1**. Local in-plane curvature r_2 is shown at 4 different locations along the interface between the invading and defending phase. Note that the sign of r_2 will vary as well as its local magnitude. The conceptual drawing in b) shows a local fluid-fluid interface blown up along the transect A-A' in a) as seen from its edge cut perpendicular to the fracture plane. Fracture (and hence fluid) geometry are conceptualized as being symmetric about a central plane (dashed line). The contact angle (α), convergence/divergence angle (β), and r_1 are defined in this plane; vertical lines illustrate discretization of the aperture field with a grid spacing of (d).

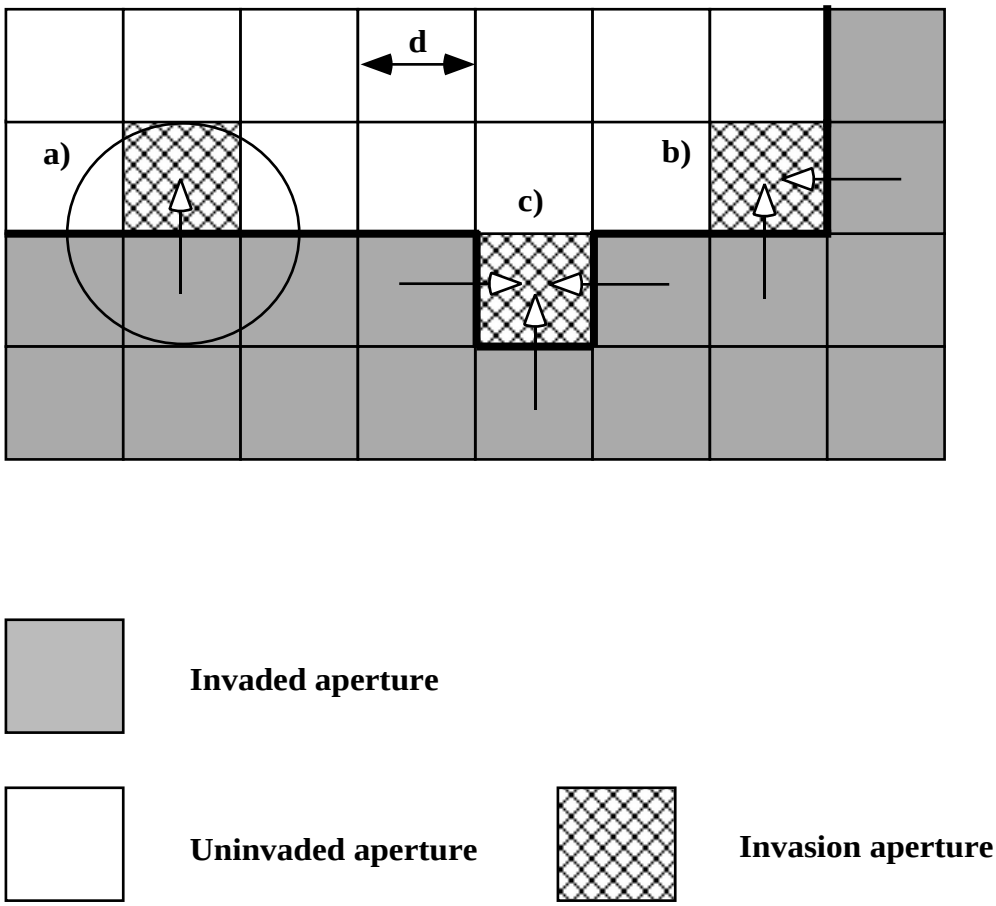

Figure 3: Simple adjacency model for r_2 (Glass, 1993). The view is looking down onto a gridded fracture plane with aperture centers separated by a distance (d); gray indicates the invading fluid (invaded aperture), white the defender (uninvaded aperture), and hatched a potential invasion step (invasion aperture). a) Where only one filled aperture is adjacent to the potential invadee, the post-invasion interface will exhibit a sharp curvature; hence, r_2 will oppose invasion and is estimated to be on the order of d (circle of radius d drawn for comparison). For two (b) and three (c) adjacent filled apertures, the final configuration is taken to be flat, or nearly flat with a negligible effect on invasion potential ($r_2 >> d$).

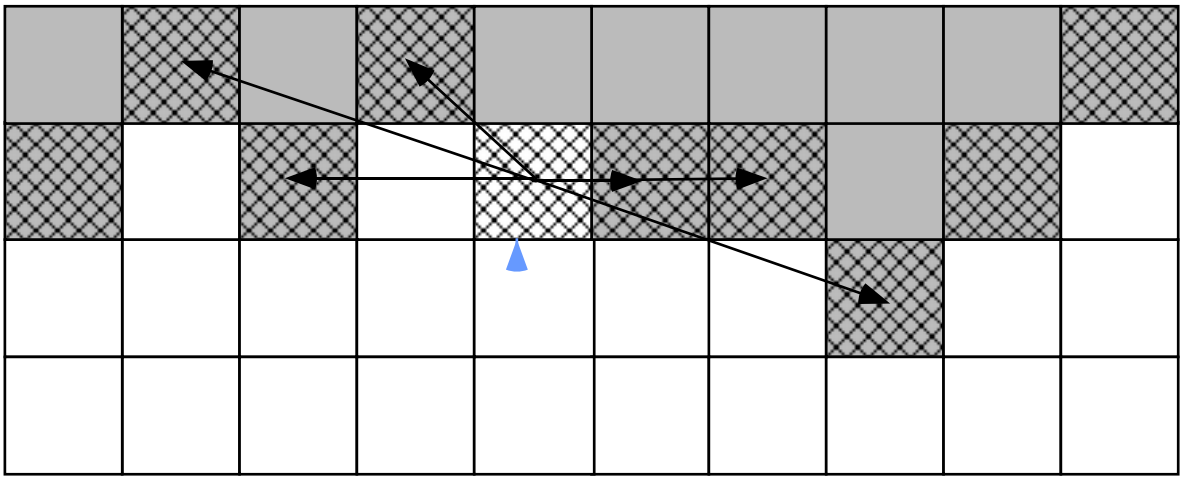

a) vectors from invasion aperture to other apertures on the interface

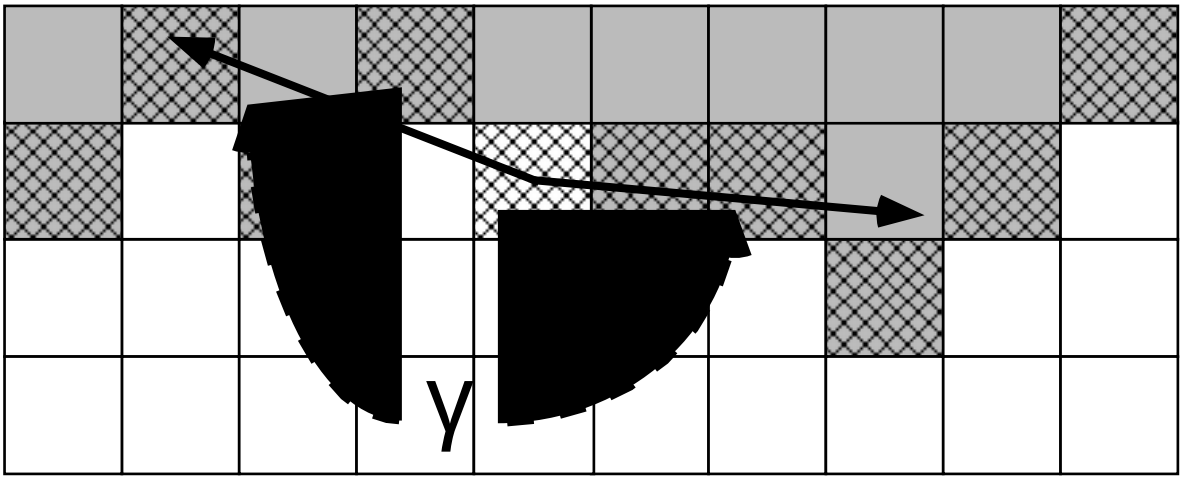

b) resultant average vectors that estimate the local interface with included angle γ

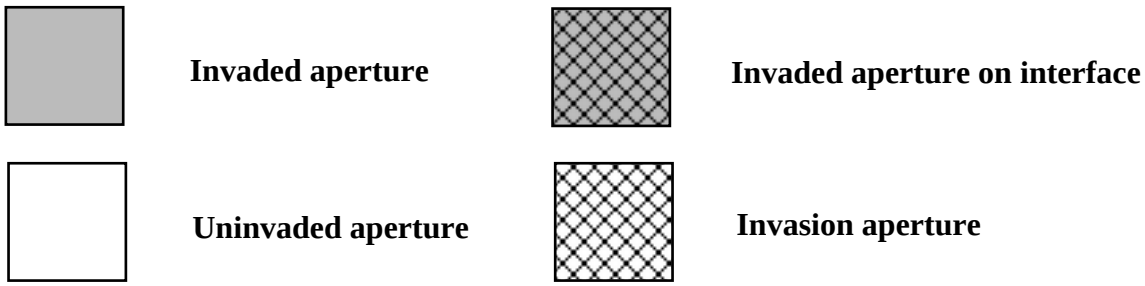

Figure 4a, b: New conceptual model for r_2. The view is looking downward onto a gridded aperture field, individual grid blocks shown in gray represent the invading fluid, hatched gray are invaded apertures on the interface, and white is the defender fluid; the hatched white block is the one for which an invasion potential is calculated. a) shows the vectors from the potential invasion aperture to apertures up to three positions away both to the right and to the left along the interface. b) The included angle γ is determined by a weighted average of unit vectors representing those shown in a). The weighting factor is calculated as the reciprocal of the neighbor number (1 for nearest, 2 for next nearest, etc.) raised to a power.

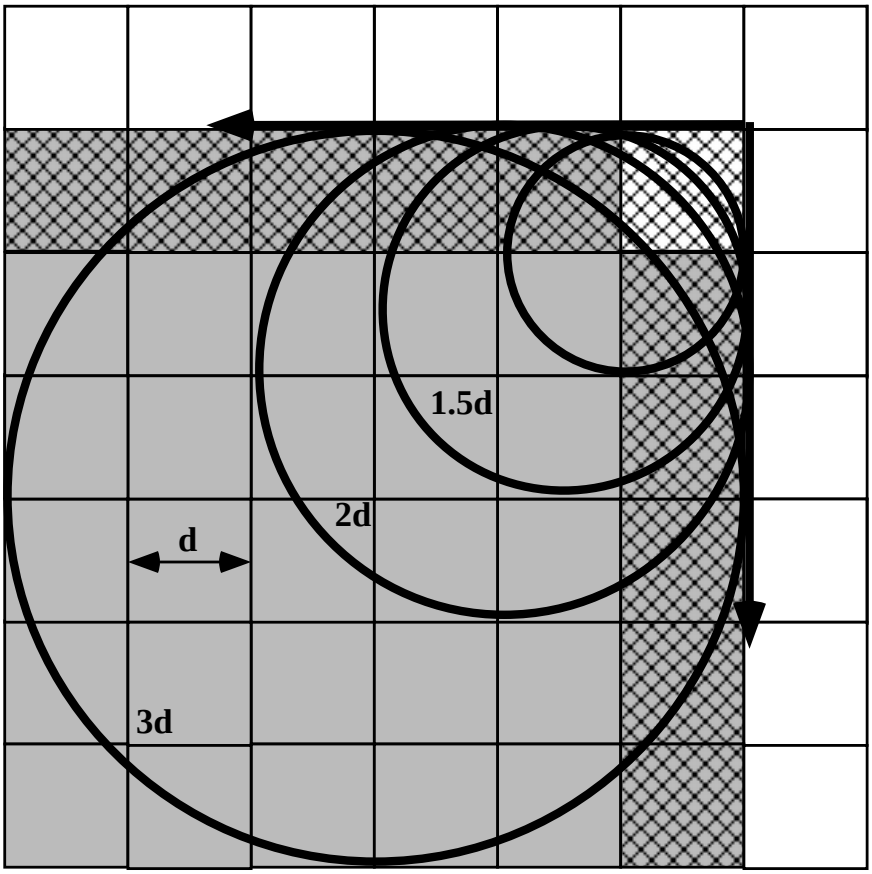

c)

Figure 4c: New conceptual model for r_2 (continued). In c) the configuration where g is 90 degrees and $d_* = r_2$ is shown along with curvatures given by 1d, 1.5d, 2d, and 3d, where d is the grid spacing.

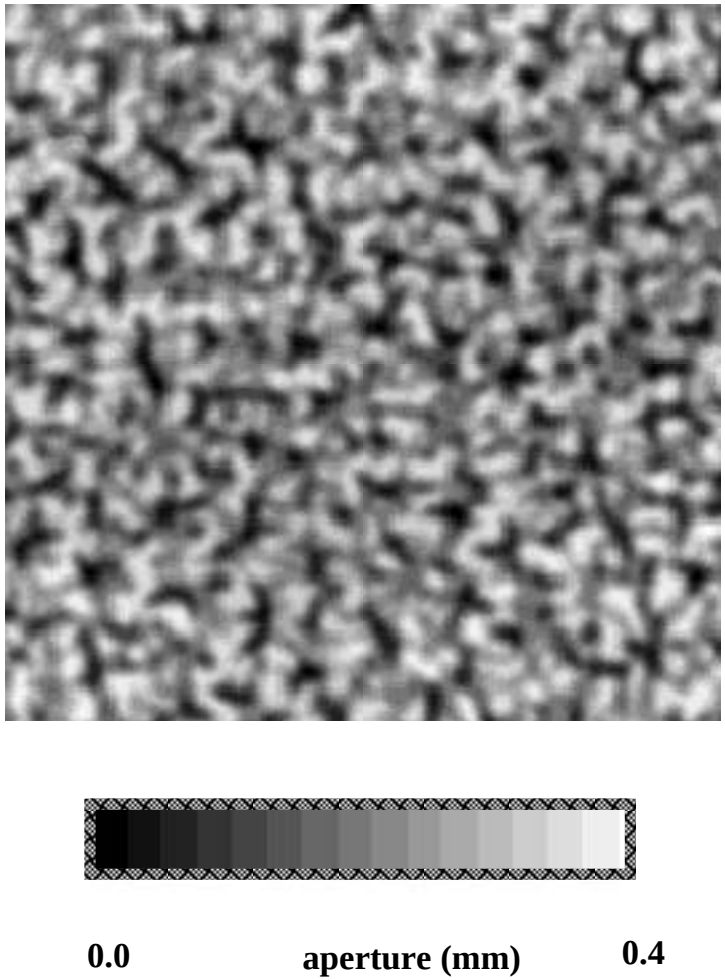

a)

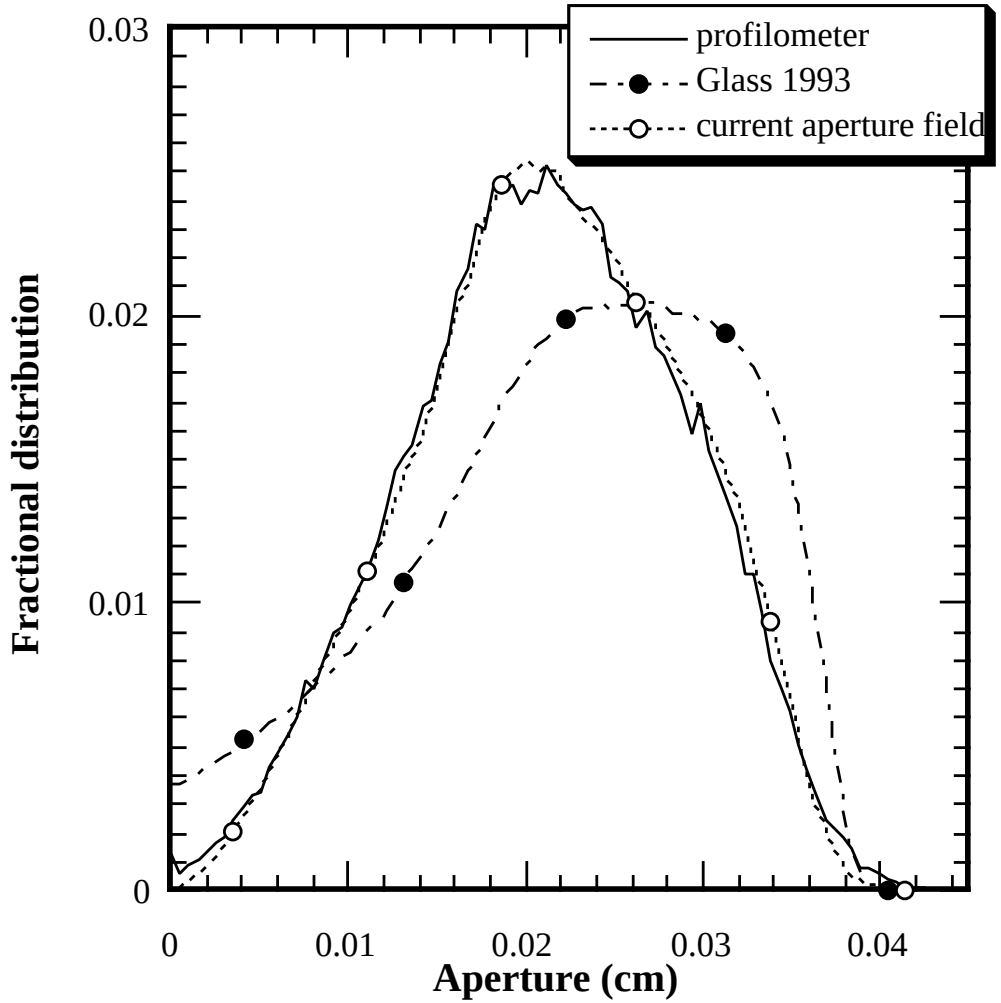

b)

Figure 5: Aperture field used for simulations. a) A 256 by 256 pixel (25.6 x 25.6 mm) segment of the 2048 by 1024 aperture field measured through transmitted light imaging. b) Normalized histogram of the 1024 by 512 portion of the aperture field used in our simulations. Glass (1993) presented a model of this aperture field based on surface roughness measurements collected at 0.1 mm spatial resolution from a 25.6 x 25.6 mm sample of the textured glass. The normalized distribution for that laser profilometer based model is nearly identical to that of the larger field used in our simulations. This observation is consistent with our expectation of a statistically homogeneous aperture field, and in that light provides independent confirmation of the transmitted light measurement technique. Also shown is an earlier estimation of this aperture field (Glass, 1993) based on images in which the fracture was filled with a fluid that was inconsistent with the assumption of linearity inherent in Lambert's Law for light absorption.

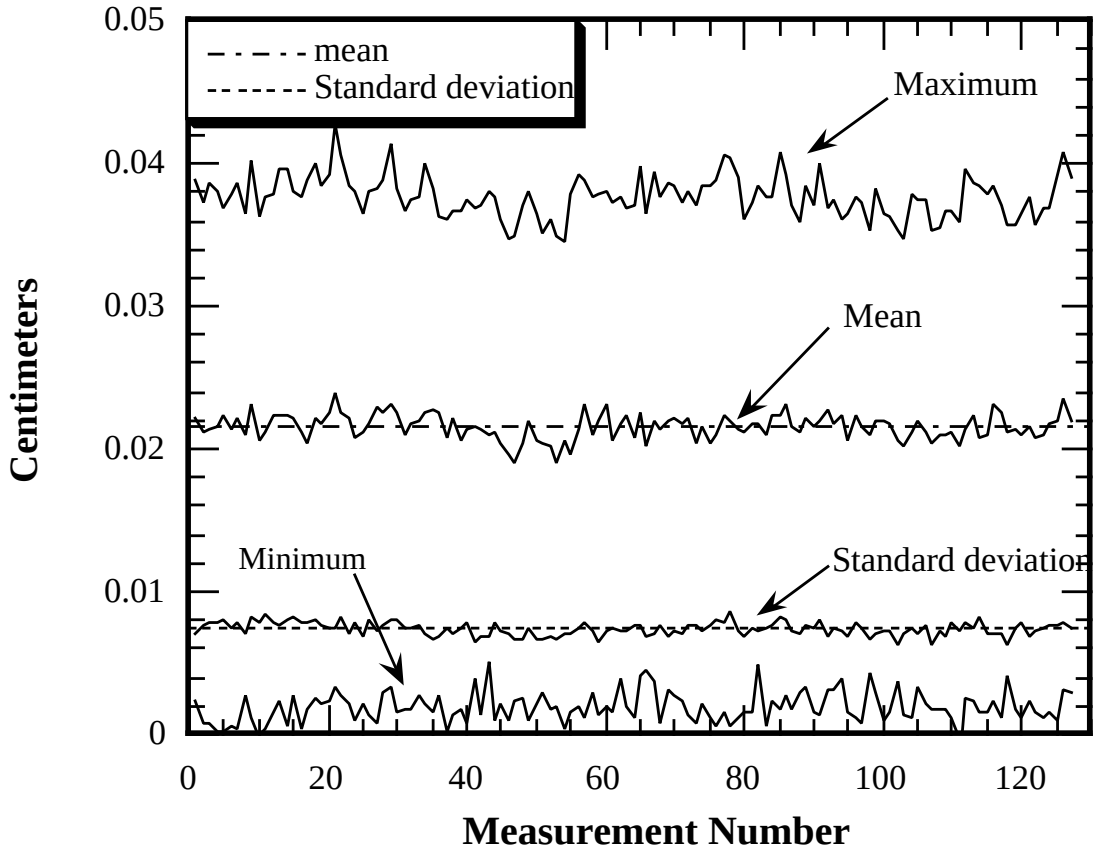

Figure 6: Homogeneity of the aperture field. The 1024 by 512 portion of the aperture field used for our simulations was subdivided into 128 sub-regions, each 64 by 64 pixels in size. Summary statistics (mean, standard deviation) of the sub-regions (shown as solid lines) are consistent with those of the population (shown as dashed lines), thereby implying homogeneity. In a statistically homogenous system, it is expected that minimum and maximum values for sub-samples will show more variation than the summary statistics; the data above shows increased, but not extreme variation relative to the summary statistics.

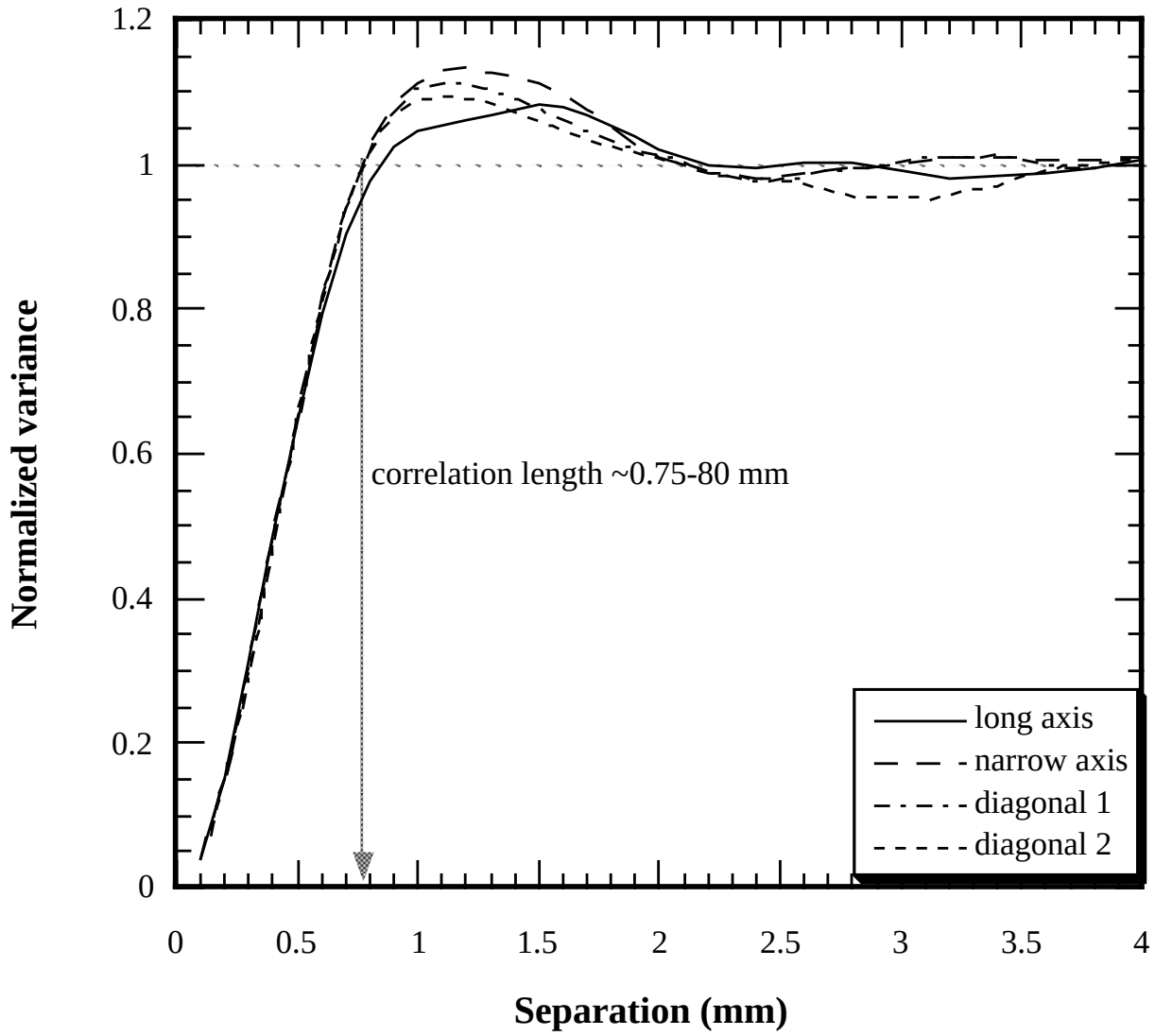

Figure 7: Spatial correlation within the aperture field. Normalized semivariance was measured on the aperture field used in our simulations. Measurements were taken along the two principal axes and the two primary diagonals at separations of up to 1/2 the system length as measured in the relevant direction. Data shows a very well defined positive correlation at the sub-millimeter scale (< ~0.8 mm) and an apparent negative correlation (semivariance exceeds population variance)at a slightly larger scale. The textured glass forms an aperture field characterized by similarly sized local regions of large or small aperture that occur in a variety of shapes (**see figure 5**). Because these regions will have a strong internal correlation and be of similar size, separation distances slightly larger than the regions will likely connect regions of small and large aperture, thereby resulting in an apparent negative correlation.

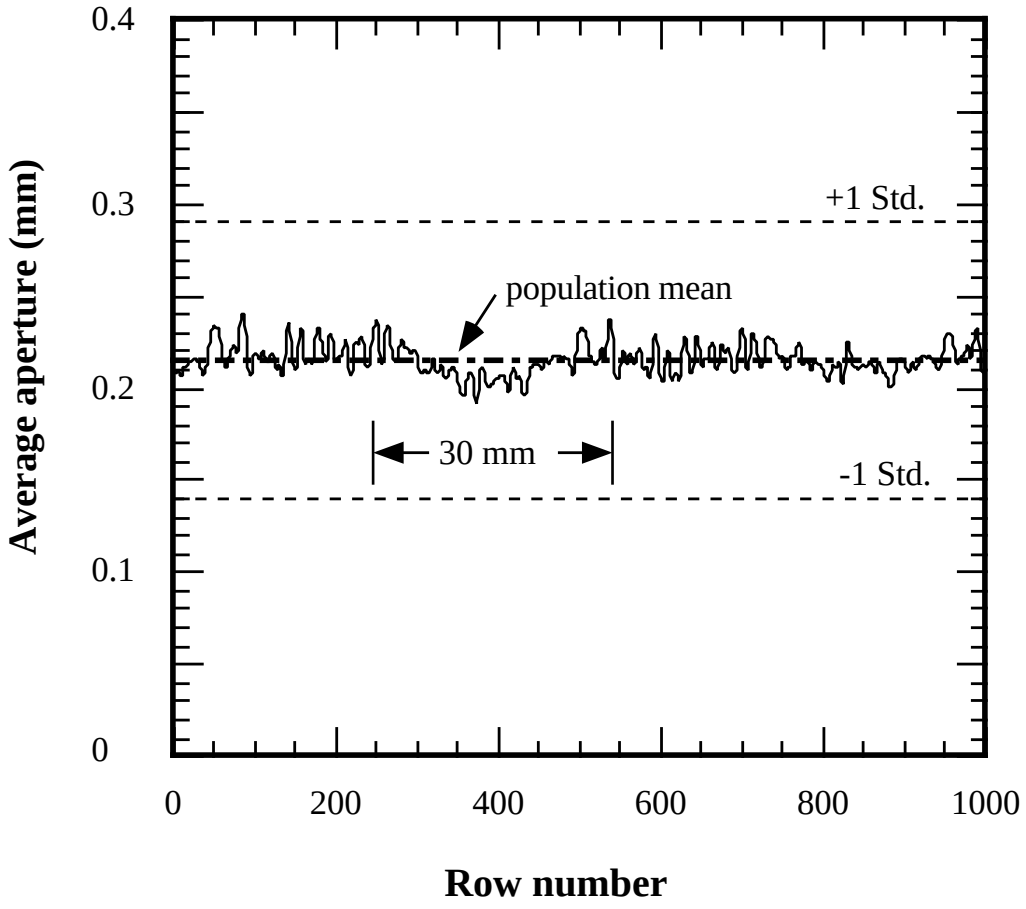

Figure 8: Average transect of the aperture field. Possible trends in the aperture field with fracture length and width were evaluated by averaging each row and column and compared the result to the population mean; for clarity only the row averages are shown. Neither row nor column averages showed any significant trend, and variation about the population mean (heavy dashed line) is small with respect to the population standard deviation (+/- 1 Std. are shown with light dashed lines). However, for the rows, there does appear to be a very slight sinusoidal variation in the data with a wavelength on the order of 30 mm.

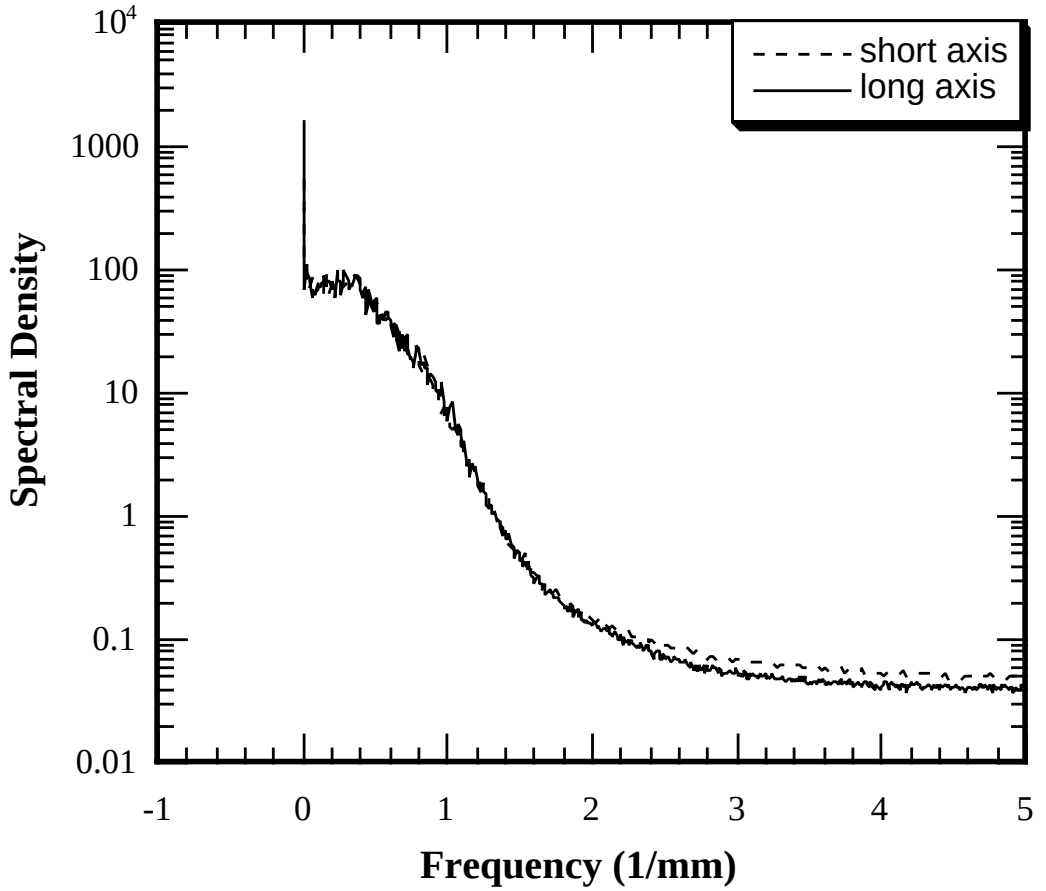

Figure 9: Spectral analysis of the aperture field. The one-sided power spectral density (PSD) function was estimated for the 1024 by 512 portion of the aperture field used in the simulations; for illustrative purposes, the PSD was averaged along transects of both primary axes and is displayed as a function of frequency (1/wavelength). As expected, the spectra in both directions are nearly coincident, indicating isotropy. Shape of the PSD is consistent with a strong auto-regressive component (e.g., short-range correlation structure), but is inconclusive with regard to longer wavelength features such as that seen in **figure 8.**

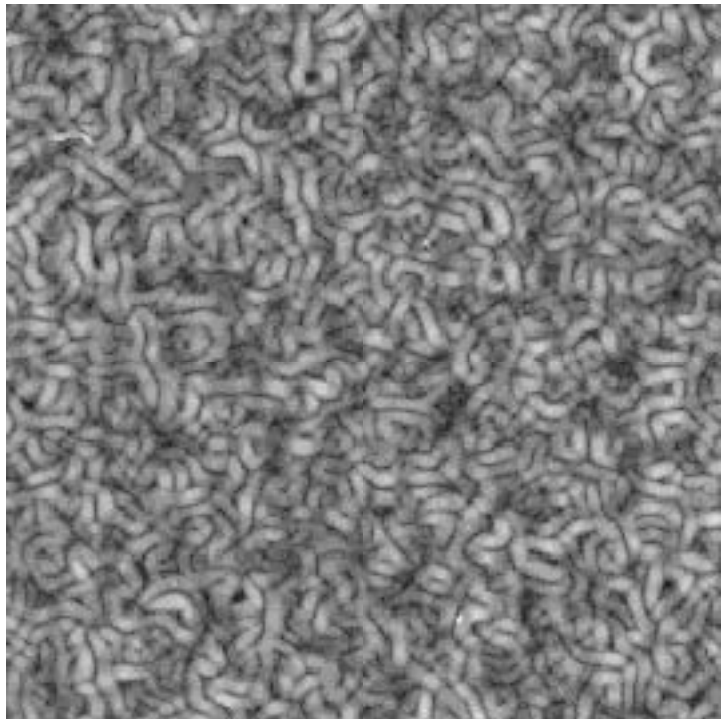

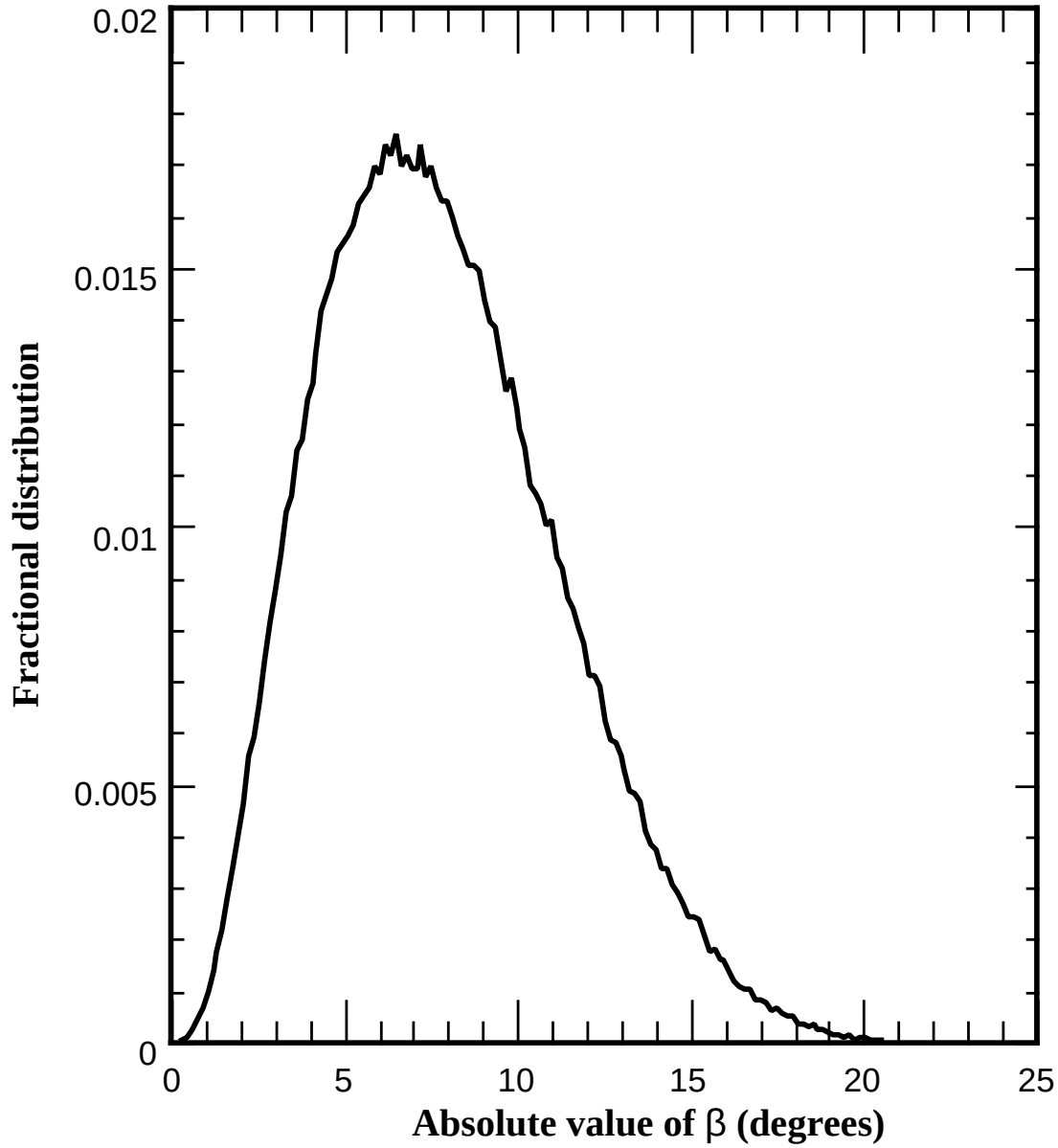

Figure 10: Convergence/divergence of the aperture field. Assuming that aperture variation is symmetric about a mean plane (see **figure 2**), we can calculate the convergence/divergence angle, β, for the same region shown in **figure 5**. The dark lines represent nearly flat regions located along the 'crests' and 'troughs' of the aperture field, while the lighter areas represent the transition between large and small aperture regions. A histogram of the absolute value of β for the 1024 by 512 portion of the aperture field used in the simulations is shown on the right.

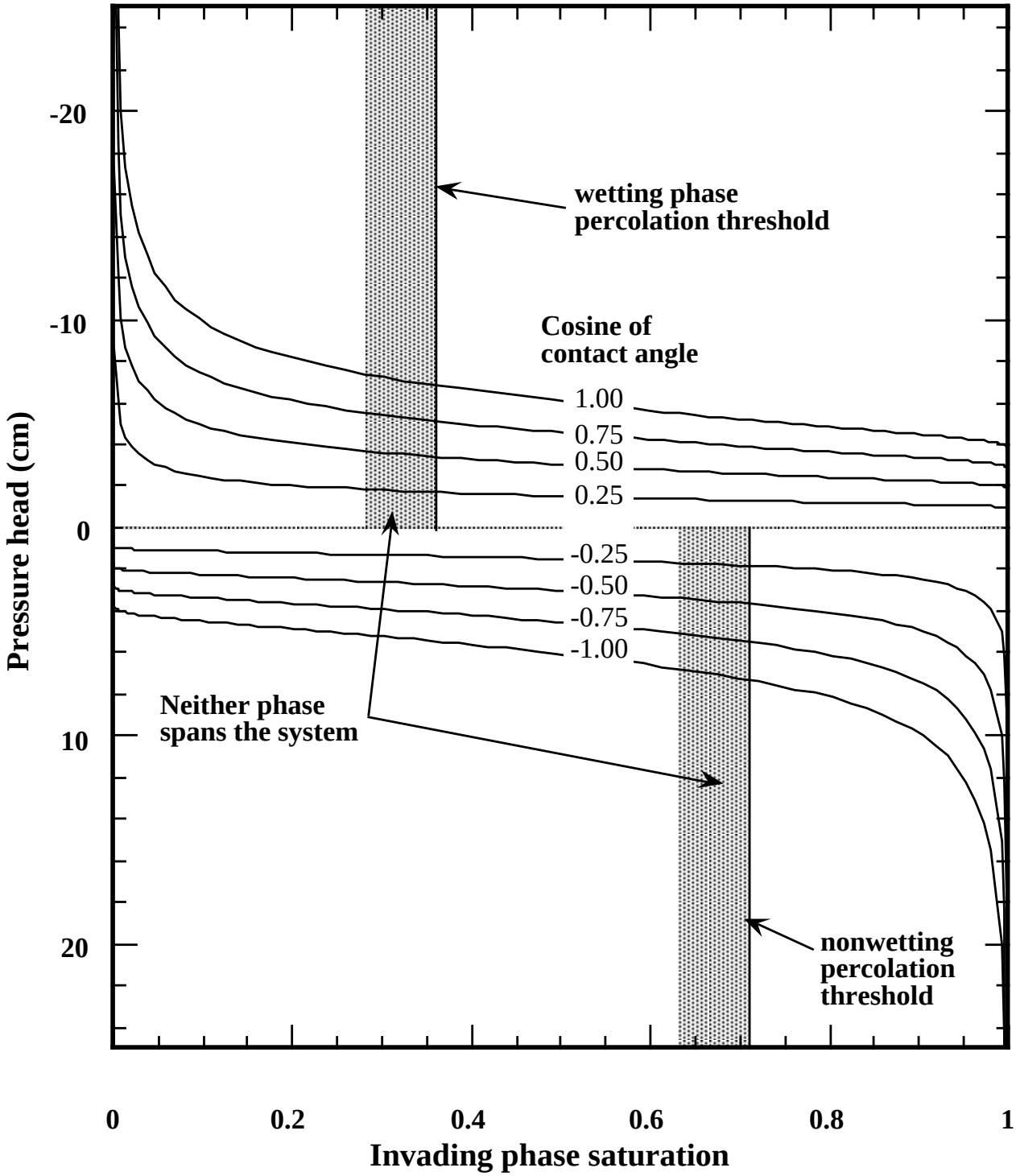

Figure 11: Pressure-saturation relationship for Standard Percolation (SP). Assuming that the La Place-Young relationship neglecting r_2 holds for each gridblock in the aperture field independent of connection to a phase source or sink allows calculation of pressure-saturation relationships for both wetting and nonwetting invasion using SP; pressure is given in cm of water. Note the higher nonwetting phase saturation required to span the system and that there is a range of pressures for which the system is not spanned by either phase (shaded regions).

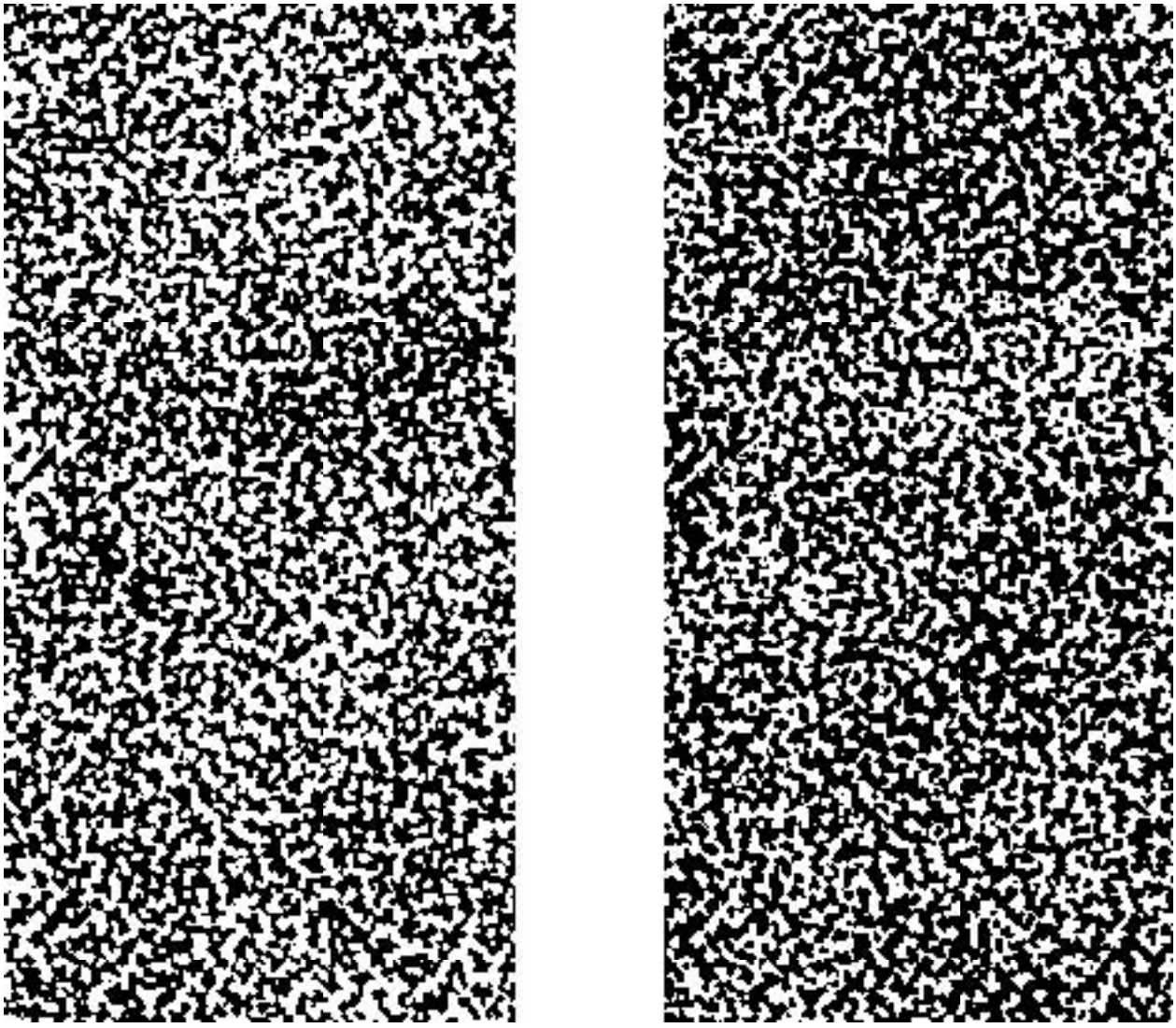

a) b)

Figure 12: Phase structures at percolation for standard percolation. a) Wetting phase invasion creates a phase structure that percolates (spans the system) when all apertures smaller than 0.22 mm are invaded. b) The nonwetting phase percolates when all apertures larger than 0.20 have been invaded. Black denotes the invaded phase in both a and b (wetting and nonwetting, respectively). The slight periodic (~30 mm) variation along the fracture length noted in **figure 8** is visible at the percolation threshold.

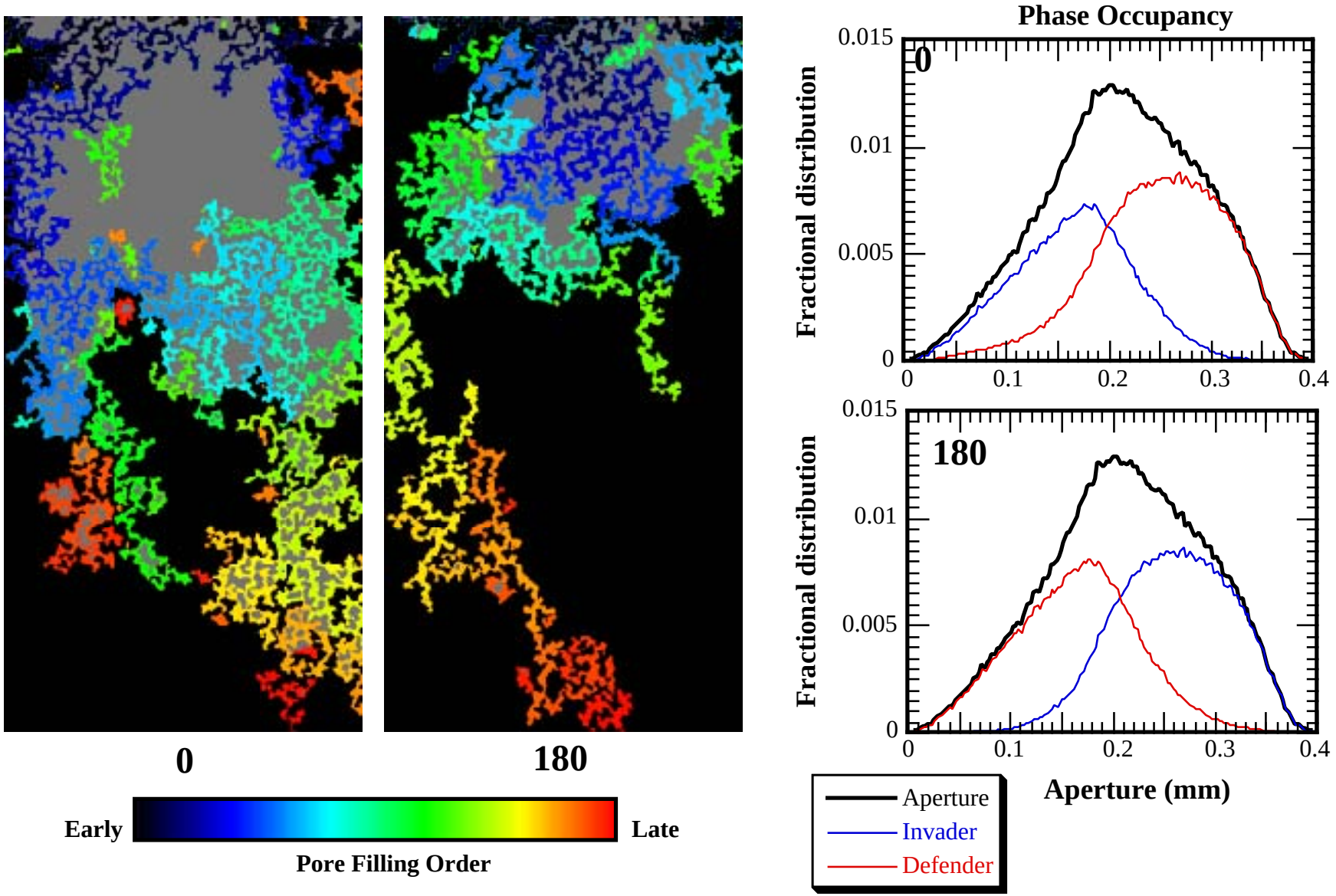

Figure 13: Horizontal invasion neglecting in-plane curvature (r_2). Fully wetting and nonwetting (α = 0, 180 degrees respectively) invasions are shown for illustrative purposes. The color sequence shows the invasion history at breakthrough and gray indicates entrapped defender fluid. The graphs show the distribution of apertures that are occupied by the invading and defending phases in the final satiated state; the aperture distribution (thick black line) is shown for comparison. Both wetting and nonwetting invasions form complicated structures with relatively narrow 'tendrils'. Note that the wetting invasion is significantly more complicated than seen experimentally (see **figure 1a**). There is significant overlap between the phase occupancies of the wetting and nonwetting fluids. This is a significant departure from SP which would predict zero overlap; also note that the phase occupancy distributions are remarkably similar for both cases.

13-Side_IPoff_0-180

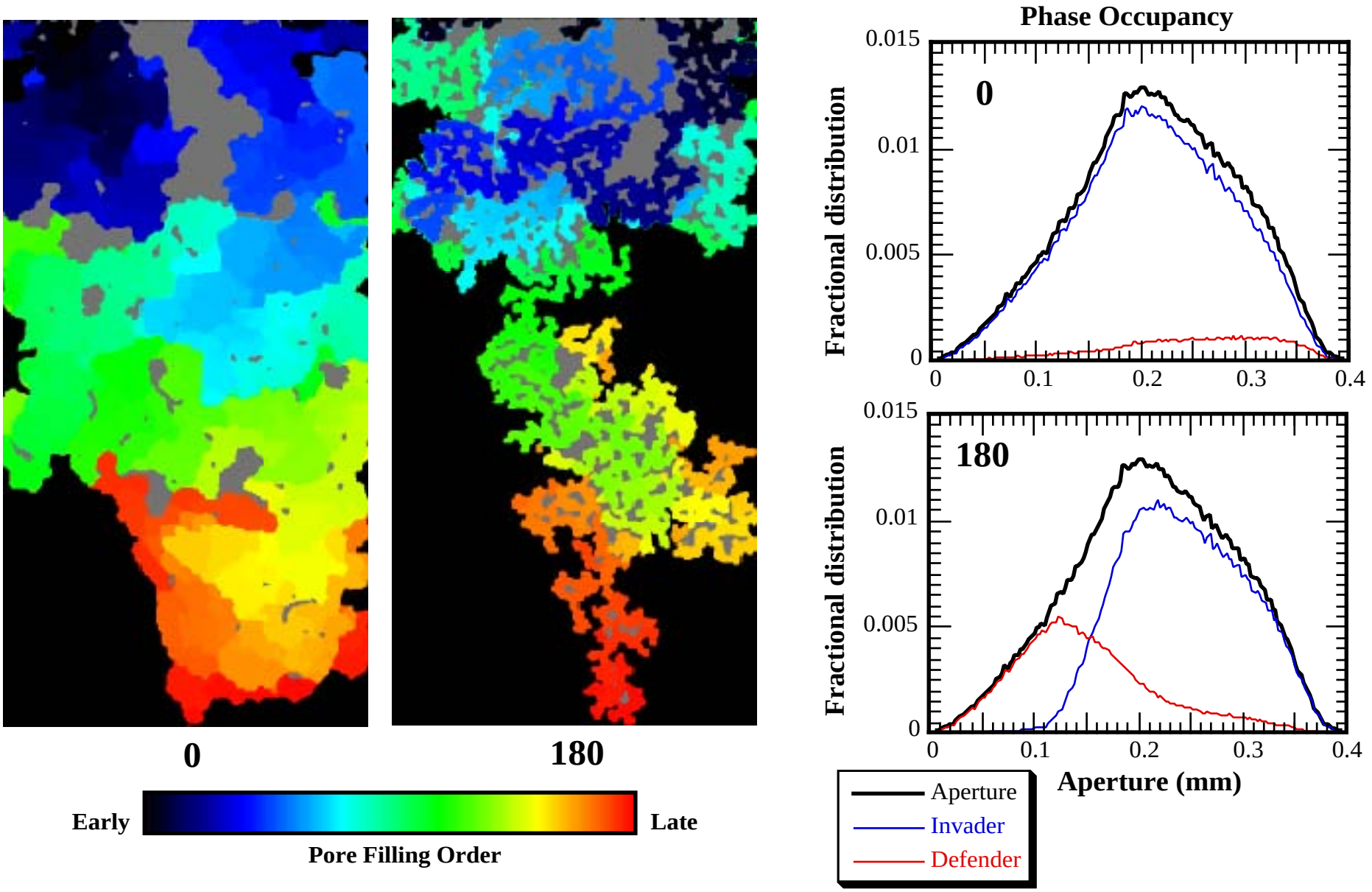

Figure 14: Horizontal invasion including in-plane curvature (r_2). Fully wetting and nonwetting (α = 0, 180 degrees respectively) invasions are shown. The color sequence shows the invasion history at breakthrough and gray indicates entrapped defender fluid. The graphs show the distribution of apertures that are occupied by the invading and defending phases in the final satiated state; the aperture distribution (thick black line) is shown for comparison. Inclusion of r_2 results in more compact structures, particularly for the wetting fluid. Note also that phase occupancy distributions differ significantly between the wetting and nonwetting invasions.

14-Side_IPon_0-180

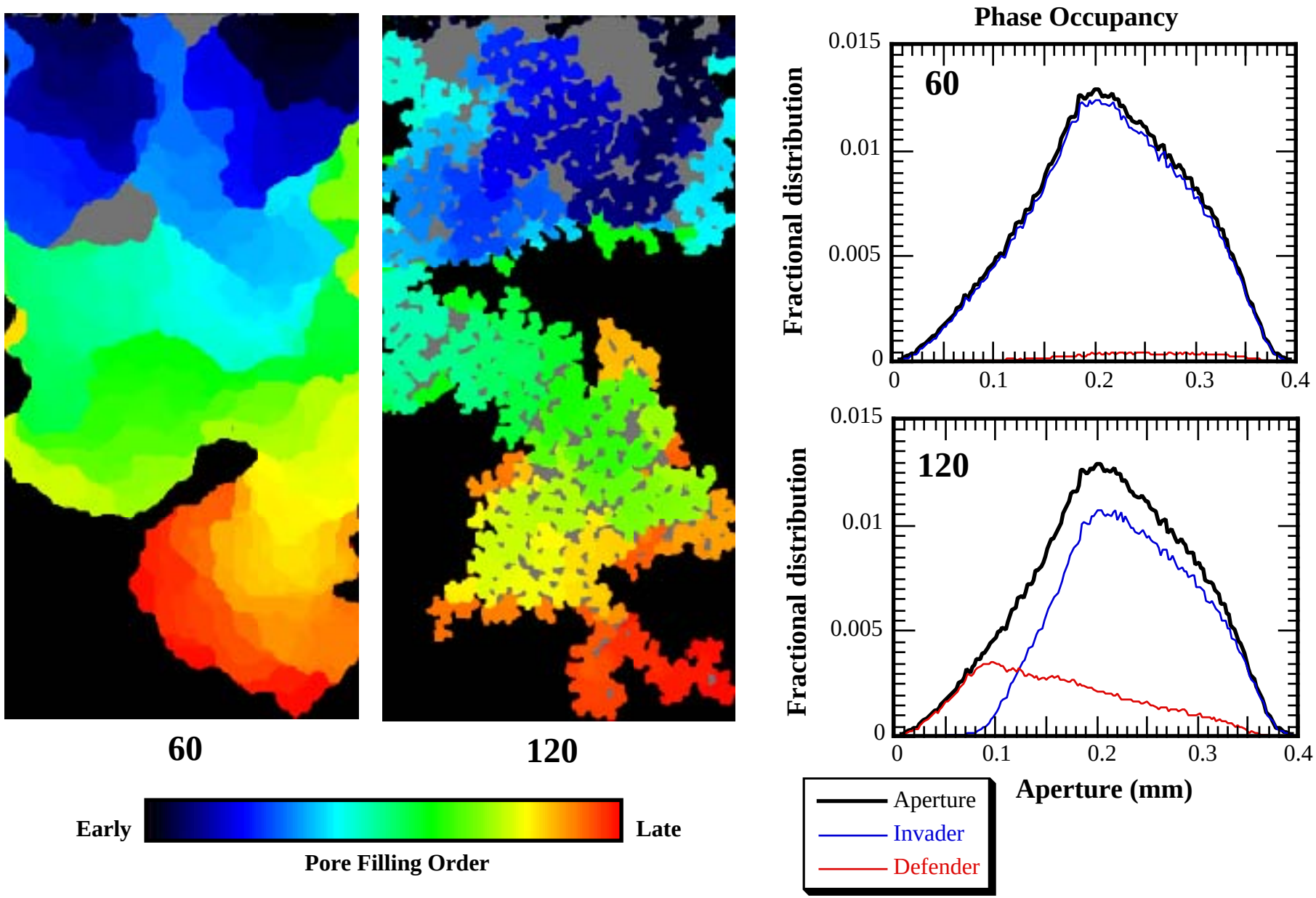

Figure 15: Horizontal invasion including in-plane curvature (r_2). Intermediate wetting and nonwetting (α = 60, 120 degrees respectively) invasions are shown. The color sequence shows the invasion history at breakthrough and gray indicates entrapped defender fluid. The graphs show the distribution of apertures that are occupied by the invading and defending phases in the final satiated state; the aperture distribution (thick black line) is shown for comparison. Note the decreased entrapment over the fully wetting and nonwetting cases.

15-Side_IPon_60-120

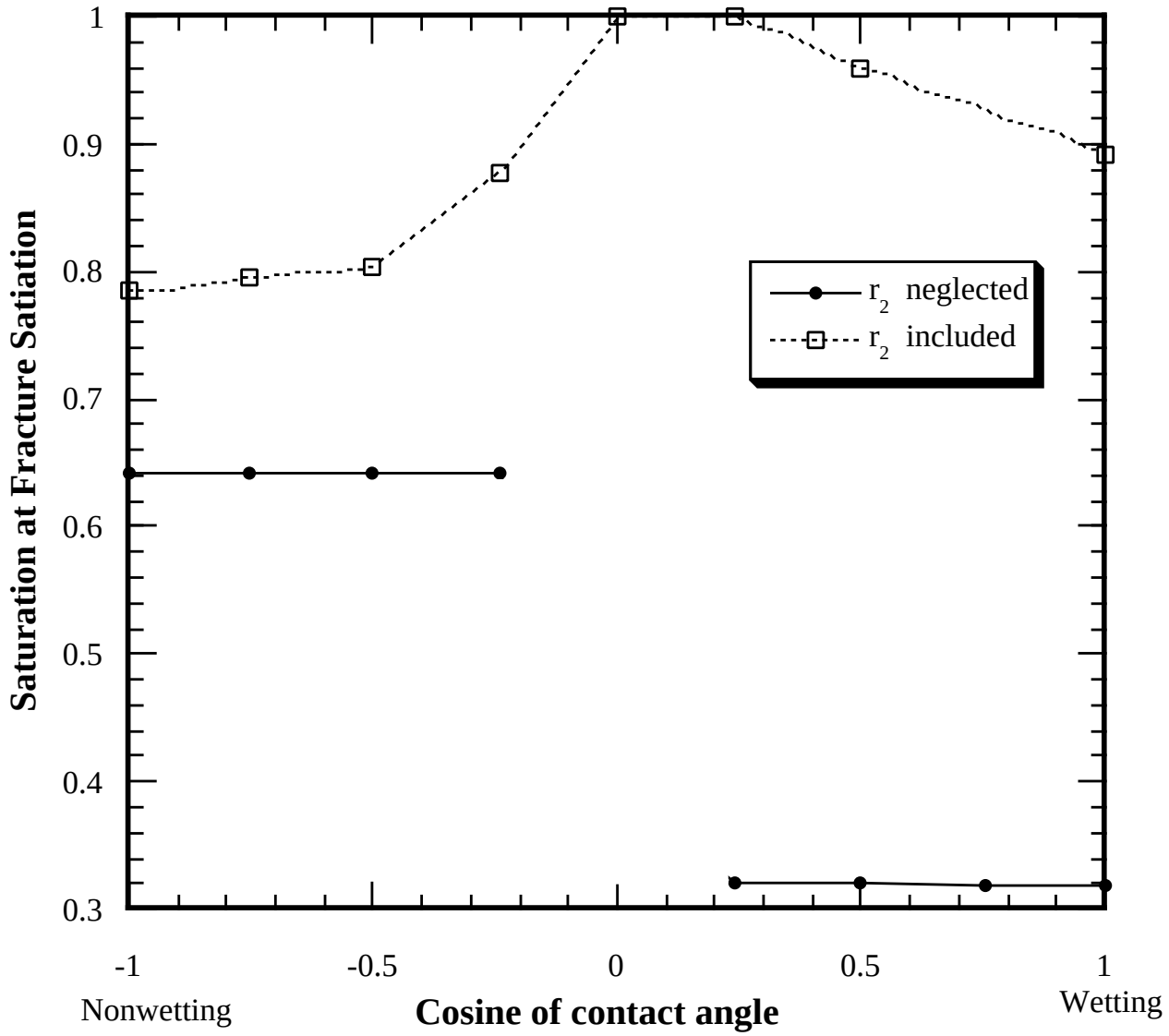

Figure 16: Horizontal invasion phase saturation at fracture satiation. At the conclusion of invasion the fracture is satiated; i.e., all apertures are either filled with the invading fluid or entrapped defender fluid. Inclusion of in-plane curvature (r_2) is observed to result in increased invading phase saturation at all contact angles; this effect is particularly significant for wetting phase invasion.

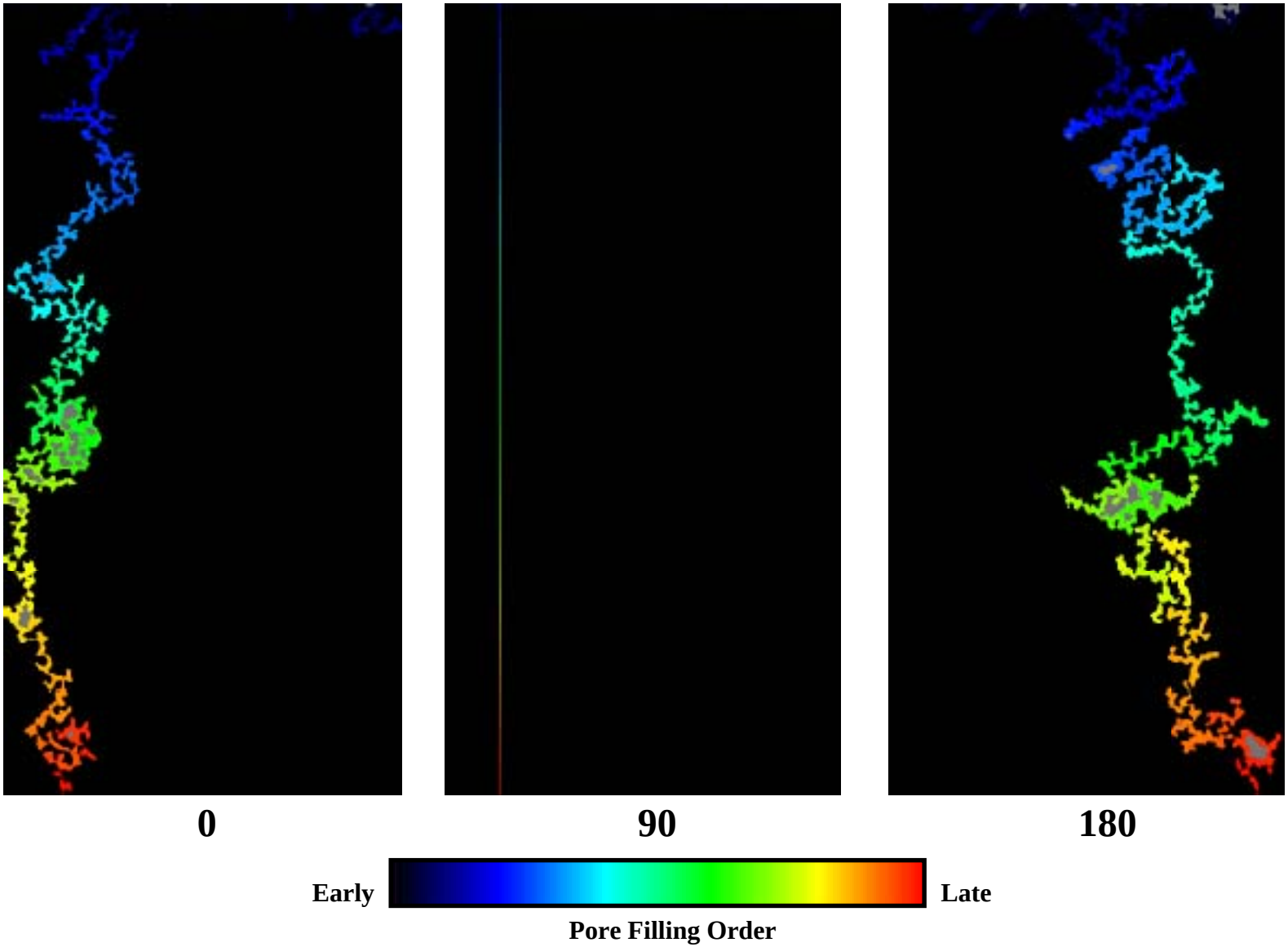

Figure 17: Gravity-destabilized vertical invasion neglecting in-plane curvature (r_2). Fully wetting, neutral, and fully nonwetting (α = 0, 90, 180 degrees respectively) invasions at breakthrough are shown. Gravity acts to destabilize invasion, leading to the formation of gravity-driven fingers. Where gravity is the sole control on invasion (α = 90) the finger is a single pixel wide. The fully wetting and nonwetting (α = 0, 180 respectively) fingers look remarkably similar in character. Note that the wetting finger (α = 0) is much more complicated than found experimentally (see **figure 1b**).

17-Down_IPoff

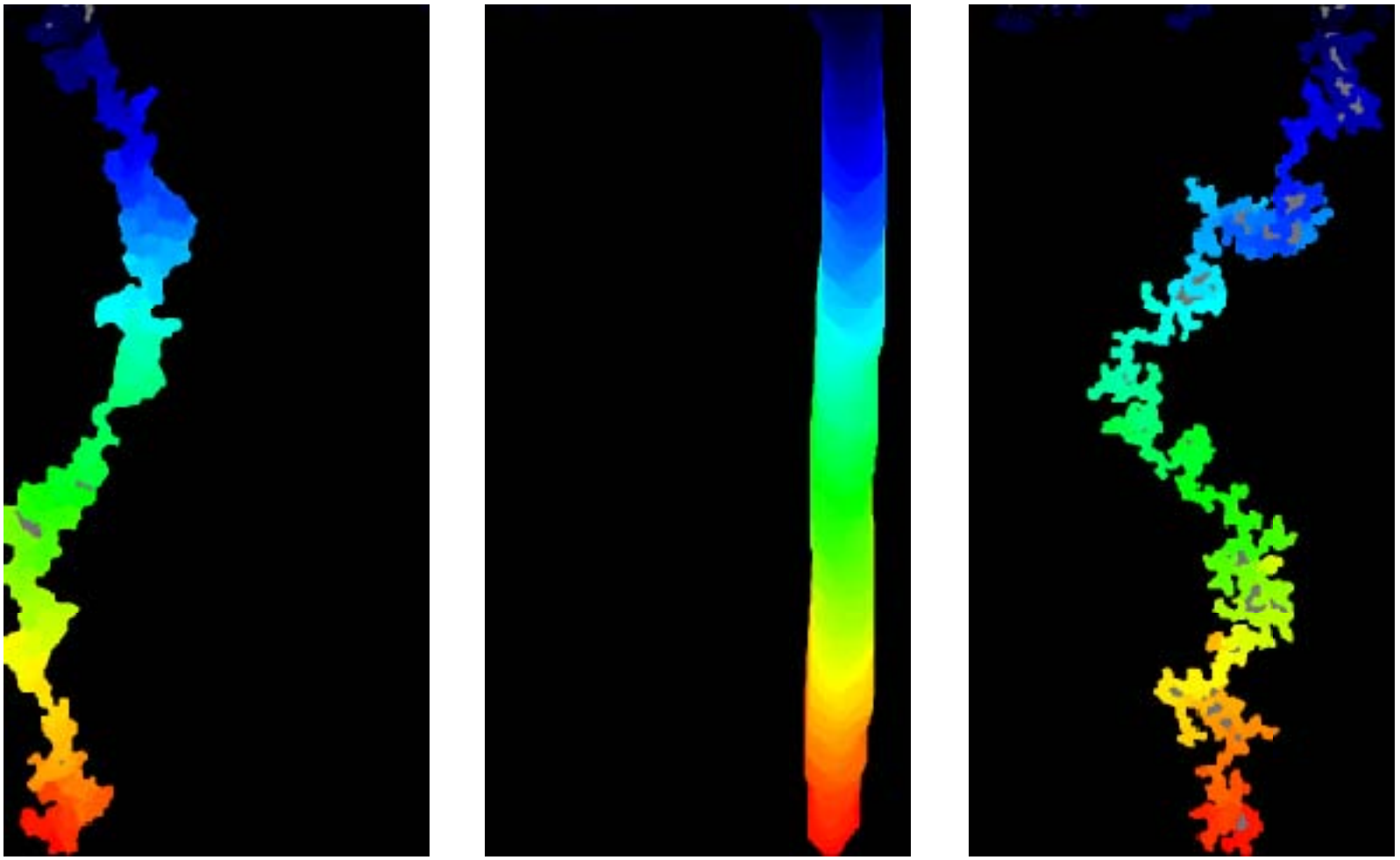

Figure 18: Gravity-destabilized vertical invasion including in-plane curvature (r_2). Fully wetting, neutral, and fully nonwetting (α = 0, 90, 180 degrees respectively) invasions at breakthrough are shown. Gravity acts to destabilize invasion, leading to the formation of gravity-driven fingers. Inclusion of r_2 makes the fingers more compact (macroscopic) and results in significantly different behaviors for wetting and nonwetting invasions (α = 0, 180 respectively). The wetting finger (α = 0) more closely resembles the experimental finger shown in **figure 1** than does the simulation shown in **figure 17**. Note also that for neutral wettability (α = 90) the fracture becomes a Hele-Shaw cell with finger width determined by the ratio of in-plane curvature to gravity forces.

18-Down_IPon

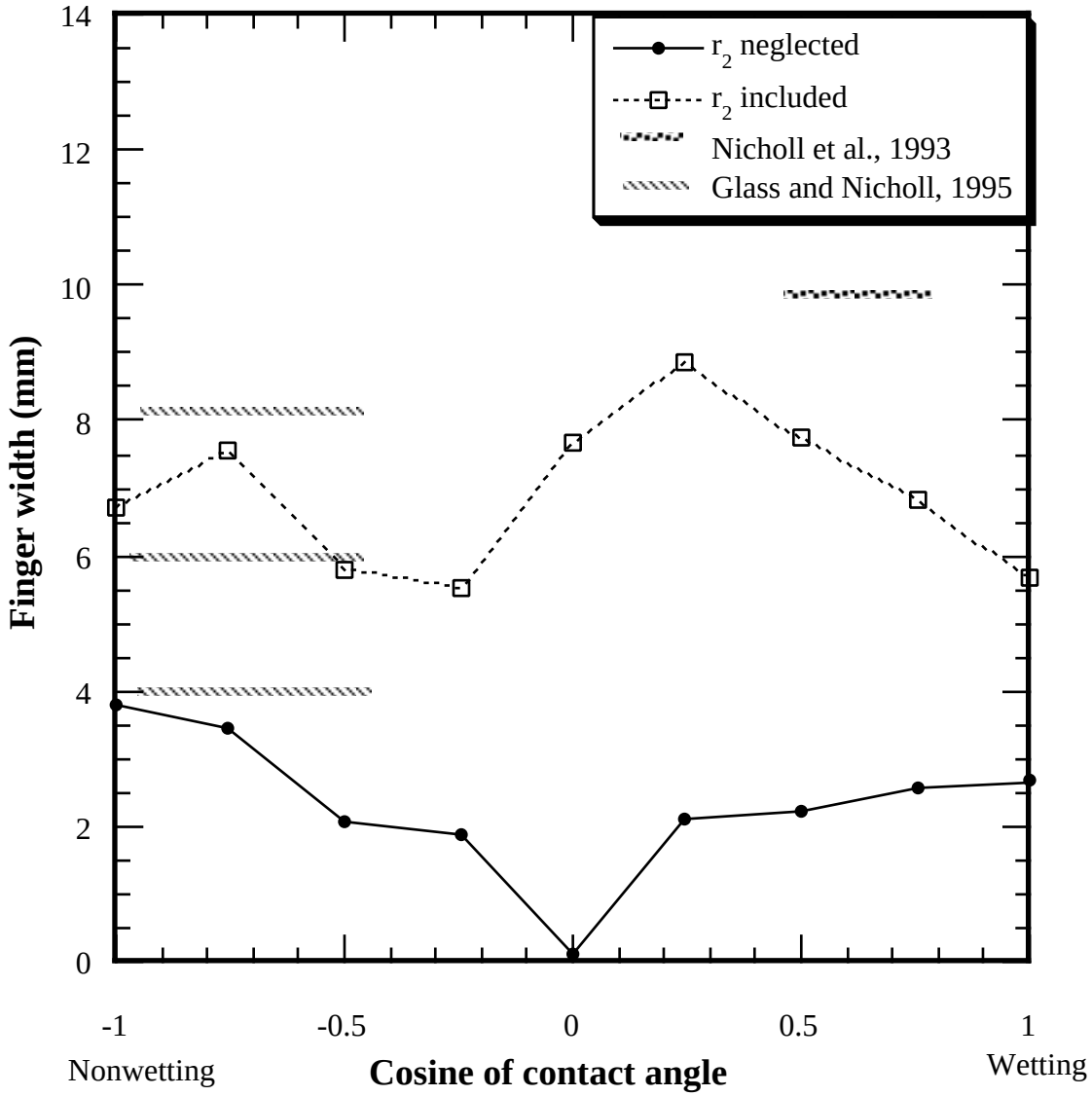

Figure 19: Finger widths for vertical fracture. Finger widths as measured normal to the direction of the gravitational gradient for all simulations are shown as a function of cos α. Nicholl et al. (1993a) measured gravity-driven fingers formed during the downward invasion of water into an air filled fracture formed from the same material as the aperture field used in these simulations. Fingers measured at the lowest flow rates considered in those experiments are slightly wider than the simulation results for wetting fluid where r_2 was included. Glass and Nicholl (1995b) reported fingers resulting from upward invasion of air into a water filled fracture that was also consistent with the aperture field used in these simulations. Three finger widths collected during that experiment are seen to span the simulation results for nonwetting invasion including in-plane curvature. Note that simulations in which r_2 was not included underestimate finger width at all contact angles.

19-finger_width

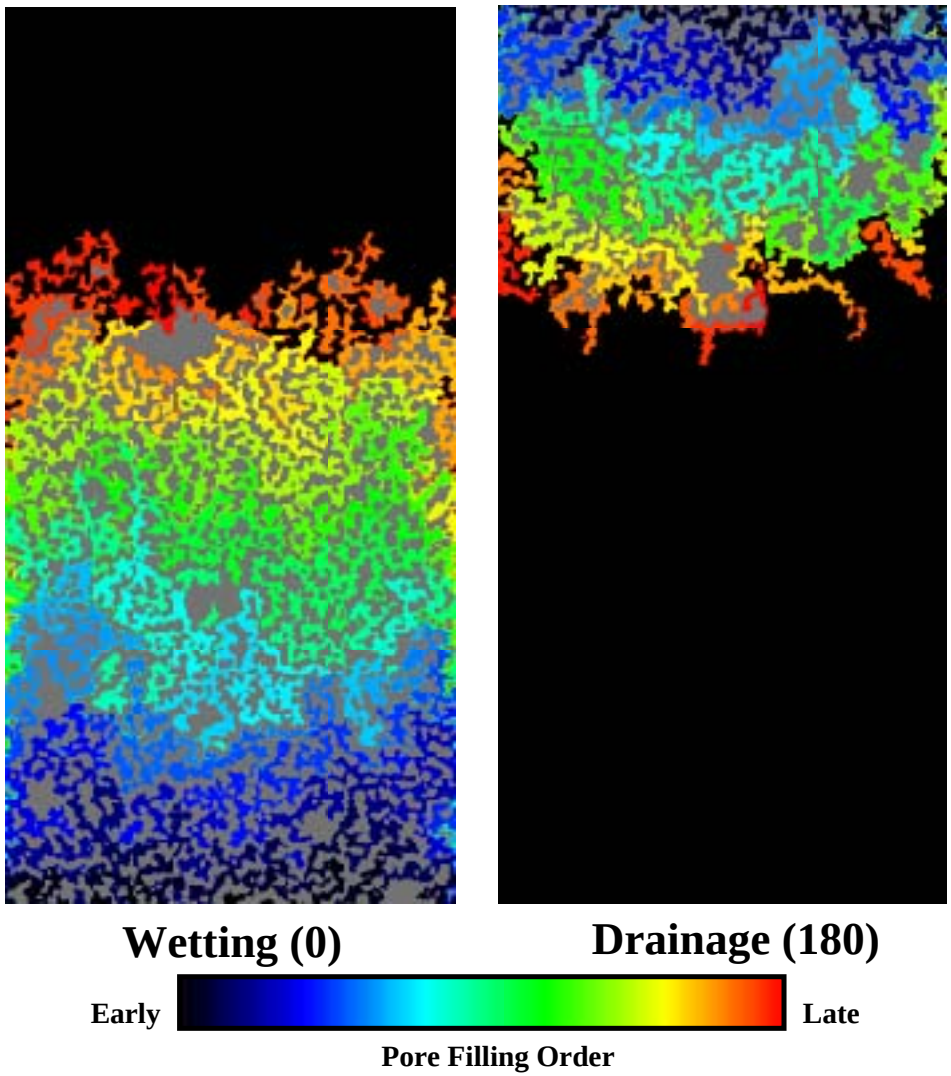

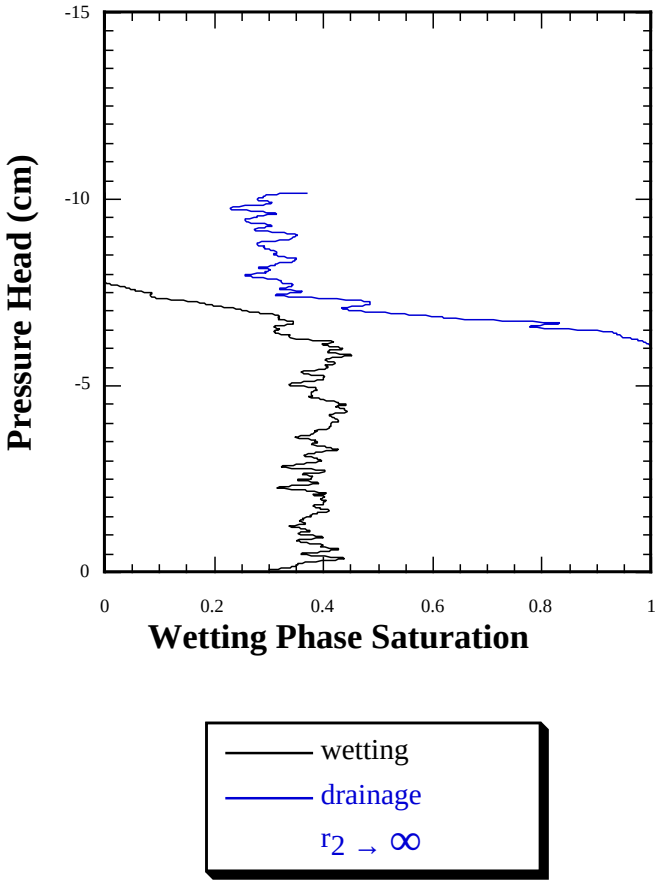

Figure 20: Gravity-stabilized vertical invasion neglecting in-plane curvature (r_2). Fully wetting (α = 0) and nonwetting cases (α = 180) are shown. The denser wetting fluid (water) is allowed to rise or drain downward until hydrostatic equilibrium is reached (fluid densities are set for air-water system). Large numbers of small entrapped regions are observed in both invasion fronts. As a result, invading phase saturations are relatively small; note that apparent lack of any significant hysteresis in the pressure-saturation relationships.

20-Rise_r2neg_0-180

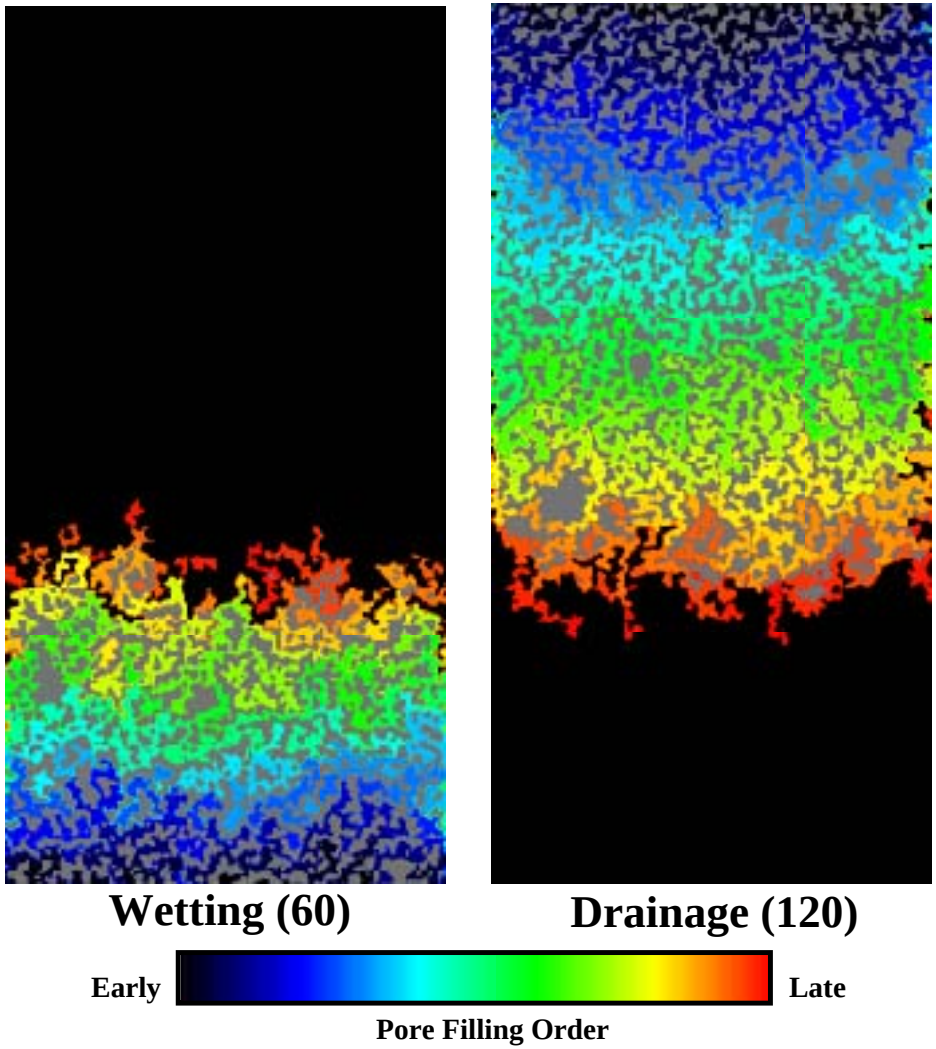

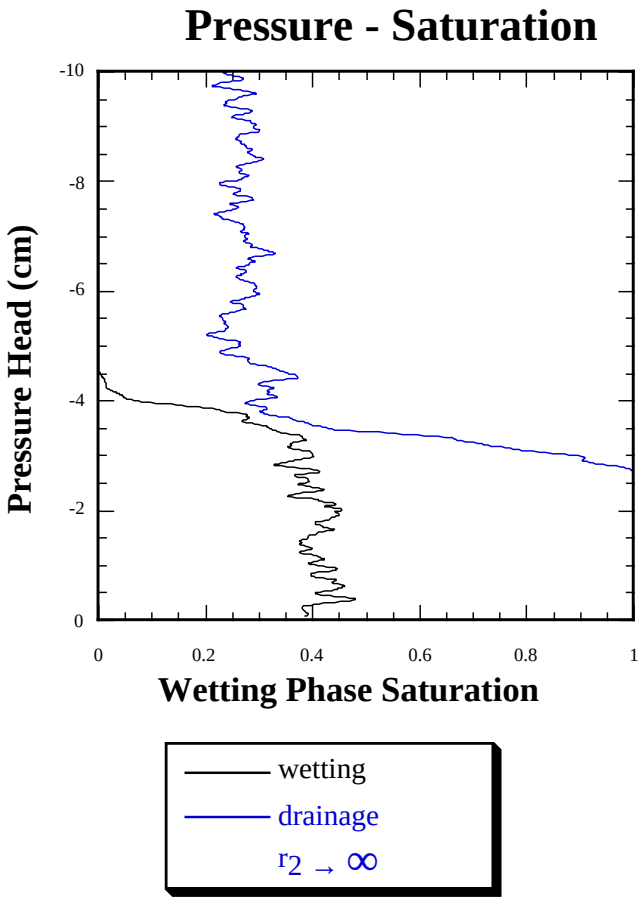

Figure 21: Gravity-stabilized vertical invasion neglecting in-plane curvature (r_2). Intermediate wetting (α = 60) and nonwetting cases (α = 120) are shown. Gross behavior differs only from the fully wetting/nonwetting cases (**figure 20**) in that the respective phase entry pressures are of lower magnitude.

21-Rise_r2neg_60-120

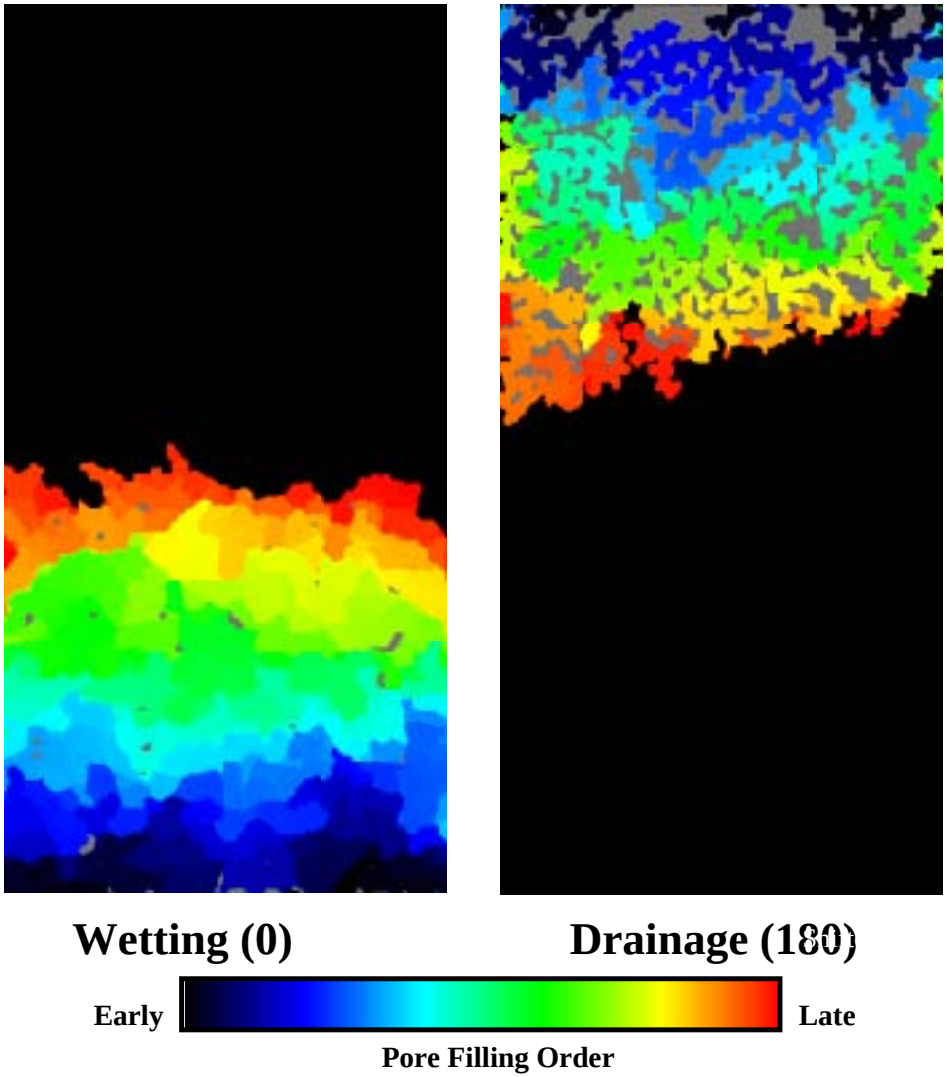

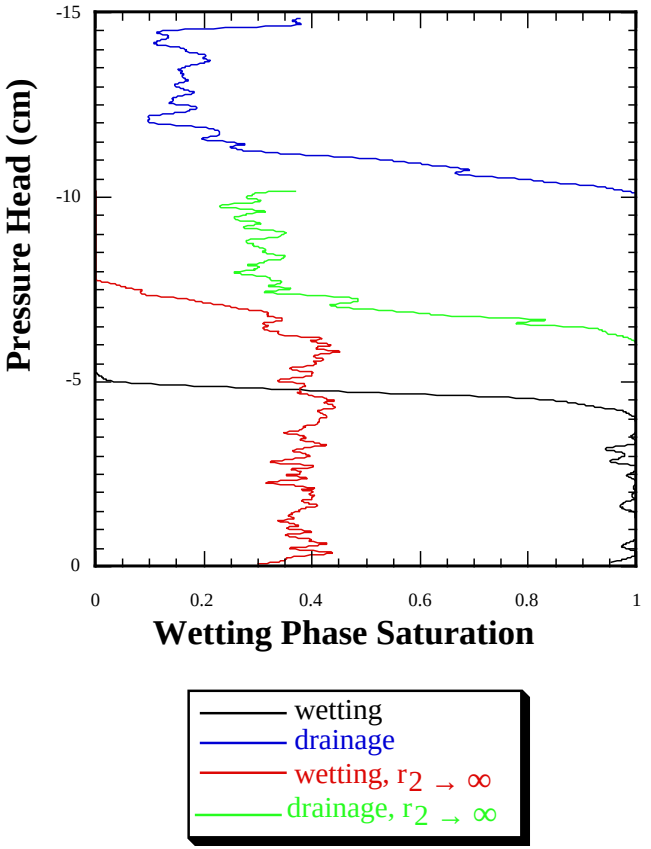

Figure 22: Gravity-stabilized vertical invasion including in-plane curvature (r_2). Fully wetting ($\alpha = 0$) and nonwetting cases ($\alpha = 180$) are shown. The wetting fluid is allowed to rise within the fracture and the nonwetting fluid is allowed to enter downward until hydrostatic equilibrium is reached (fluid densities are set for air-water system). Significant invasion of the nonwetting phase required the application of 5 cm pressure at the boundary; in effect, the aperture field had to be shifted up 5 cm in the gravity field, which is then taken into account during calculation of the drainage curve. Inclusion of r_2 results in a compact wetting phase invasion with small entrapment; entrapment during nonwetting invasion is reduced from the case where r_2 is neglected but still remains significant. Inclusion of r_2 leads to significant hysteresis in the pressure-saturation relationships independent of contact angle hysteresis.

22-Rise_r2incl_0-180

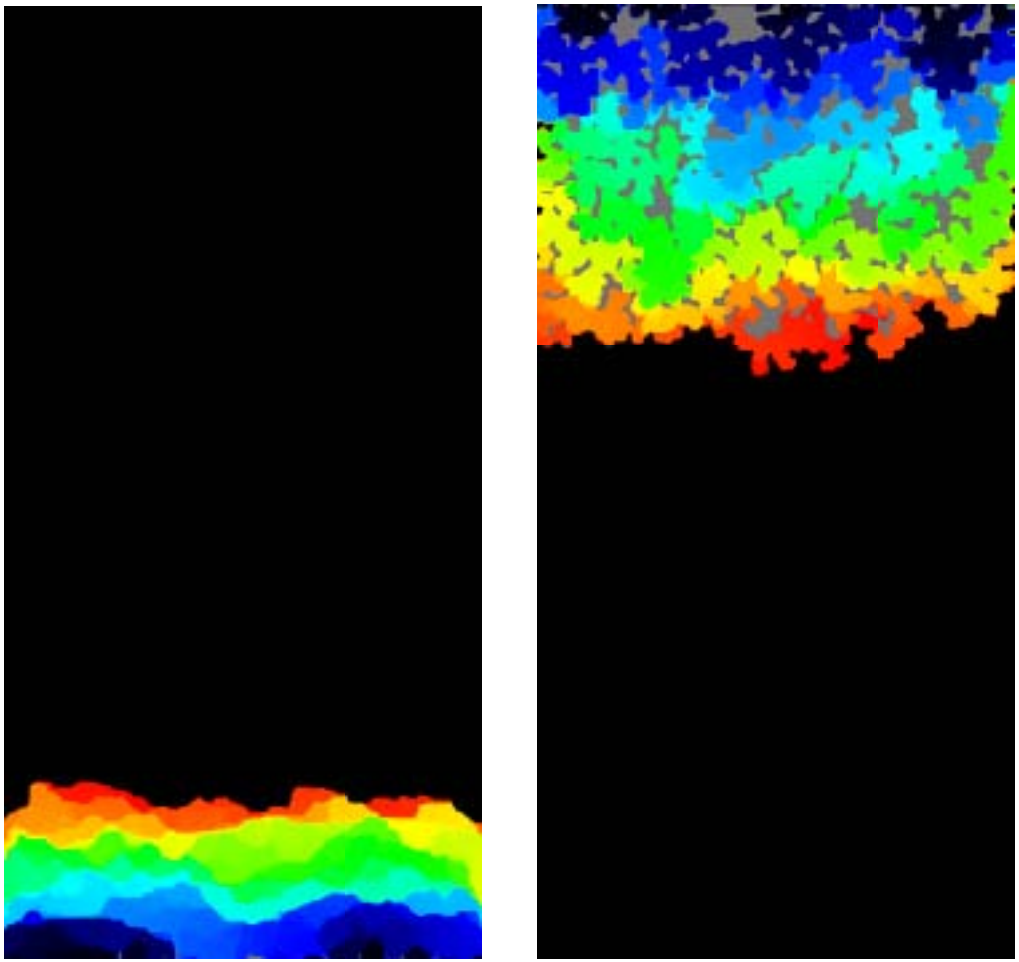

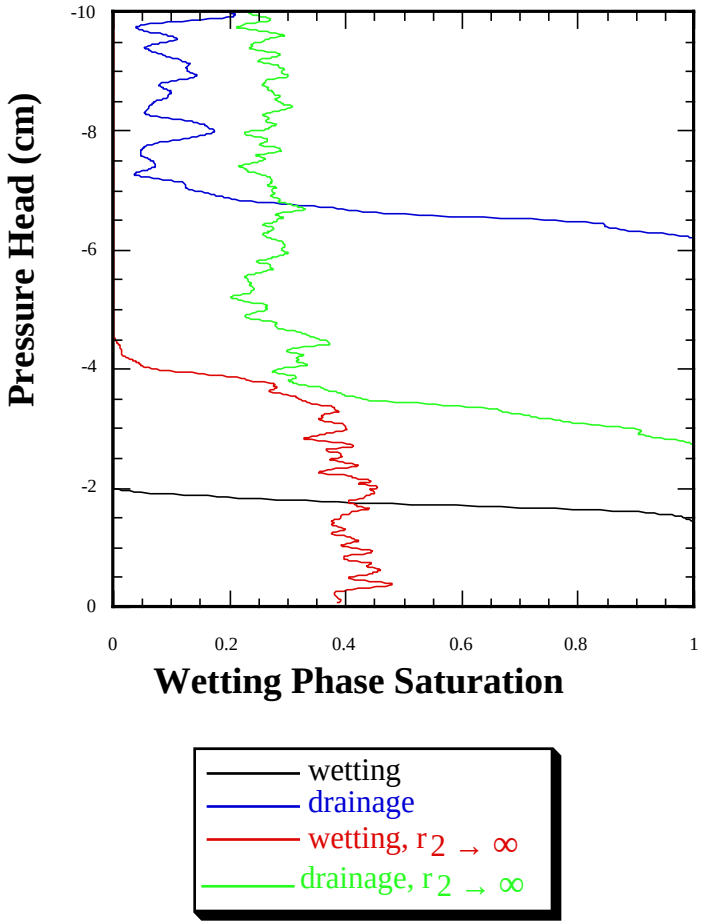

Figure 23: Gravity-stabilized vertical invasion including in-plane curvature (r_2). Intermediate wetting (α = 60) and nonwetting cases (α = 120) are shown. Gross behavior is very similar to that seen for the fully wetting/nonwetting case (**figure 22**); primary differences are reduced phase entry pressures and increased residual saturation.

23-Rise_r2incl_60-120

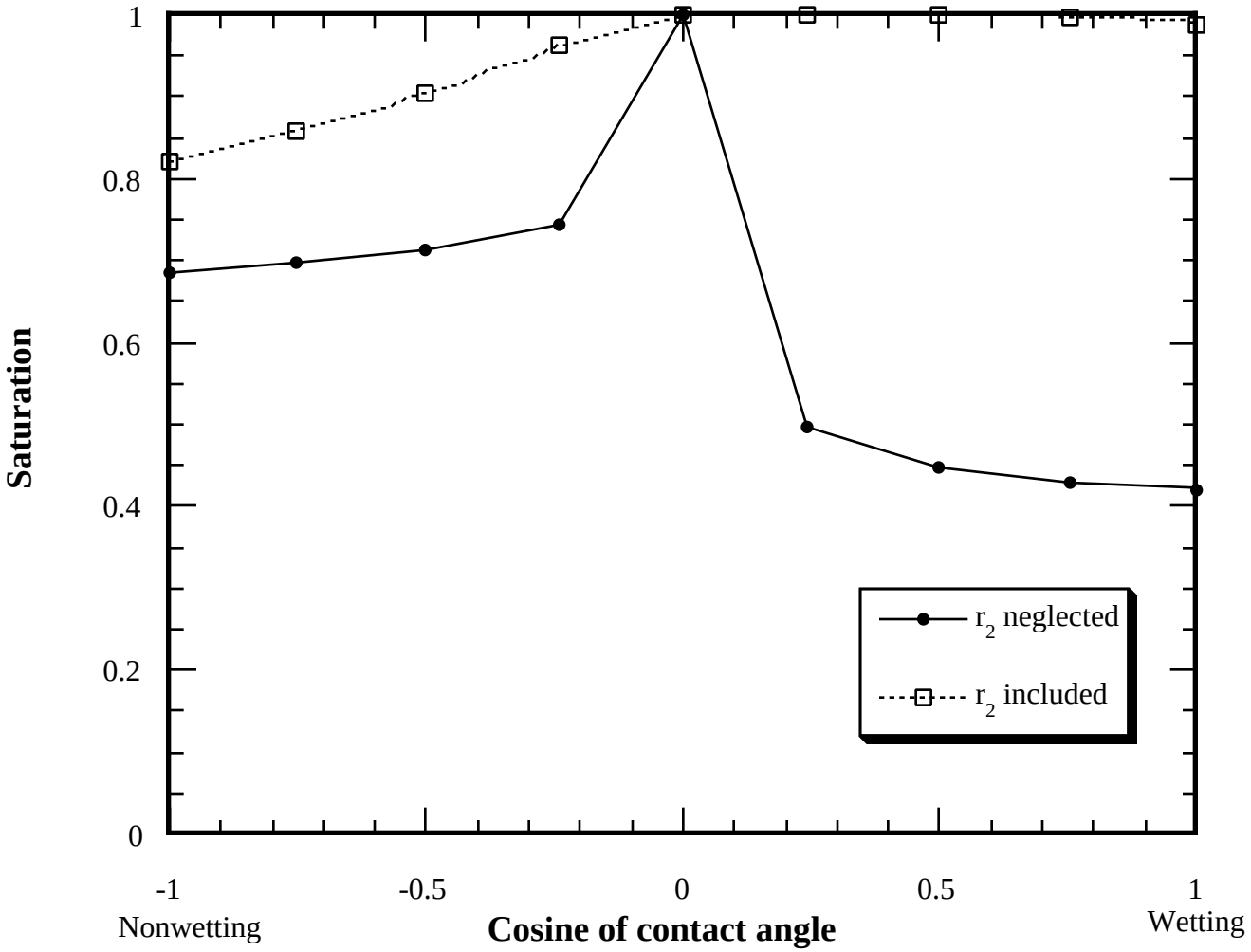

Figure 24: Phase saturation behind the front during gravity-stabilized vertical invasion as a function of contact angle. Except for α = 90 degrees, inclusion of r_2 leads to significantly increased phase saturation during gravity-stabilized invasion; this effect is particularly pronounced for wetting invasion.

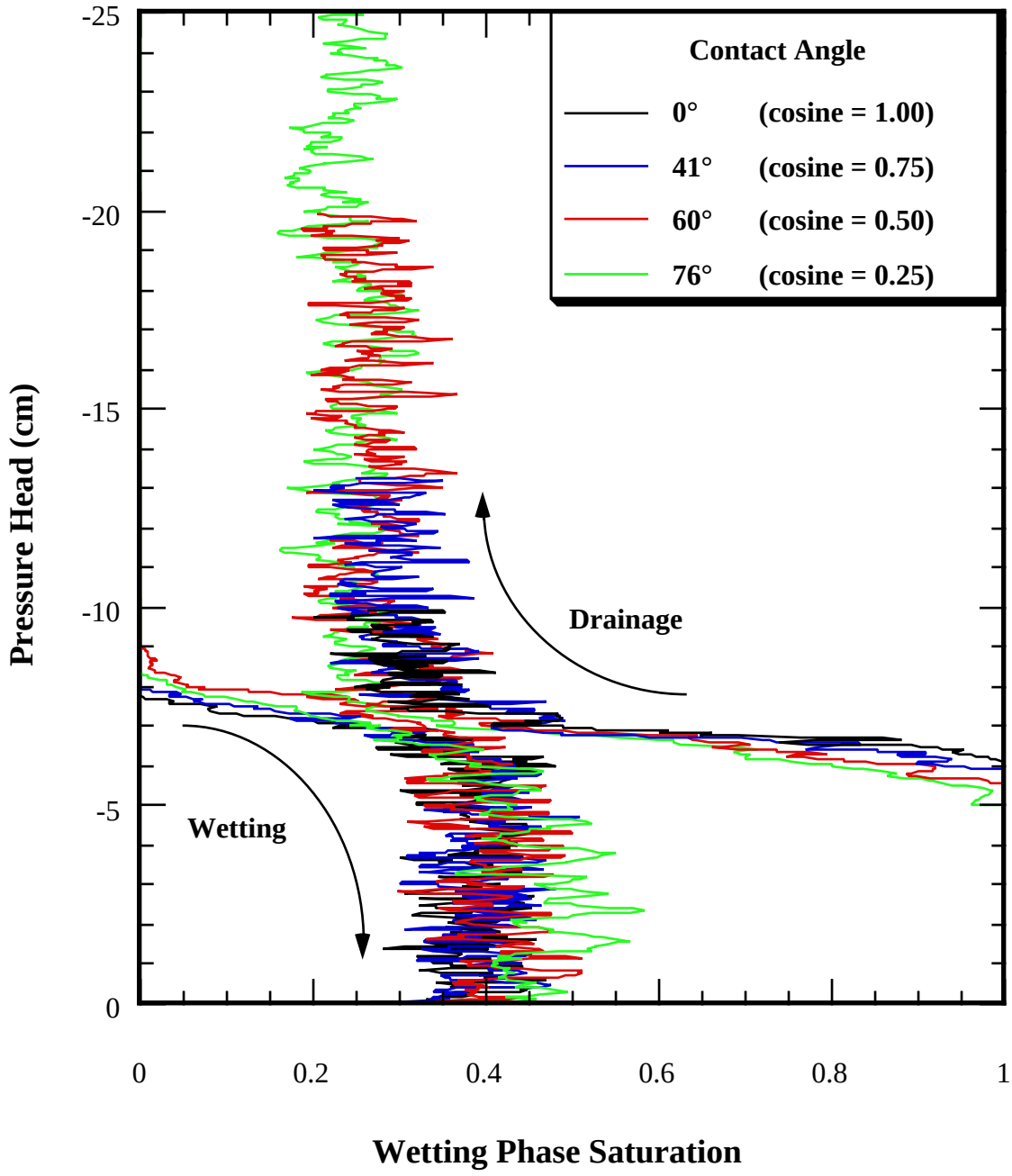

Figure 25: Contact angle scaling of pressure-saturation curves for cases neglecting in-plane curvature (r_2). Scaling the data by contact angle results in curves that very nearly fall on top of each other. Small differences spring from the influence of the gravity-capillary force ratio on residual saturation.

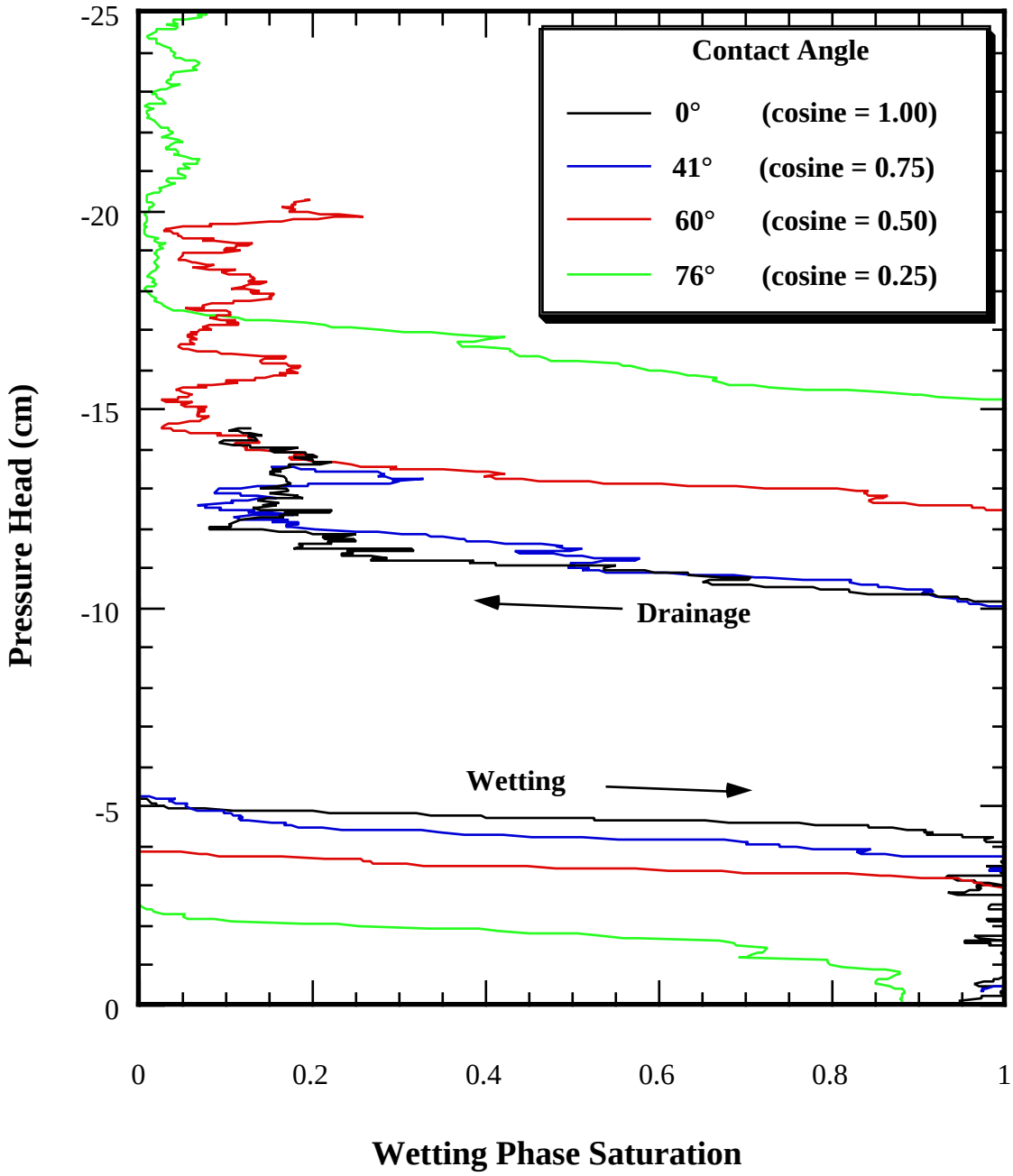

Figure 26: Contact angle scaling of pressure-saturation curves for cases including in-plane curvature (r_2). Contact angle scaling does not collapse pressure-saturation curves for the cases where r_2 has been included. Entry pressures for the wetting and nonwetting phases are significantly different for the various contact angles as are the residual saturations. The drainage curves show considerably more variation with contact angle than do the wetting curves.

26-psi-theta_ip_on

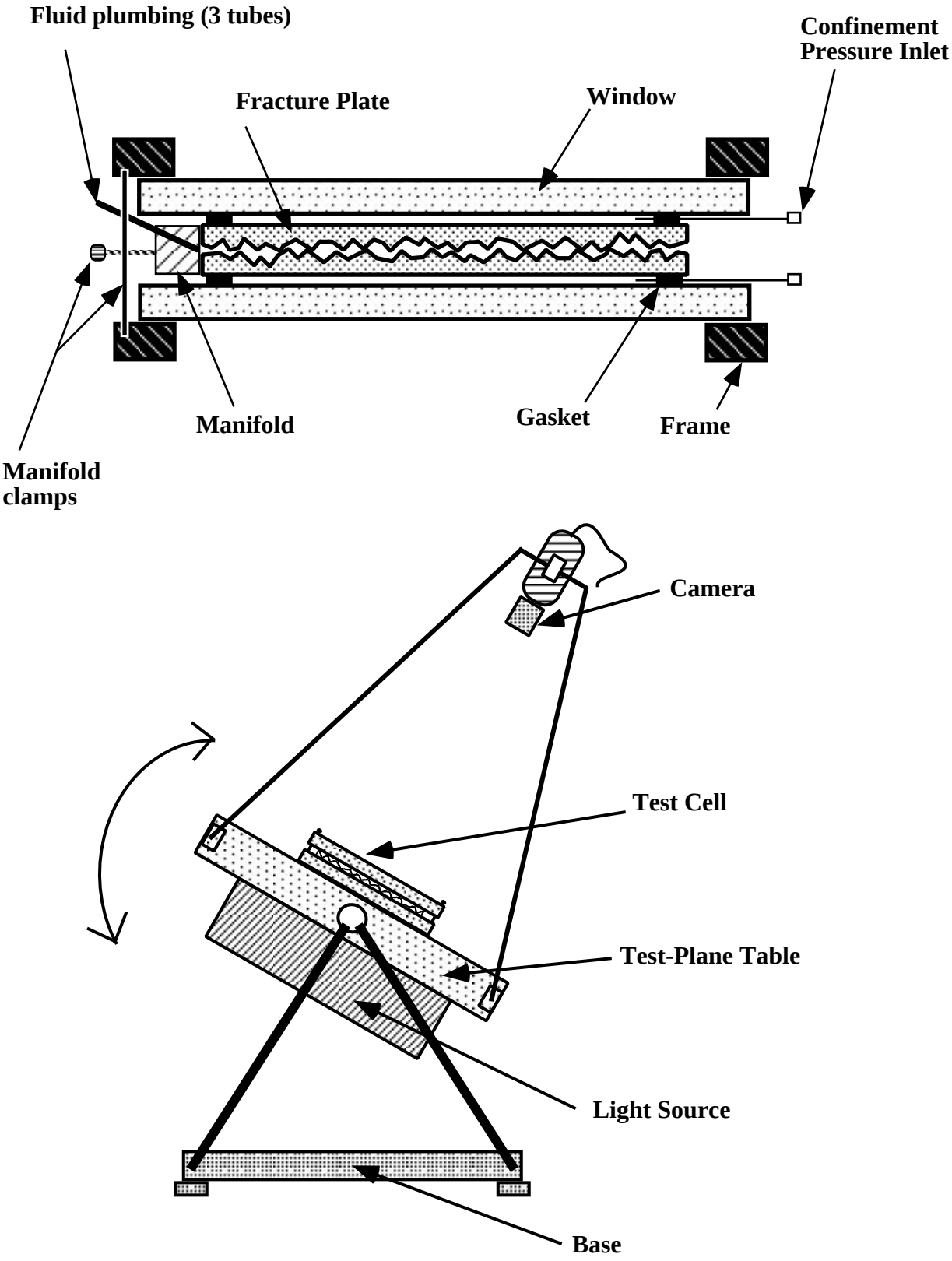

Figure 27: Fracture test cell and rotating test stand. The test cell consists of two rectangular aluminum frames with 1.9 cm thick plate glass windows. The thinner test fracture is sandwiched between the windows; gasket material is used to form a pressure container on each side of the fracture. Compressed gas is then used to apply a normal pressure to each side of the fracture plane. A rotating test stand holds the test cell, light source, and digital camera in rigid alignment; rotation of the test stand allows variation of fracture inclination and hence gravitational gradient. A feedback loop is used to stabilize output from the light source (high frequency fluorescent lamps).

27-test_cell_and_stand

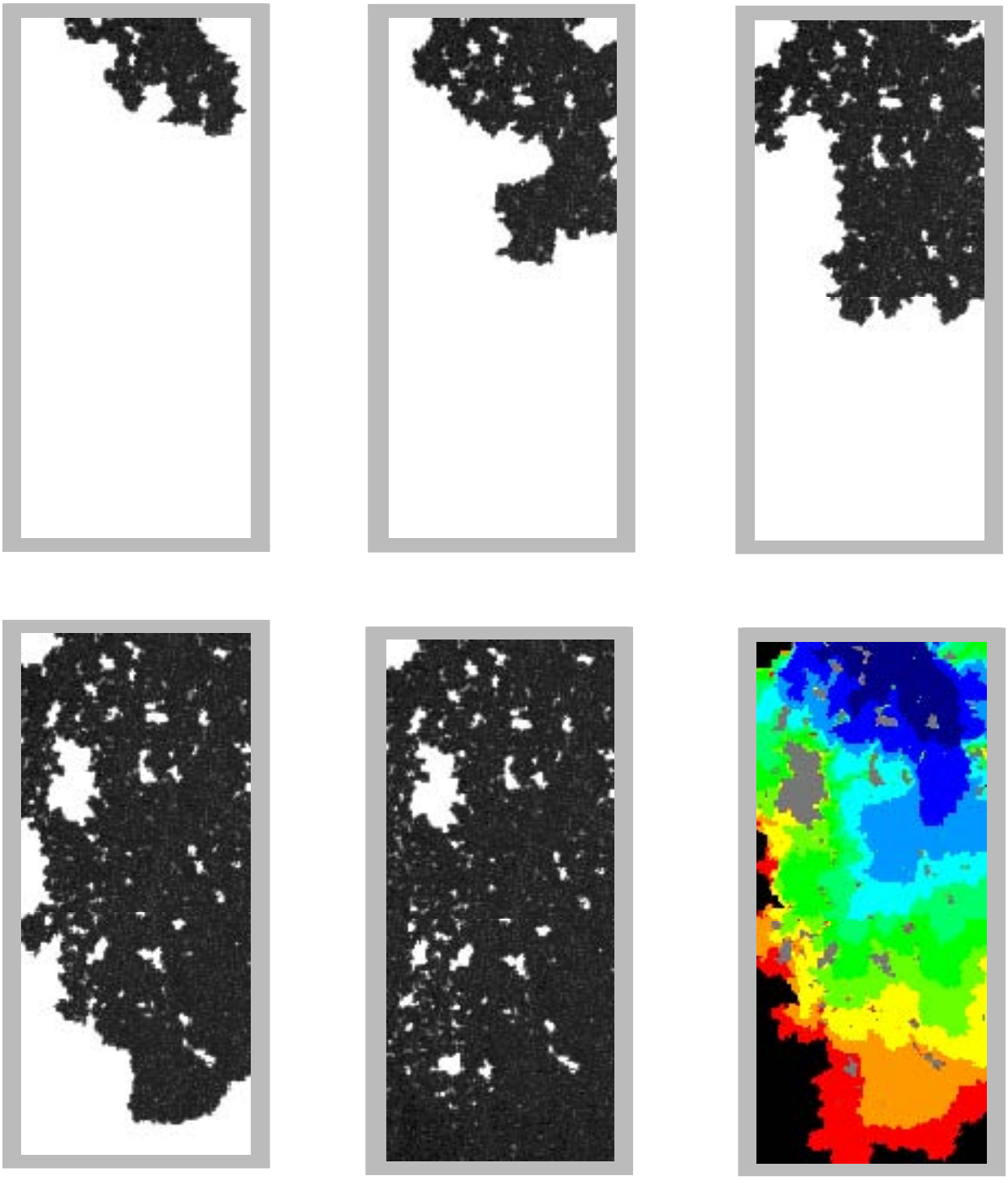

Figure 28: Experimental observations of horizontal wetting phase invasion. Dyed water is imbibed into the horizontal, air-filled analog fracture from a point source located at the middle of the top edge. All edges of the fracture were open allowing air to escape freely. An approximately 116 by 280 mm section of the 152 by 305 mm fracture is shown; the gasket which forms the confinement cell (see **figure 27**) obscures part of the image. Flow rate for this experiment (F91) was initially set at ~0.018 ml/minute; the first image shown reflects the first 60 minutes of imbibition at this flow rate. One hour after the initiation of flow, the flow rate was increased to 0.14 ml/minute; the next 4 images were collected at 70, 80, 100, and 120 minutes (satiated end point). In order to facilitate comparison between experiment and simulation, the final image is a composite of the experimental data that illustrates development of the phase invasion structure to near breakthrough. As in numerical simulations, the color scale shows the order of advancement from blue (first) to red (breakthrough); entrapped fluid is shown in gray and free defending fluid in black.

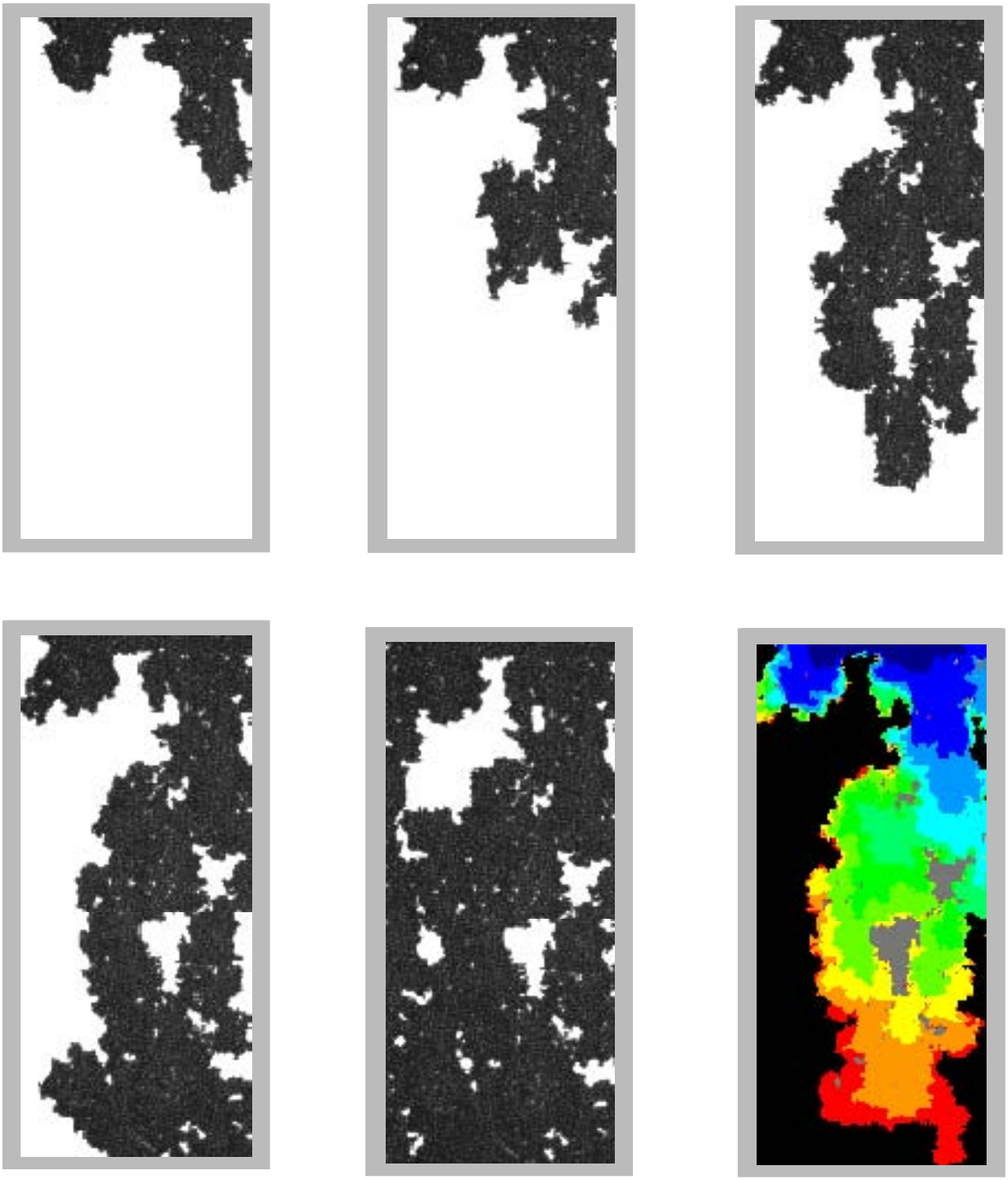

Figure 29: Experimental observations of horizontal wetting phase invasion. Dyed water is imbibed into the horizontal, air-filled analog fracture from a point source located at the middle of the top edge. All edges of the fracture were open allowing air to escape freely. An approximately 116 by 280 mm section of the 152 by 305 mm fracture is shown; the gasket which forms the confinement cell (see **figure 27**) obscures part of the image. Flow rate for this experiment (F104) was set at 0.14 ml/minute; the images shown were collected 10, 20, 30, 40, and 70 minutes (satiated end point). In order to facilitate comparison between experiment and simulation, the final image is a composite of the experimental data that illustrates development of the phase invasion structure to near breakthrough. As in numerical simulations, the color scale shows the order of advancement from blue (first) to red (breakthrough); entrapped fluid is shown in gray and free defending fluid in black.

29-horiz_h20_exp

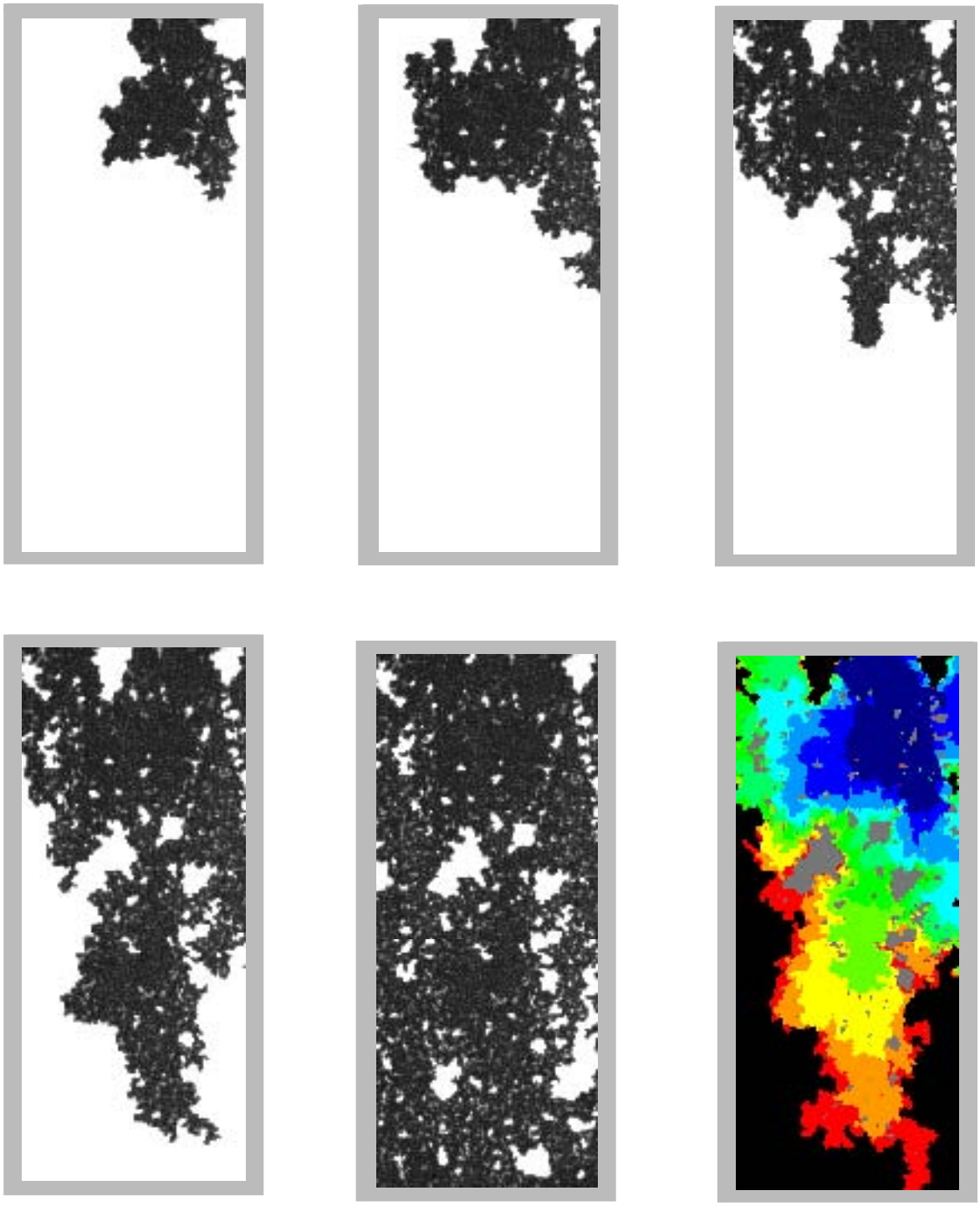

Figure 30: Experimental observations of horizontal wetting phase invasion. Dyed water is imbibed into the horizontal, air-filled analog fracture from a point source located at the middle of the top edge. All edges of the fracture were open allowing air to escape freely. An approximately 116 by 280 mm section of the 152 by 305 mm fracture is shown; the gasket which forms the confinement cell (see **figure 27**) obscures part of the image. Flow rate for this experiment (F109) was set at 0.024 ml/minute; the images shown were collected 50, 100, 150, 200, and 380 minutes (satiated end point). In order to facilitate comparison between experiment and simulation, the final image is a composite of the experimental data that illustrates development of the phase invasion structure to near breakthrough. As in numerical simulations, the color scale shows the order of advancement from blue (first) to red (breakthrough); entrapped fluid is shown in gray and free defending fluid in black.

30-horiz_h20_exp

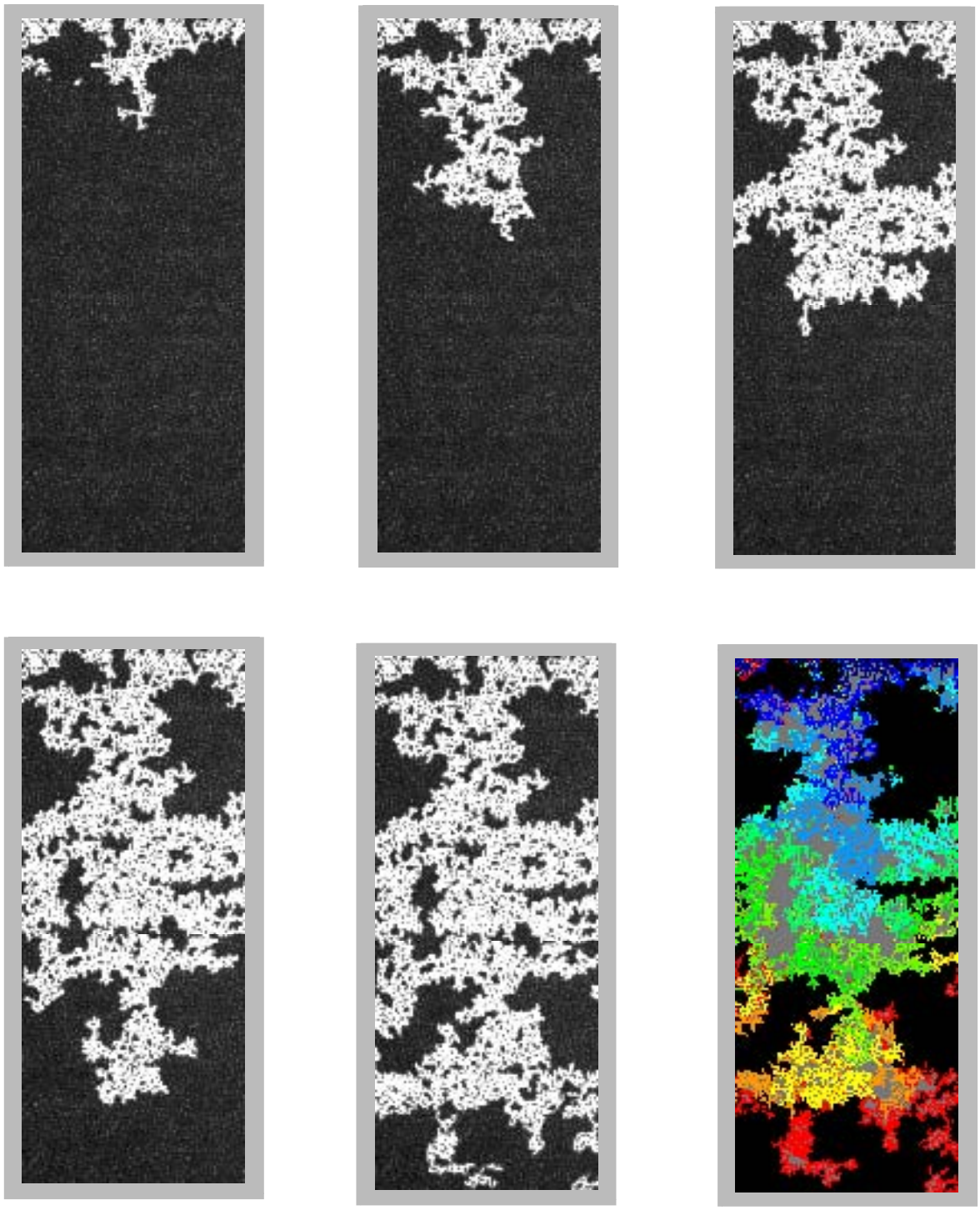

Figure 31: Experimental observation of horizontal nonwetting phase invasion. The analog fracture was sealed along the long edges and flow manifolds placed across the full width of the upstream and downstream boundaries. After fully saturating the fracture with dyed water, air was supplied slowly to the upstream boundary using a positive displacement pump, and the downstream boundary vented to atmospheric pressure. An approximately 116 by 280 mm section of the 152 by 305 mm fracture is shown; the gasket which forms the confinement cell (see **figure 27**) obscures part of the image. In order to facilitate comparison between experiment and simulation, the final image is a composite of the experimental data that illustrates development of the phase invasion structure to near breakthrough. As in numerical simulations, the color scale shows the order of advancement from blue (first) to red (breakthrough); entrapped fluid is shown in gray and free defending fluid in black.

31-horiz_air_exp

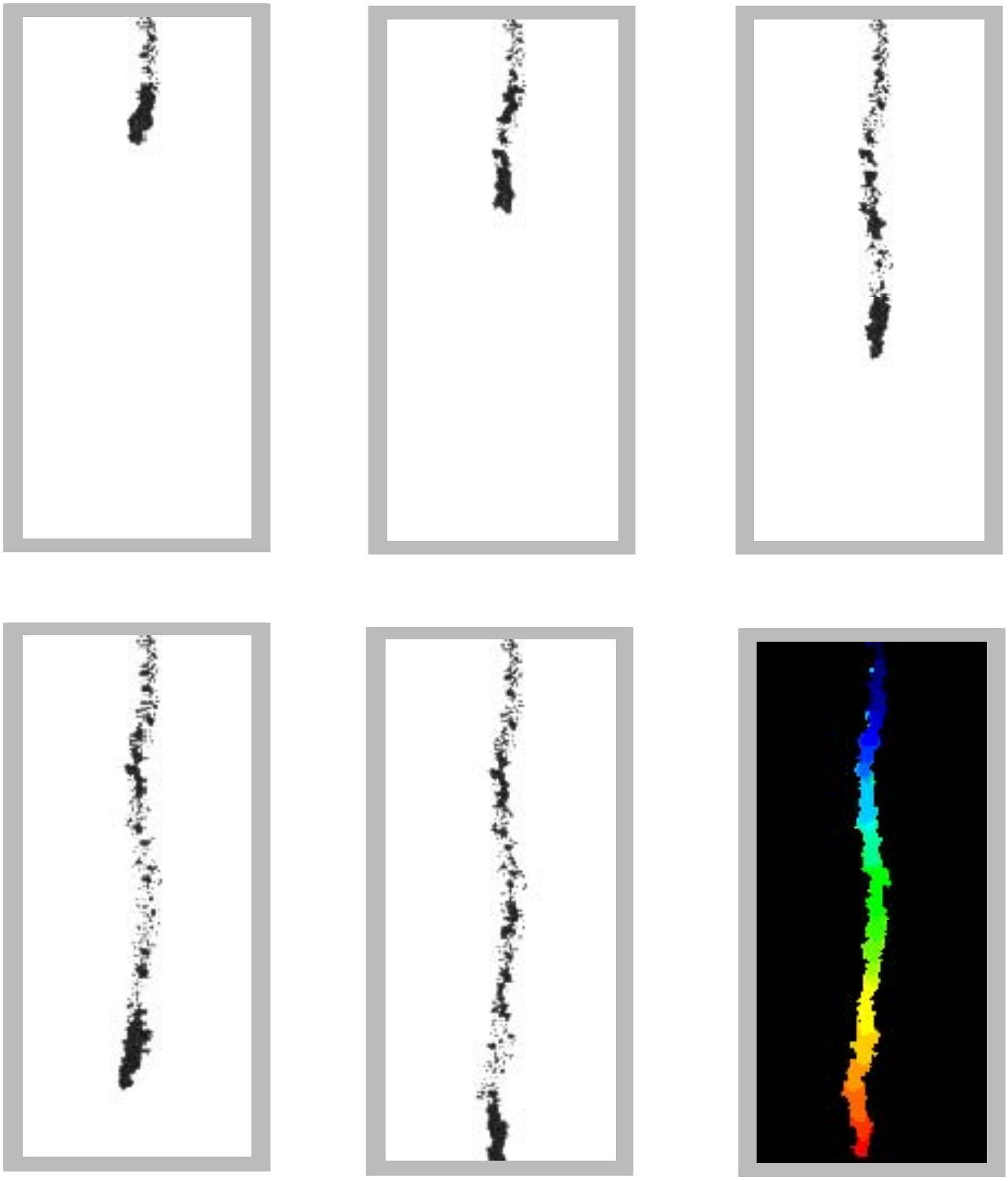

Figure 32: Experimental observations of gravity destabilized wetting invasion. The air-filled analog fracture was inclined to vertical and slow steady flow of dyed water initiated from a point source arbitrarily located on the upper boundary. An approximately 116 by 280 mm section of the 152 by 305 mm fracture is shown; the gasket which forms the confinement cell (see **figure 27**) obscures part of the image. A single gravity-driven finger forms as a hanging column that is initially pinned to the upper boundary by capillary forces. When the column reaches a length sufficient to overcome the fracture air-entry invasion pressure, air invades apertures along the top of the fracture behind the water finger tip. The finger tip now disconnects and moves downward as a coherent unit leaving entrapped water in its wake. Subsequent reinvasion of air filled apertures between these disconnected blobs replenishes flow between finger-tip and source. Flow rate for this trial (F41) was set at 0.025 ml/minute; images shown were taken 150, 300, 375, 450, and 525 seconds after initiation of flow (from the experiments of Nicholl et al., 1993a). The simulation differs from the experiment in that drainage and re-invasion behind the finger-tip is not modeled. In order to facilitate comparison between experiment and simulation, the final image shows the area swept by the experimental finger at breakthrough. The color scale shows the order of advancement from blue (first) to red (breakthrough); entrapped fluid is shown in gray and free defending fluid in black.

32-vert_h20_exp

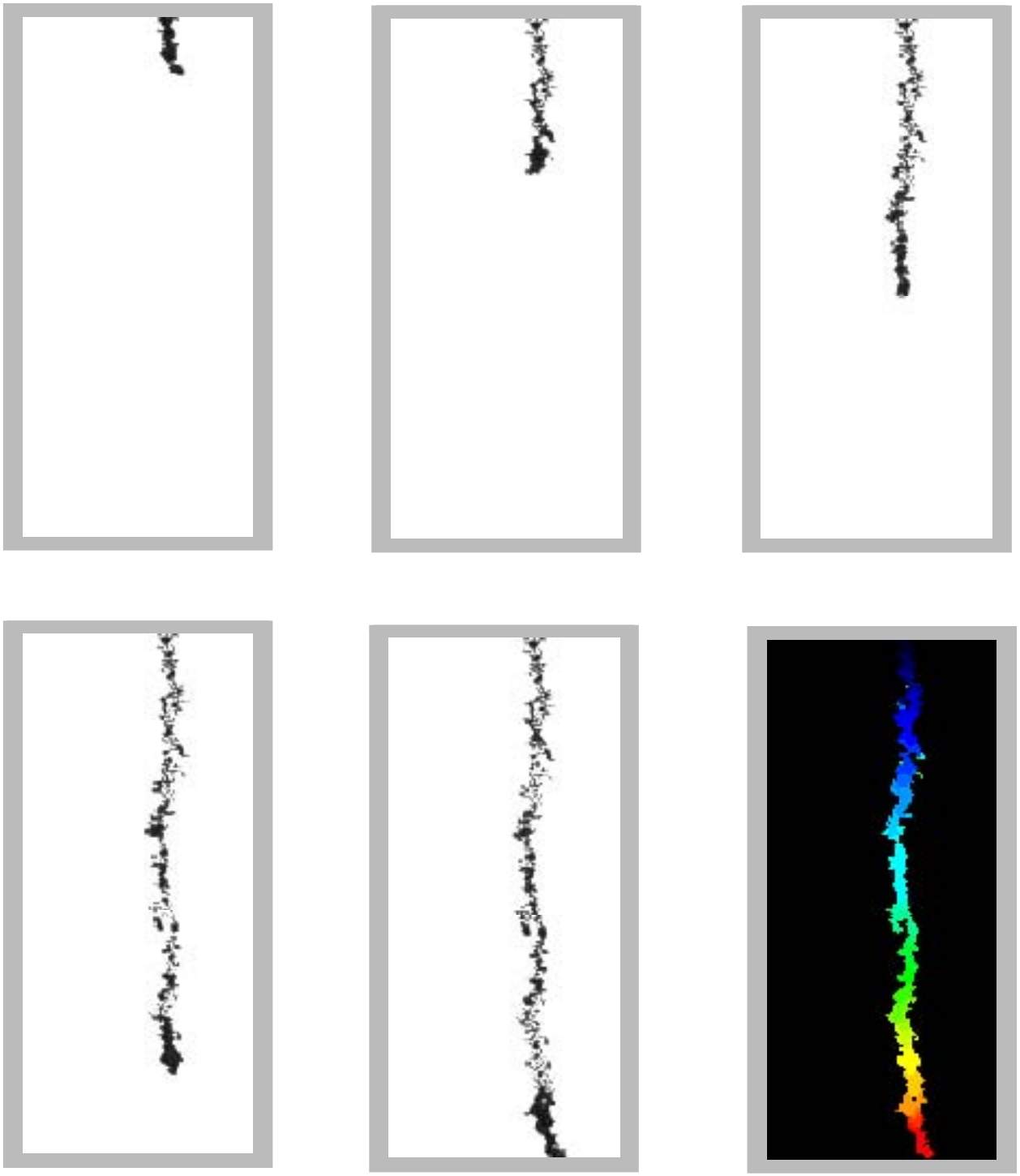

Figure 33: Experimental observations of gravity destabilized wetting invasion. The air-filled analog fracture was inclined to vertical and slow steady flow of dyed water initiated from a point source arbitrarily located on the upper boundary. An approximately 116 by 280 mm section of the 152 by 305 mm fracture is shown; the gasket which forms the confinement cell (see **figure 27**) obscures part of the image. A single gravity-driven finger forms as a hanging column that is initially pinned to the upper boundary by capillary forces. When the column reaches a length sufficient to overcome the fracture air-entry invasion pressure, air invades apertures along the top of the fracture behind the water finger tip. The finger tip now disconnects and moves downward as a coherent unit leaving entrapped water in its wake. Subsequent reinvasion of air filled apertures between these disconnected blobs replenishes flow between finger-tip and source. Flow rate for this trial (F54) was set at 0.026 ml/minute; images shown were taken 75, 150, 225, 375, and 450 seconds after initiation of flow (from the experiments of Nicholl et al., 1993a). The simulation differs from the experiment in that drainage and re-invasion behind the finger-tip is not modeled. In order to facilitate comparison between experiment and simulation, the final image shows the area swept by the experimental finger at breakthrough. The color scale shows the order of advancement from blue (first) to red (breakthrough); entrapped fluid is shown in gray and free defending fluid in black.

33-vert_h20_exp

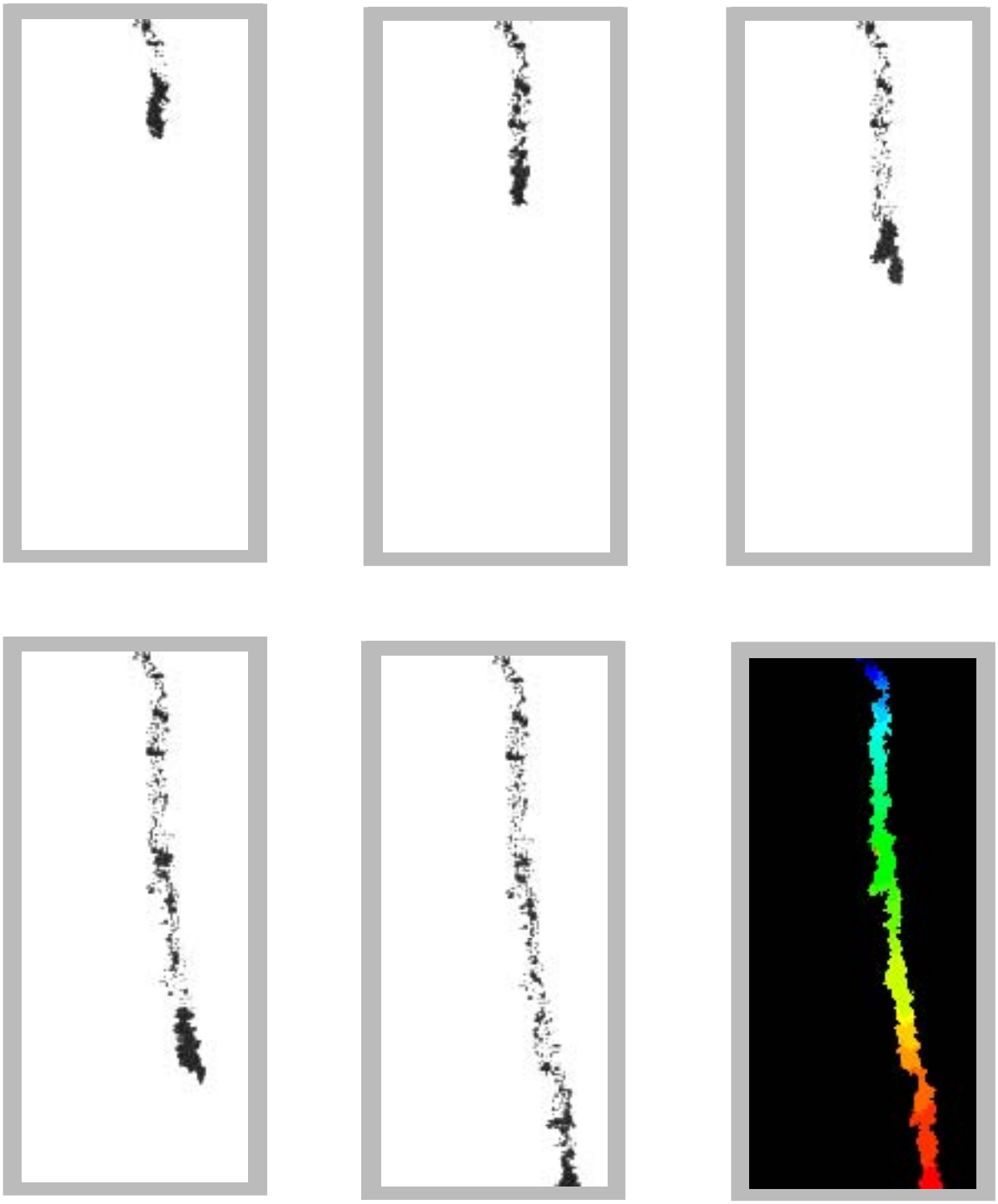

Figure 34: Experimental observations of gravity destabilized wetting invasion. The air-filled analog fracture was inclined to vertical and slow steady flow of dyed water initiated from a point source arbitrarily located on the upper boundary. An approximately 116 by 280 mm section of the 152 by 305 mm fracture is shown; the gasket which forms the confinement cell (see **figure 27**) obscures part of the image. A single gravity-driven finger forms as a hanging column that is initially pinned to the upper boundary by capillary forces. When the column reaches a length sufficient to overcome the fracture air-entry invasion pressure, air invades apertures along the top of the fracture behind the water finger tip. The finger tip now disconnects and moves downward as a coherent unit leaving entrapped water in its wake. Subsequent reinvasion of air filled apertures between these disconnected blobs replenishes flow between finger-tip and source. Flow rate for this trial (F80) was set at 0.026 ml/minute; images shown were taken 300, 375, 450, 600, and 750 seconds after initiation of flow (from the experiments of Nicholl et al., 1993a,b). The simulation differs from the experiment in that drainage and re-invasion behind the finger-tip is not modeled. In order to facilitate comparison between experiment and simulation, the final image shows the area swept by the experimental finger at breakthrough. The color scale shows the order of advancement from blue (first) to red (breakthrough); entrapped fluid is shown in gray and free defending fluid in black.

34-vert_h20_exp

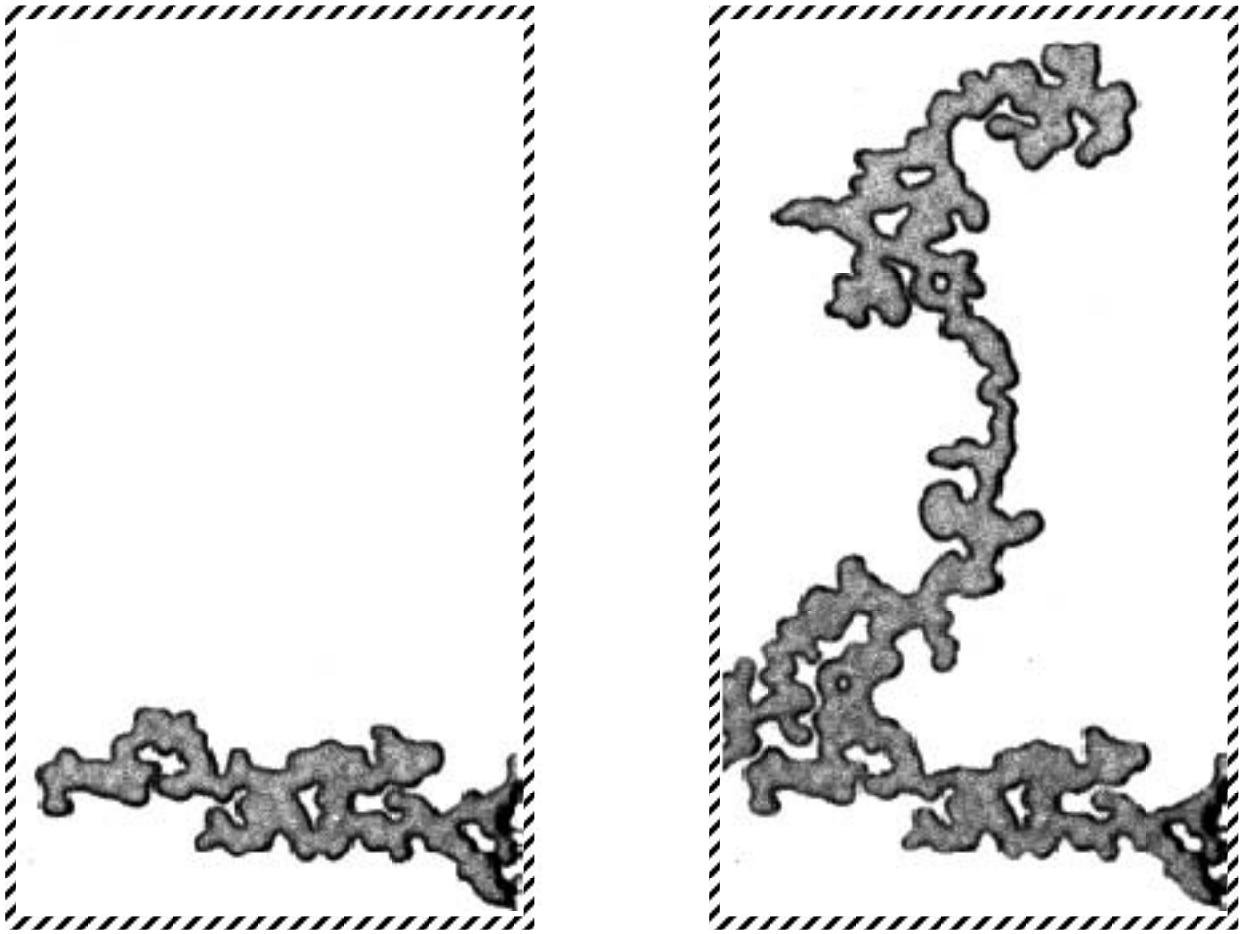

a) b)

Figure 35: A single finger resulting from gravity destabilized nonwetting invasion. Air was drawn along the bottom boundary of an otherwise sealed, vertically inclined, water saturated, analog fracture (152 by 305 mm). As water evaporated it was replaced by the air phase; however, while evaporation occurs along the entire exposed boundary, replacement will occur at the aperture with the lowest invasion potential. The images shown here are enlargements of a single finger (an approximately 25 by 50 mm region is shown); the left-hand image shows air invading from the left and moving nearly horizontal, but always trending upward. The right-hand image shows distinct vertical development of the finger and entrapment of the defending phase (from the experiments of Glass and Nicholl, 1995b).

Figure 36: Experimental observations of gravity destabilized nonwetting phase invasion. Air was allowed to pass along the bottom boundary of an otherwise sealed, vertically inclined analog fracture; an approximately 130 by 250 mm section of the 152 by 305 mm fracture is shown here. As water evaporated it was replaced by the air phase. Although evaporation occurs along the entire exposed boundary, replacement will occur at the aperture with the lowest invasion potential leading to the formation of upward growing buoyant fingers. Re-invasion by the wetting phase complicates development of the phase structure. This image shows the area swept by all fingers (black) that formed during this experiment; the region corresponding to **figure 35** is delineated by a box in the lower right-hand corner (from the experiments of Glass and Nicholl, 1995b).

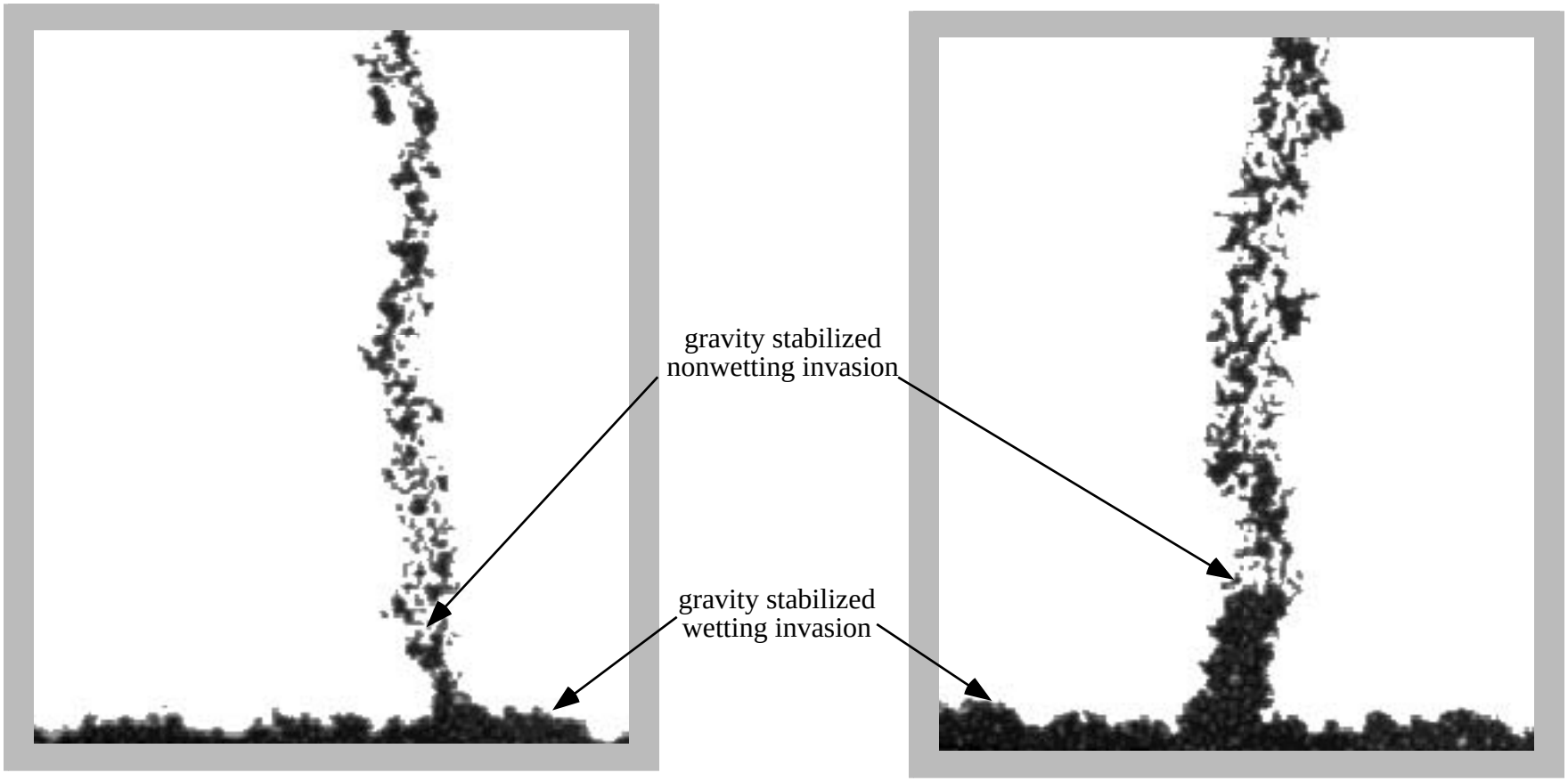

Figure 37: Experimental observations of gravity stabilized wetting invasion. In the gravity-driven fingering experiments of Nicholl et al., (1993a) water moved downward through the vertical analog fracture until reaching the lower boundary. This open edge acted as a zero pressure boundary. Fluid contacting the boundary migrated laterally away from the finger into the air-filled region at the bottom of the fracture, where it rose to a height dictated by the balance of capillary and gravity forces. The images shown here represent an approximately 130 by 140 mm section at the bottom of the 152 by 305 mm fracture; the gasket forming the confinement cell obscures part of the capillary rise. Note the compact, mostly saturated structure that forms during gravity stabilized wetting invasion. The average rise for all experiments was 22.5 mm; shown here are: a) experiment F54, capillary rise = 18 mm; and b) experiment F57, capillary rise = 20 mm. After the cessation of flow, air re-invades the finger; this gravity stabilized nonwetting invasion (see also **figure 38**) proceeds until the interface reaches hydrostatic equilibrium (air-entry pressure). 37-low_rise

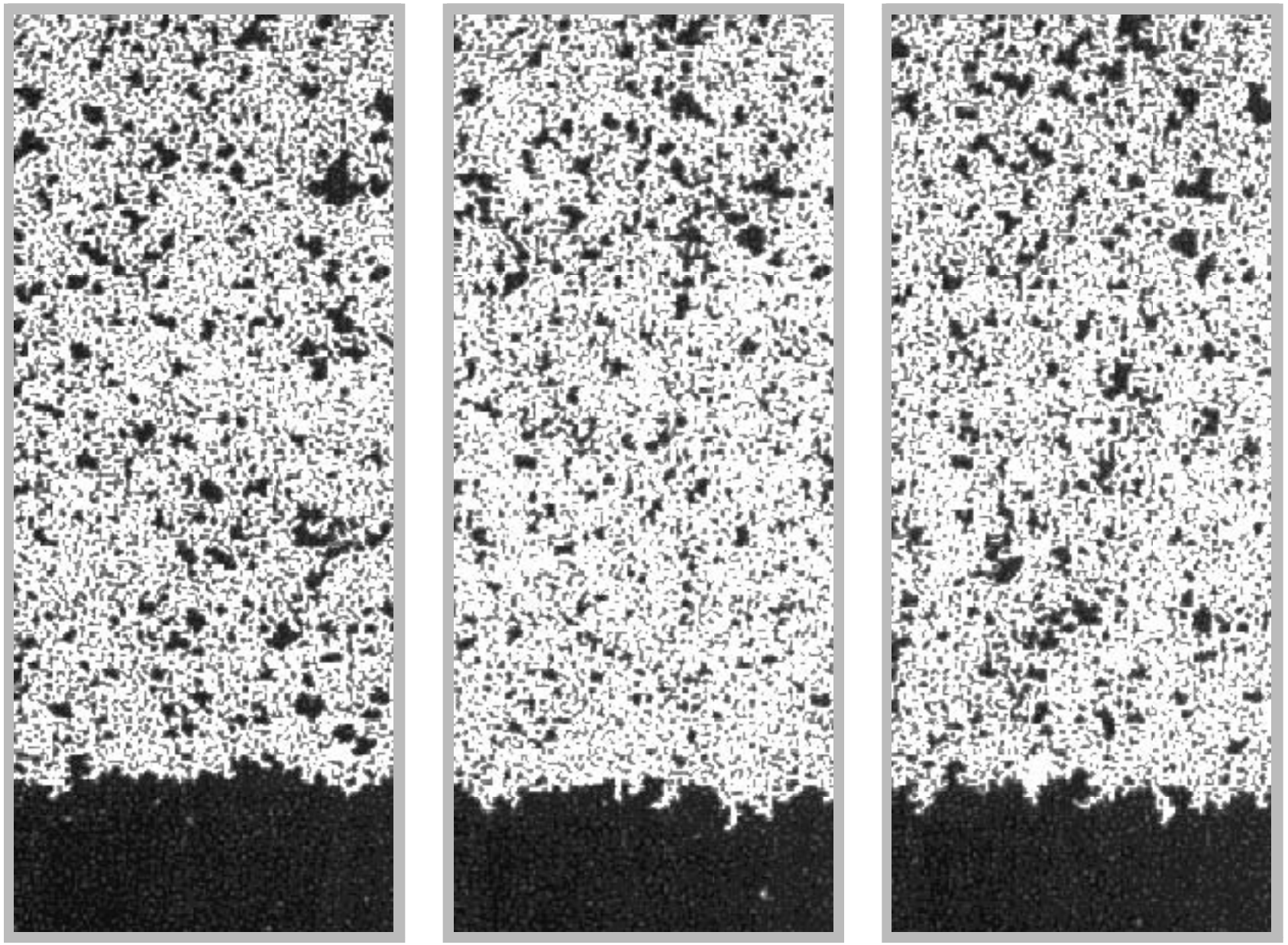

Figure 38: Experimental observations of gravity stabilized nonwetting invasion. The analog fracture was saturated with dyed water and then inclined to vertical, with all boundaries open to atmospheric pressure. Free drainage proceeded until the interface reached hydrostatic equilibrium An approximately 116 by 280 mm section of the 152 by 305 mm fracture is shown at equilibrium for three repetitions; the gasket which forms the confinement cell (see **figure 27**) obscures part of the image.

38-high_rise

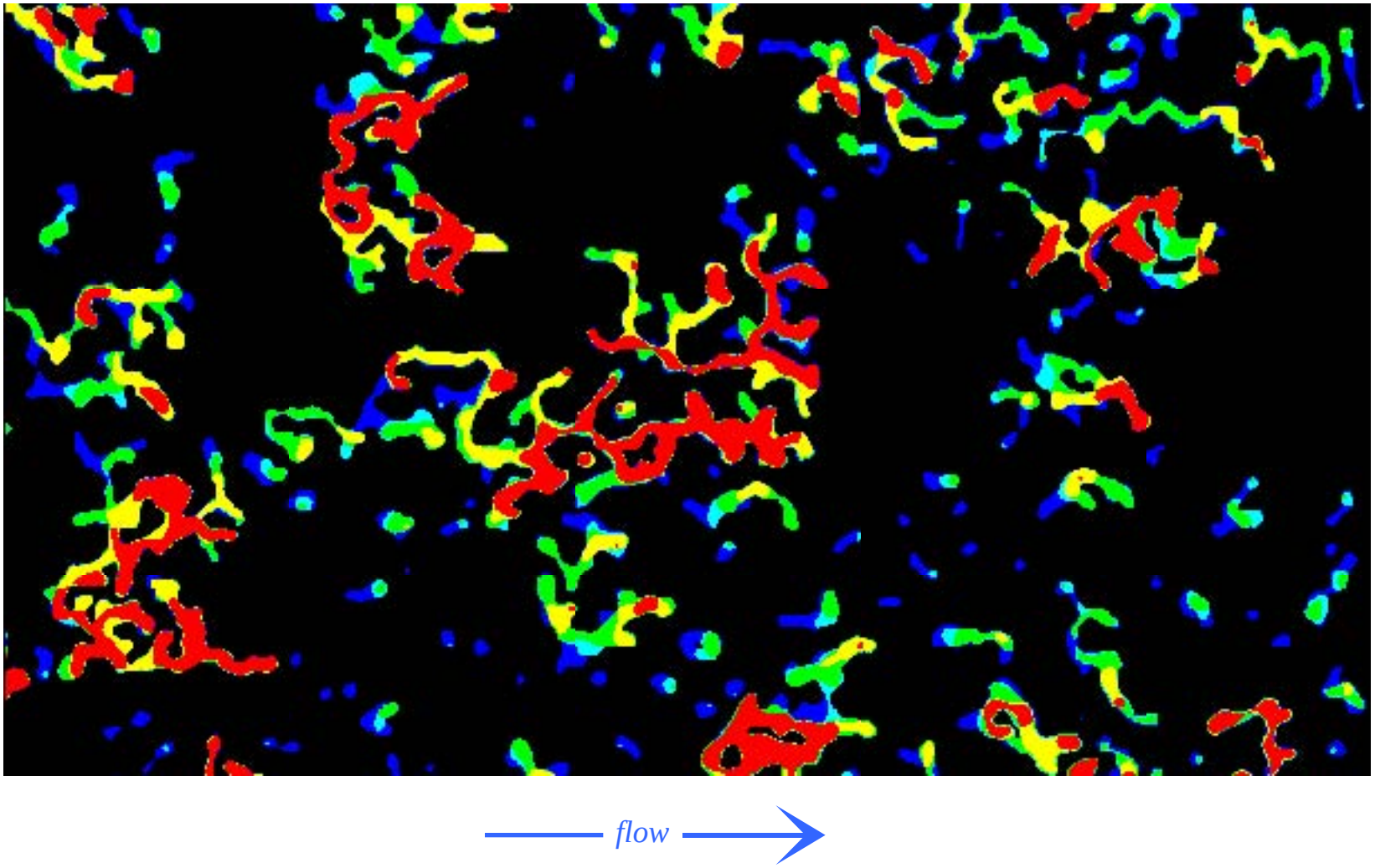

Figure 39: Experimental observations of nonwetting phase dissolution in a flowing fracture. The process of entrapped phase (air) dissolution into the flowing phase (deaerated water) is visualized in the horizontal analog fracture. This image depicts the order of dissolution (replacement of air with water) over a 231 minute time span for a 58 x 102 mm region of the 152 x 305 mm fracture; water flow is from right to left, at a rate that is sufficiently high to minimize the formation of a dissolution front but sufficiently low as to not mobilize entrapped air clusters. Apertures where no change in phase occur are displayed as black (water) and red (air). Apertures where water invades the air as the air dissolves at intermediate times during the experiment are shown as violet (t = 0 - 25 minutes), blue (t = 25 - 73 minutes), green (t = 73 - 141 minutes), and yellow (t = 141 - 231 minutes). Notice that small entrapped phase regions dissolve quickly through simple compact shrinkage, while larger entrapped regions exhibit interfacial recession along cluster appendages with occasional cluster splitting. After becoming sufficiently small, these clusters then dissolve by uniform shrinkage (from the experiments of Glass and Nicholl, 1995a).

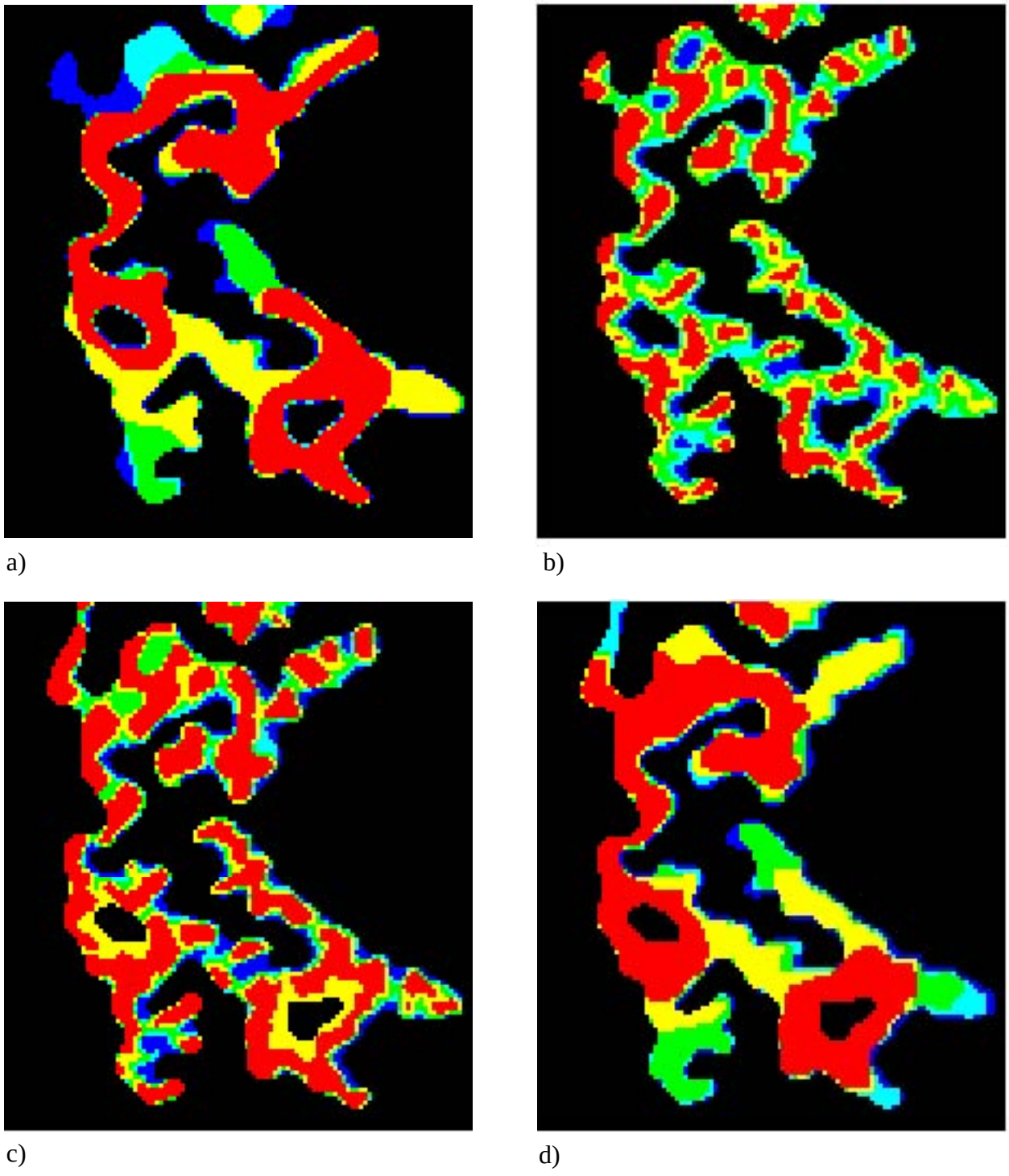

Figure 40: Nonwetting phase dissolution, single cluster comparison of simulation and experiments. Observations wetting phase invasion for a single complex cluster from **figure 39** are shown in (a) and are compared to SP (b), IP (c) and MIP (d) simulations on the measured aperture field. Color - time scale is as described for **figure 39**. MIP is the only approach that yields comparable qualitative and quantitative results (from the experiments of Glass and Nicholl, 1995a).

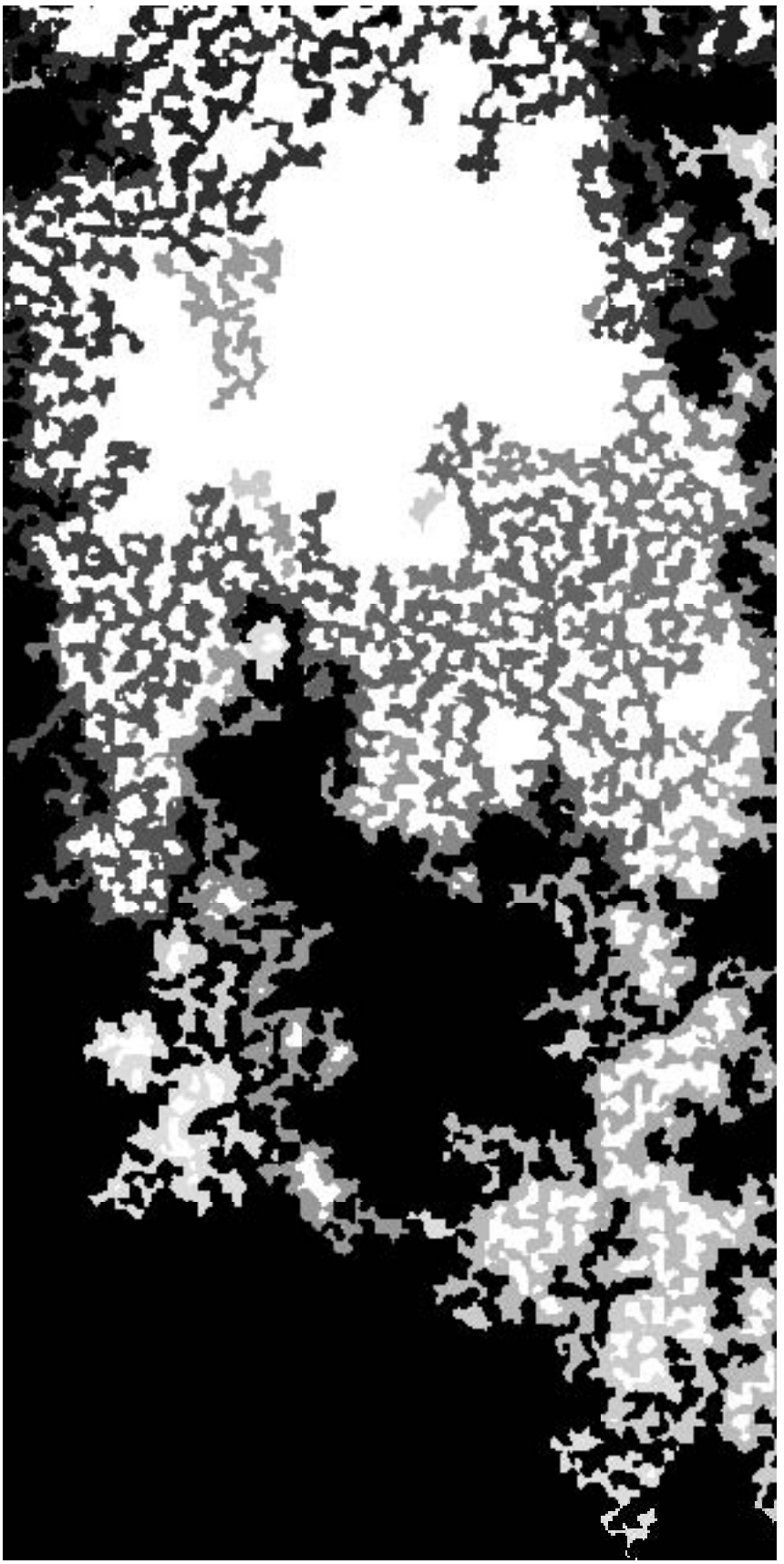

A1: Horizontal Invasion neglecting in-plane curvature, r_2 ($\alpha = 0$)

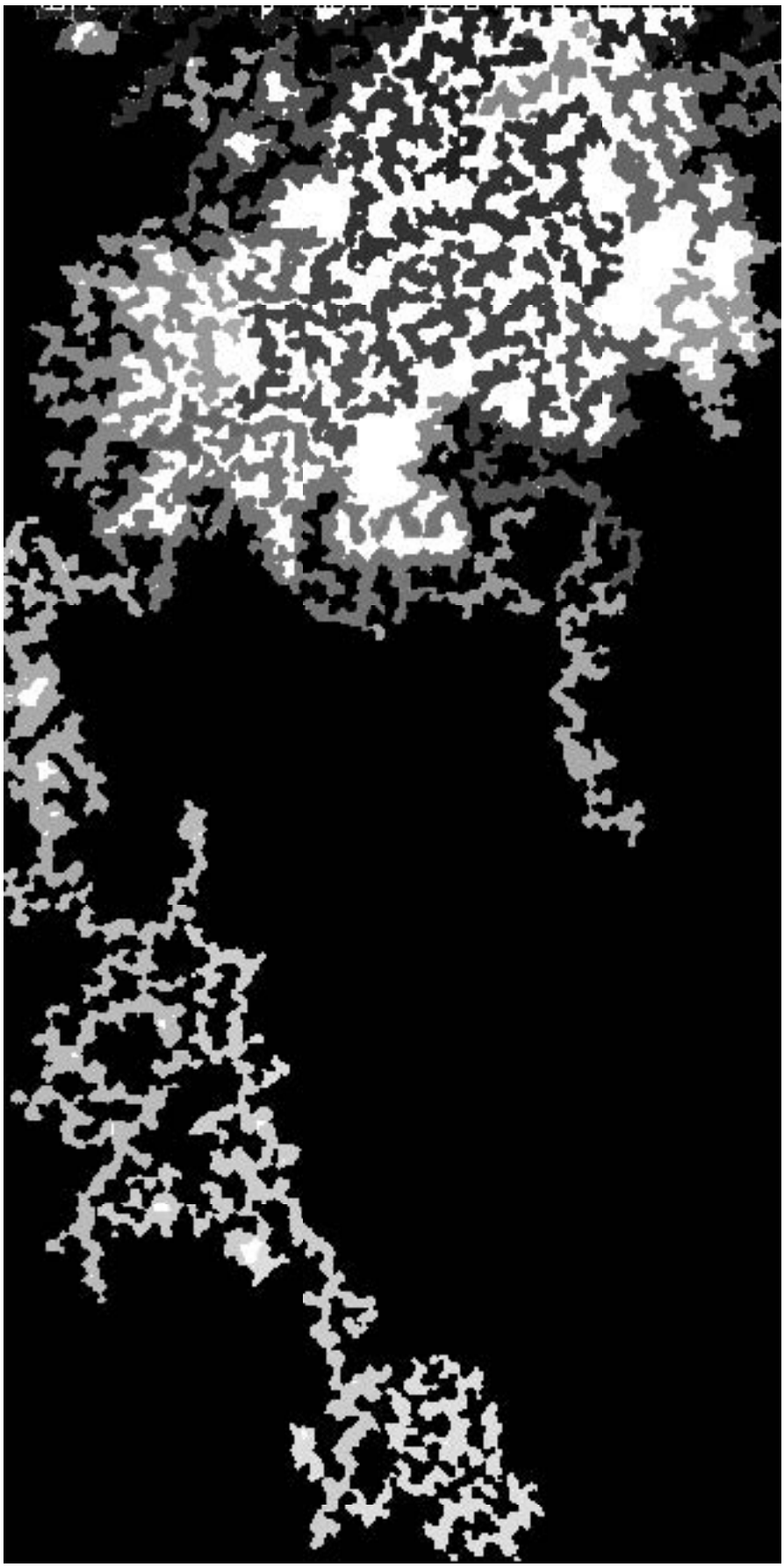

A2: Horizontal Invasion neglecting in-plane curvature, r_2 ($\alpha = 180$)

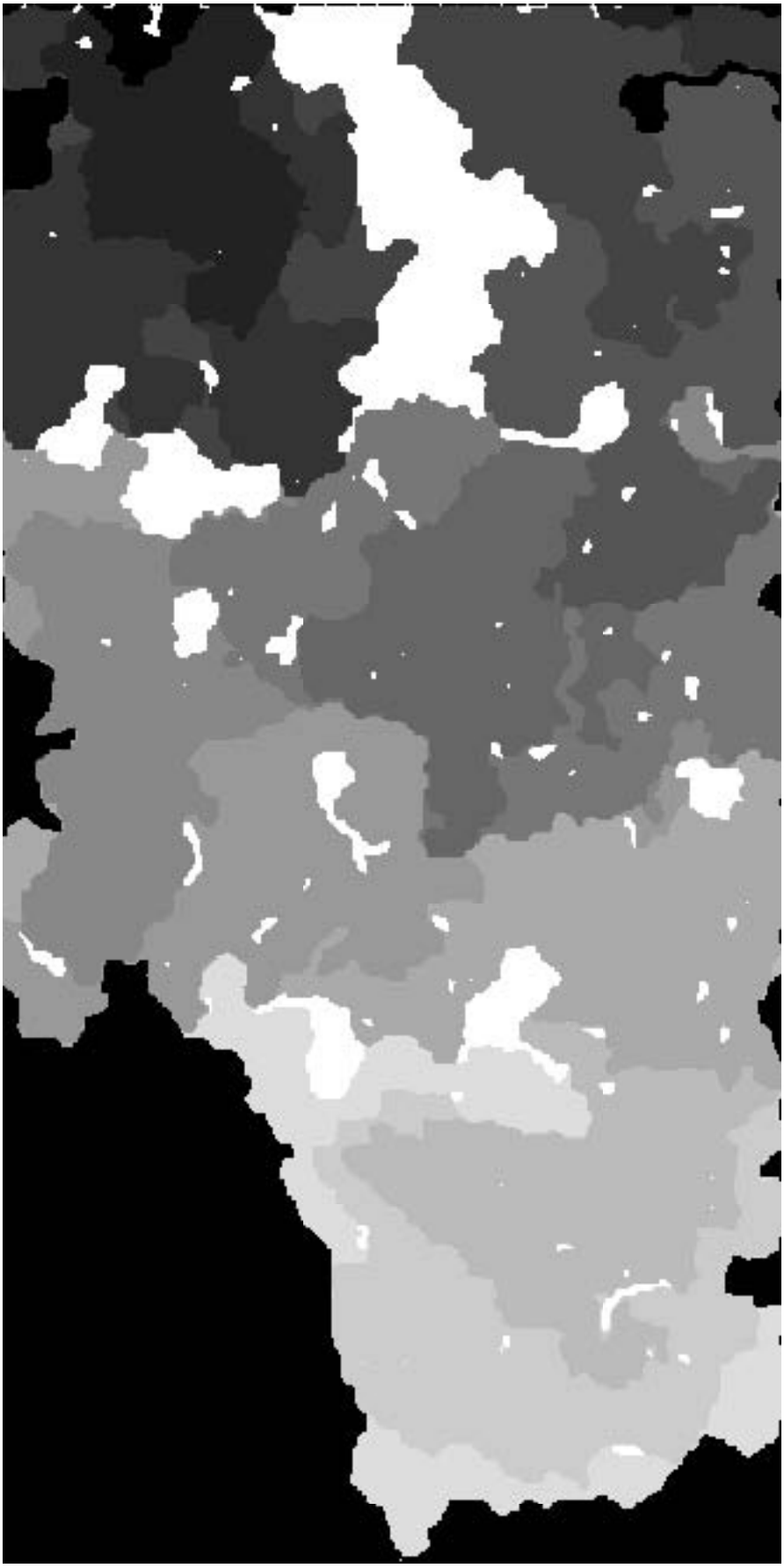

A3: Horizontal Invasion including in-plane curvature, r_2 ($\alpha = 0$)

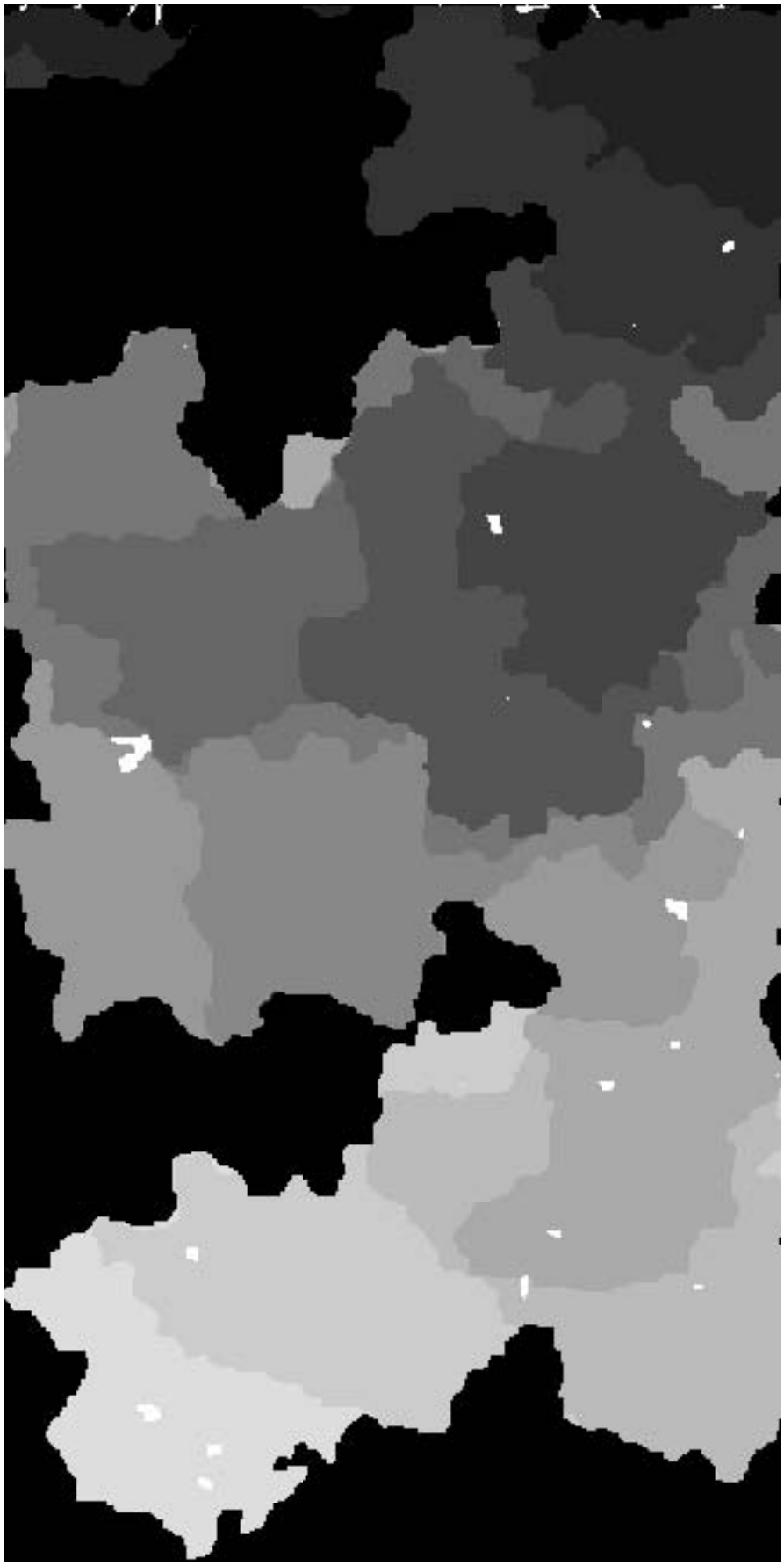

A4: Horizontal Invasion including in-plane curvature, r_2 ($\alpha = 41$)

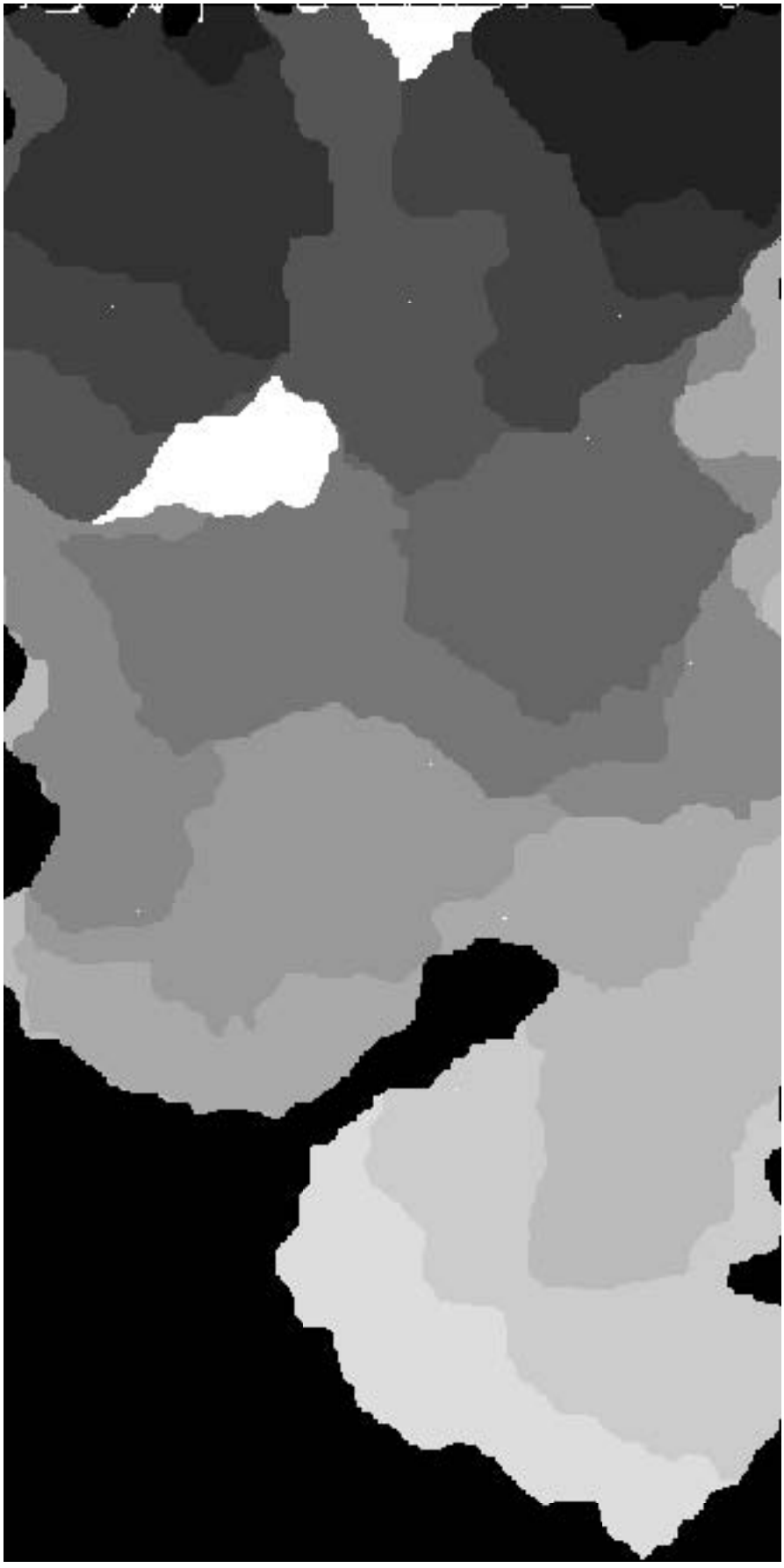

A5: Horizontal Invasion including in-plane curvature, r_2 ($\alpha = 60$)

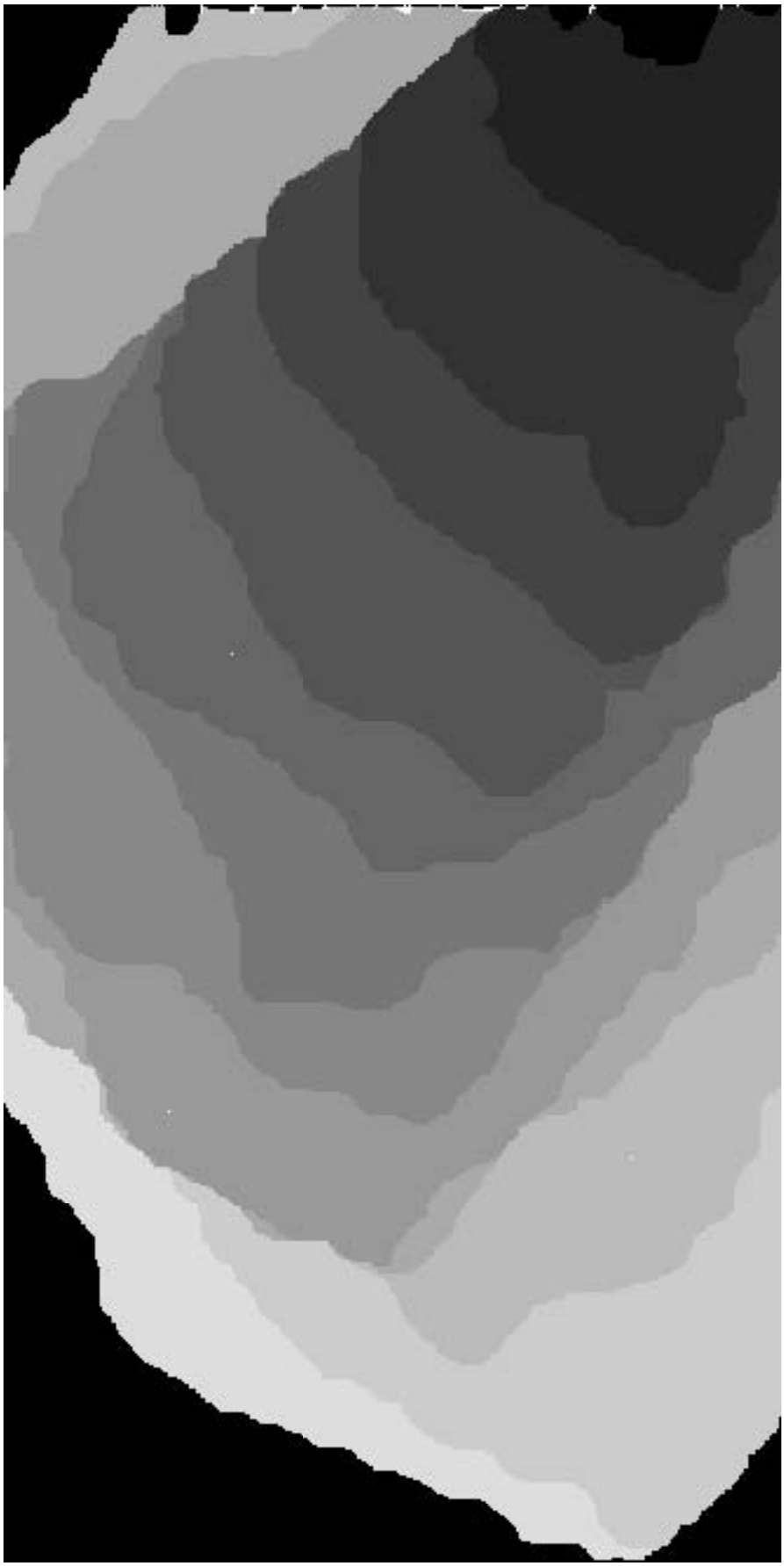

A6: Horizontal Invasion including in-plane curvature, r_2 ($\alpha = 76$)

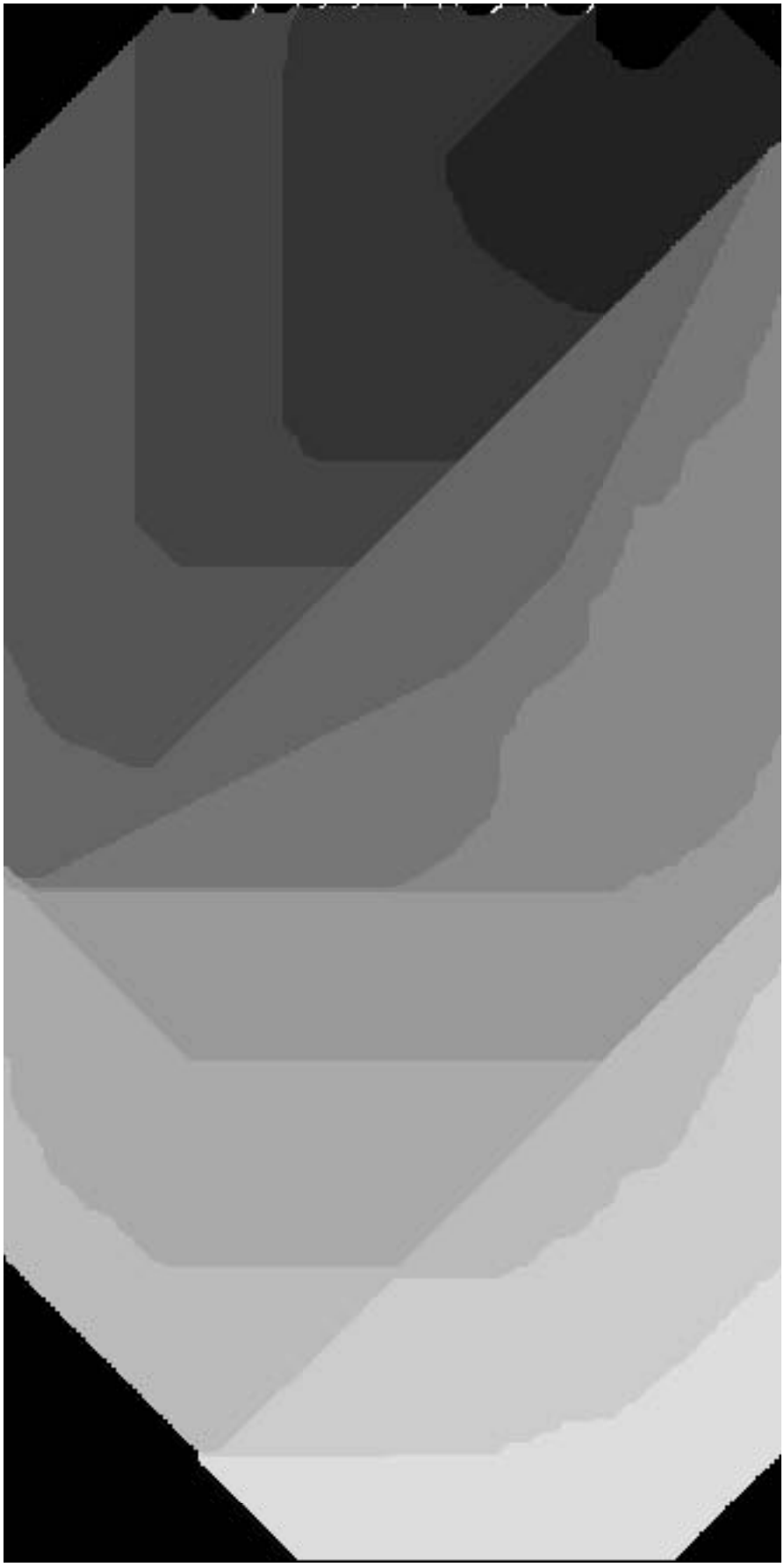

A7: Horizontal Invasion including in-plane curvature, r_2 ($\alpha = 90$)

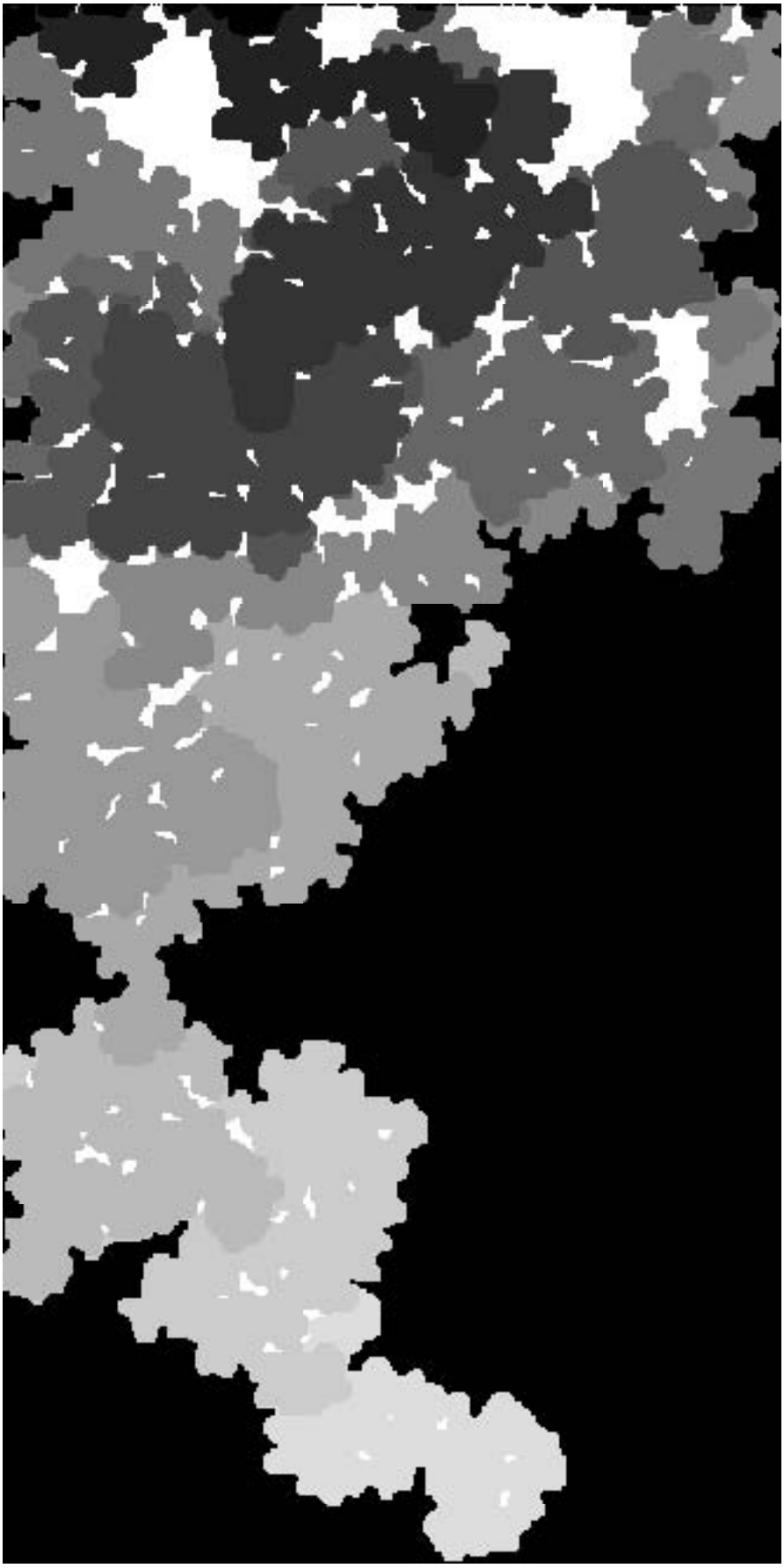

A8: Horizontal Invasion including in-plane curvature, r_2 ($\alpha = 104$)

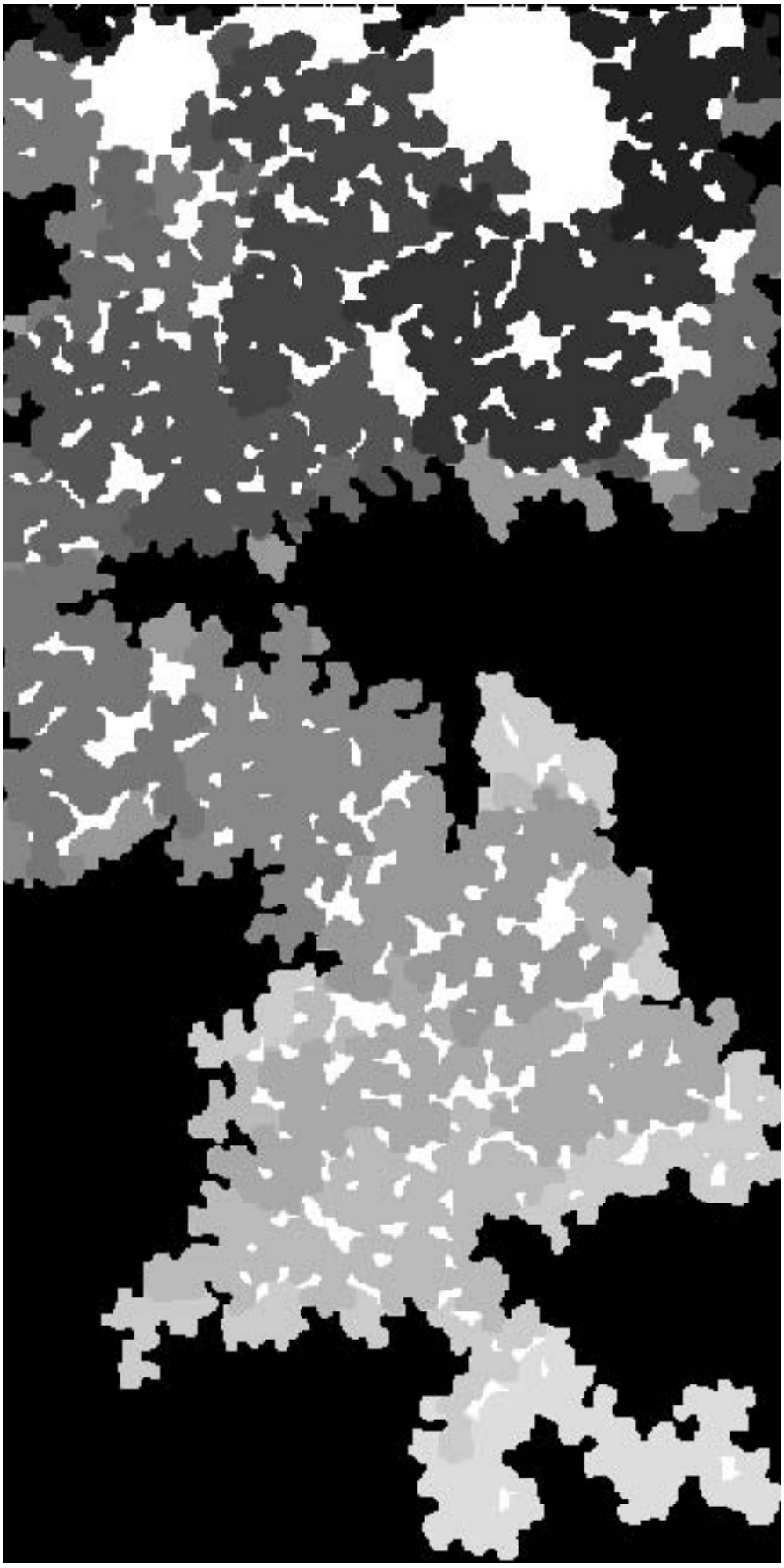

A9: Horizontal Invasion including in-plane curvature, r_2 ($\alpha = 120$)

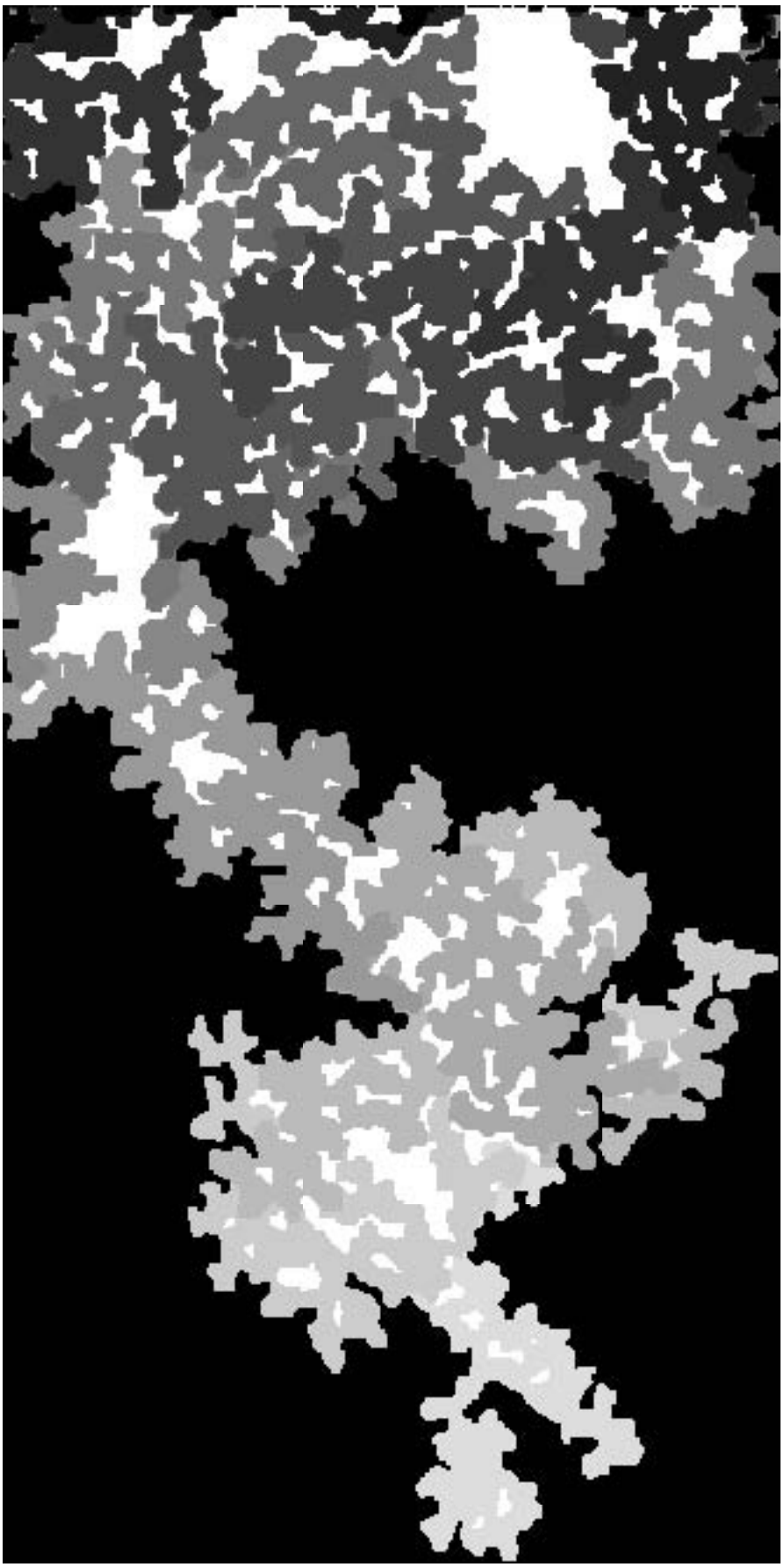

A10: Horizontal Invasion including in-plane curvature, r_2 ($\alpha = 139$)

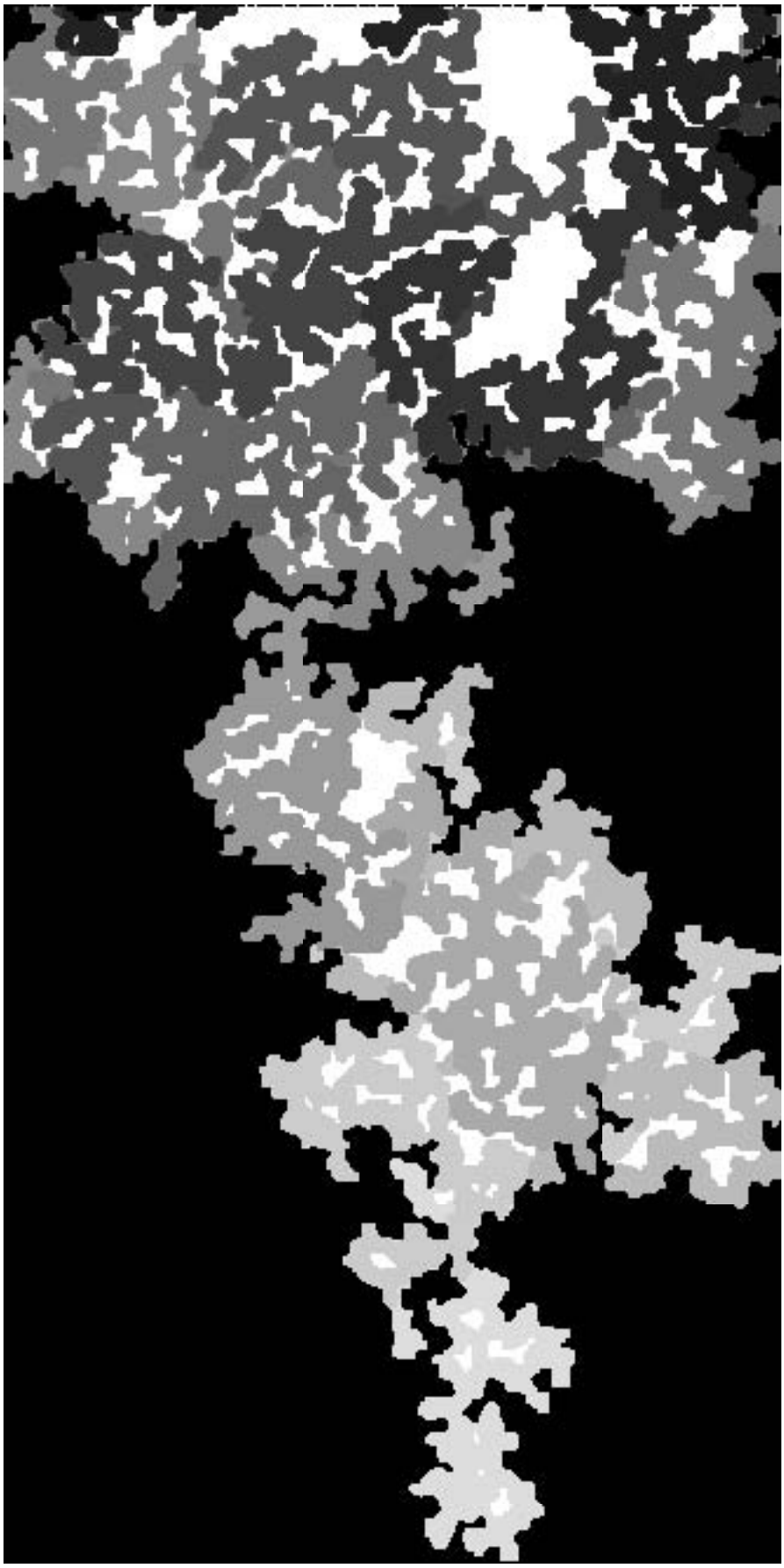

A11: Horizontal Invasion including in-plane curvature, r_2 ($\alpha = 180$)

A12: Gravity-destabilized vertical invasion neglecting in-plane curvature, r_2 ($\alpha = 0$).

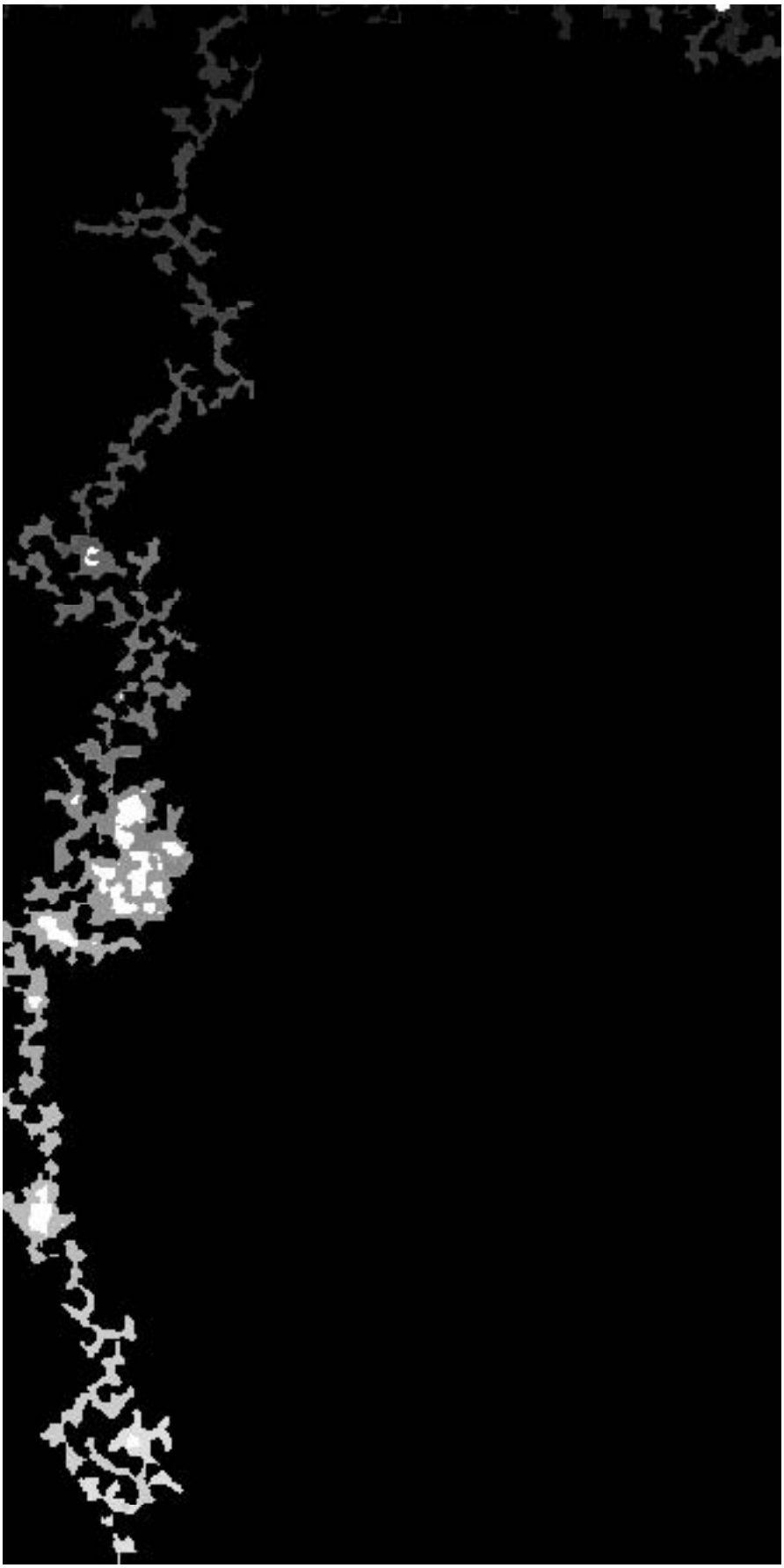

A13: Gravity-destabilized vertical invasion neglecting in-plane curvature, r_2 ($\alpha = 41$).

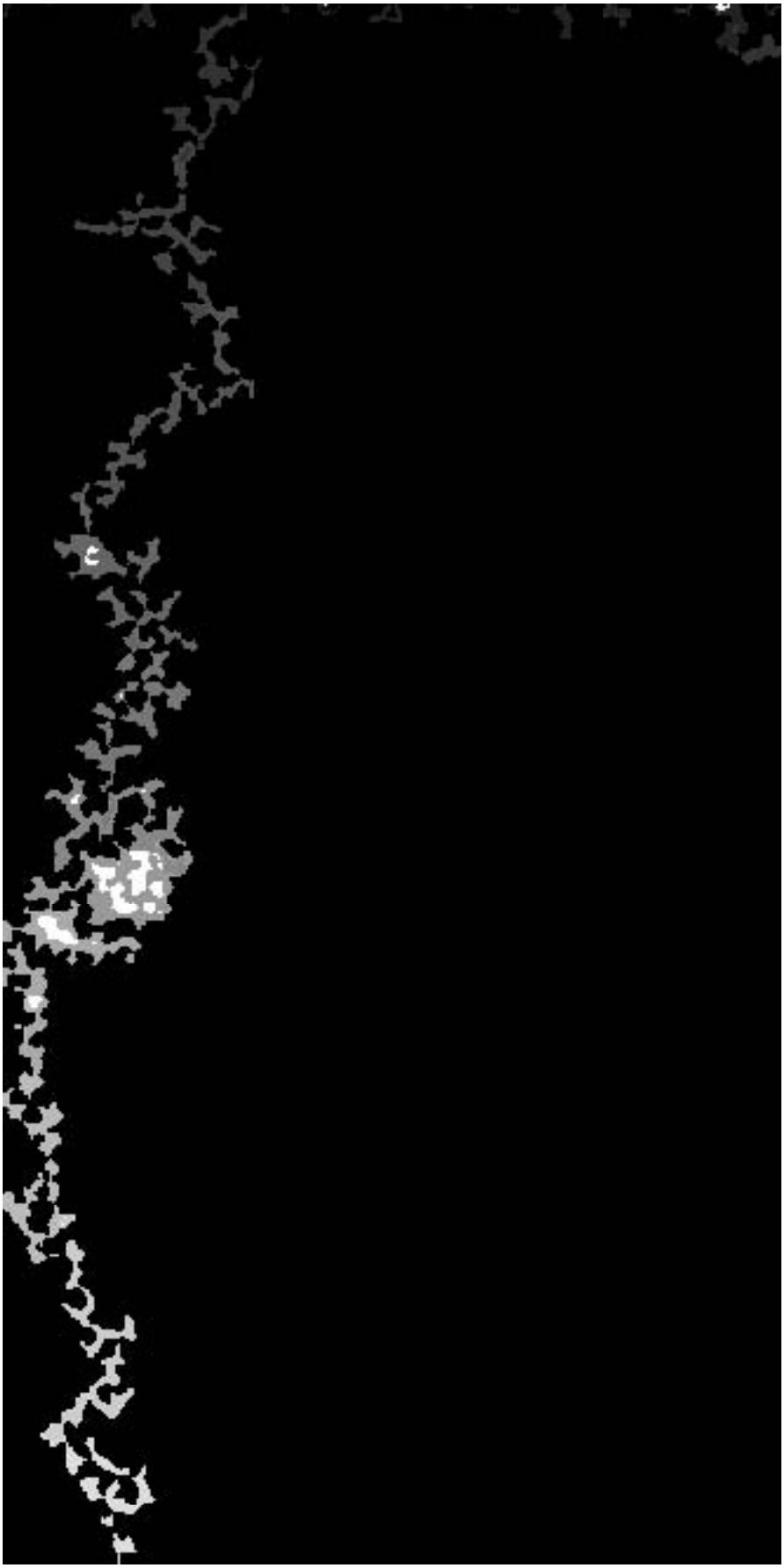

A14: Gravity-destabilized vertical invasion neglecting in-plane curvature, r_2 ($\alpha = 60$).

A15: Gravity-destabilized vertical invasion neglecting in-plane curvature, r_2 ($\alpha = 76$).

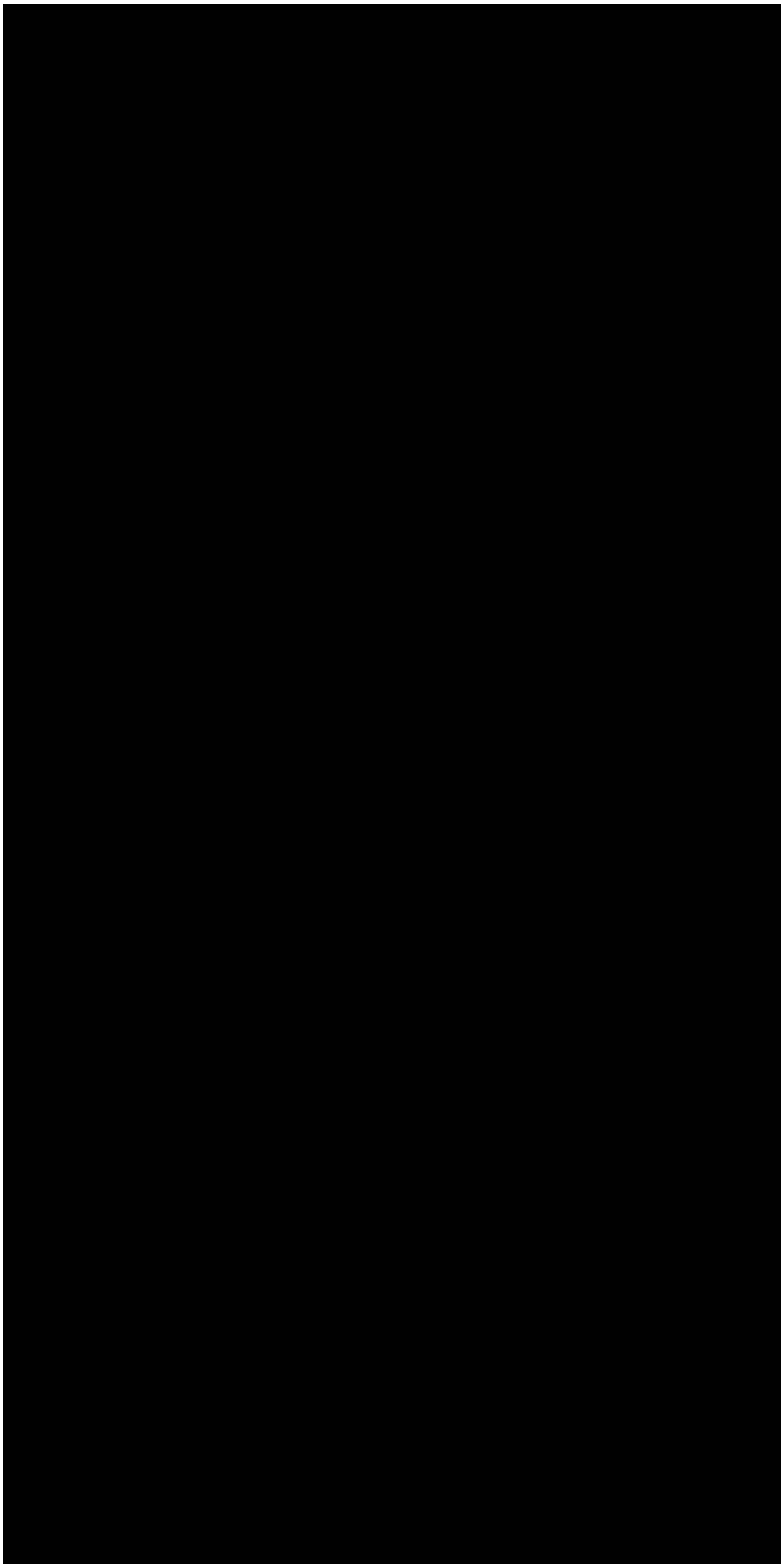

A16: Gravity-destabilized vertical invasion neglecting in-plane curvature, r_2 ($\alpha = 90$).

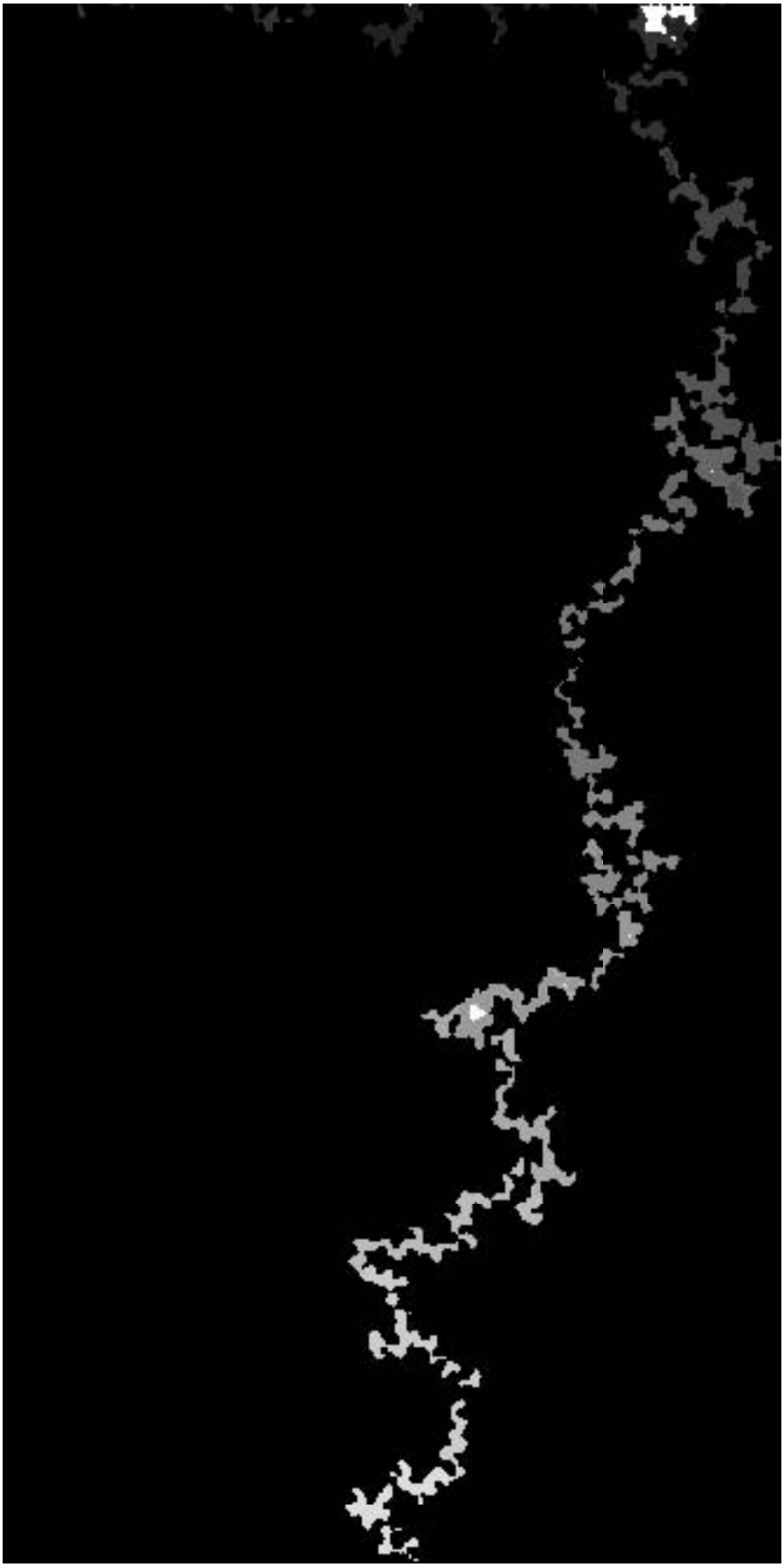

A17: Gravity-destabilized vertical invasion neglecting in-plane curvature, r_2 ($\alpha = 104$).

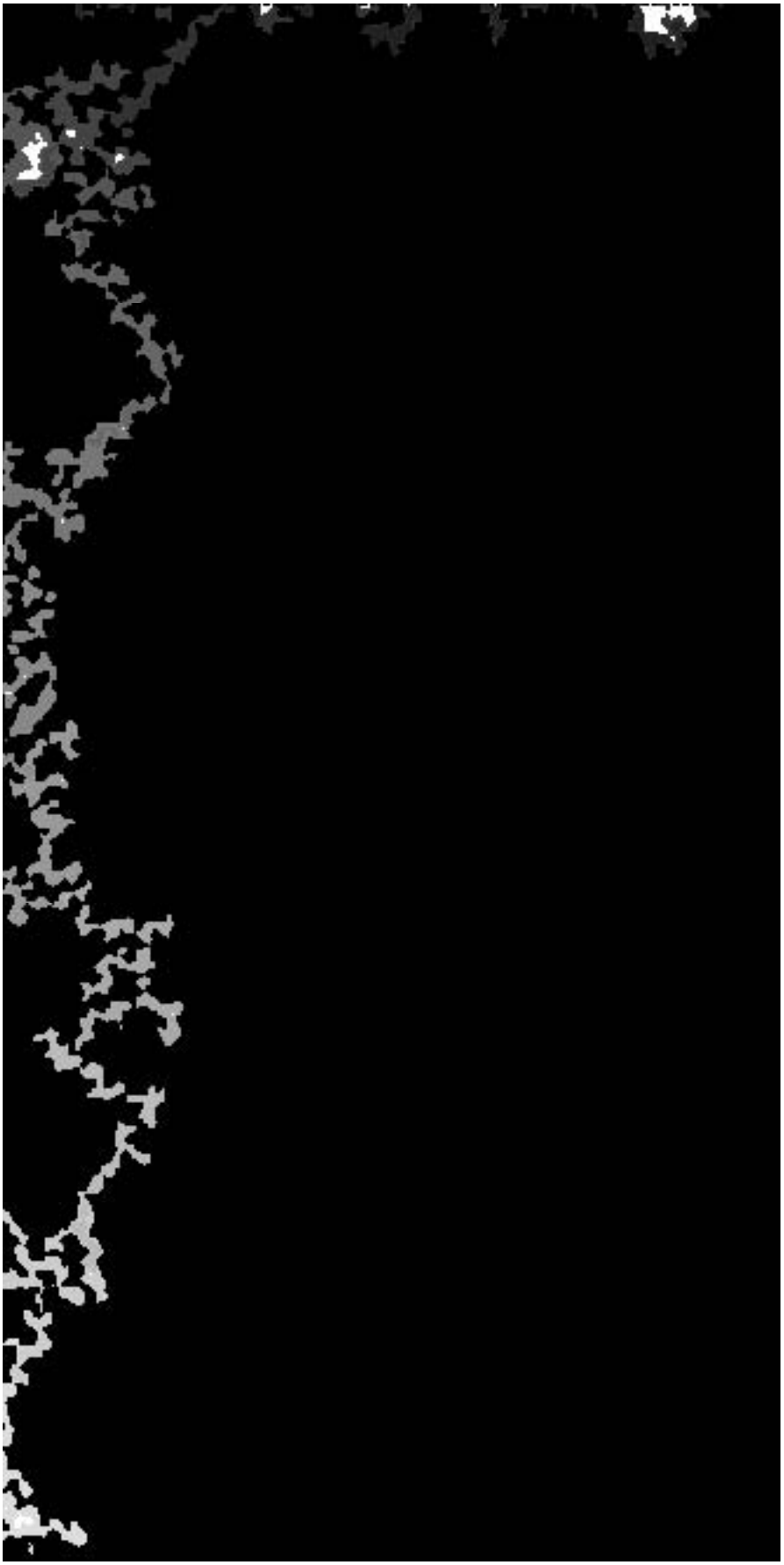

A18: Gravity-destabilized vertical invasion neglecting in-plane curvature, r_2 ($\alpha = 120$).

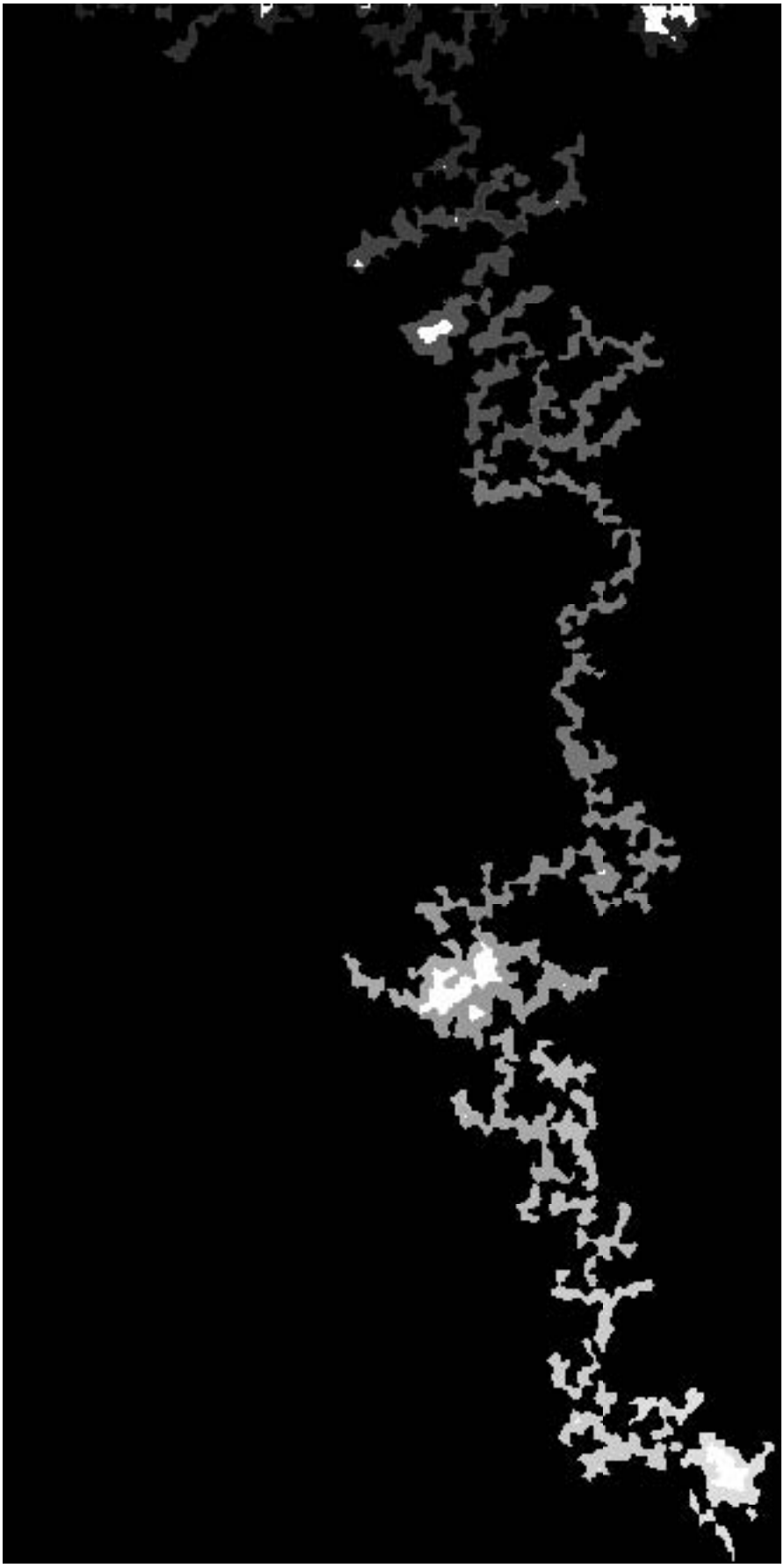

A19: Gravity-destabilized vertical invasion neglecting in-plane curvature, r_2 ($\alpha = 139$).

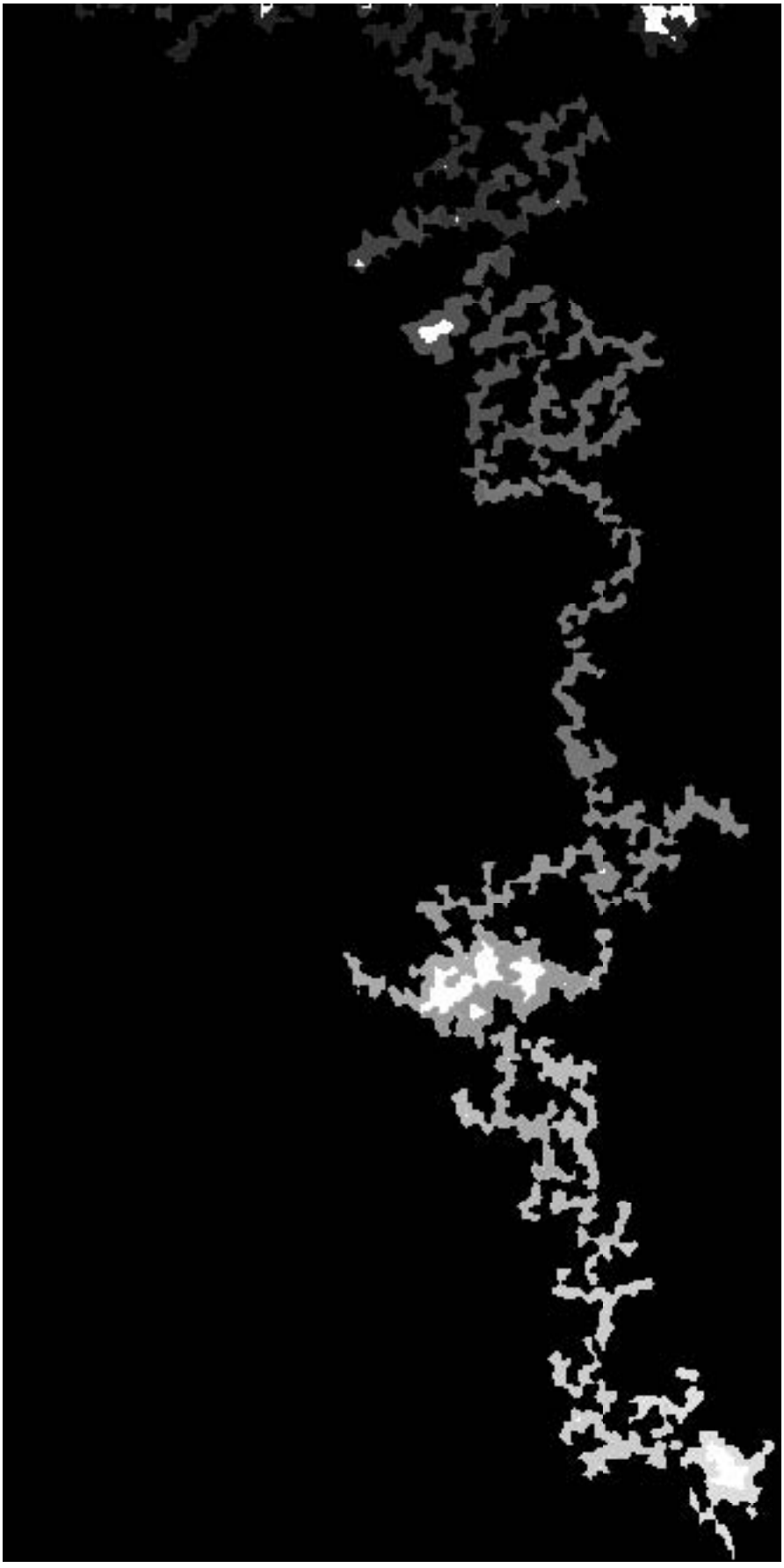

A20: Gravity-destabilized vertical invasion neglecting in-plane curvature, r_2 ($\alpha = 180$).

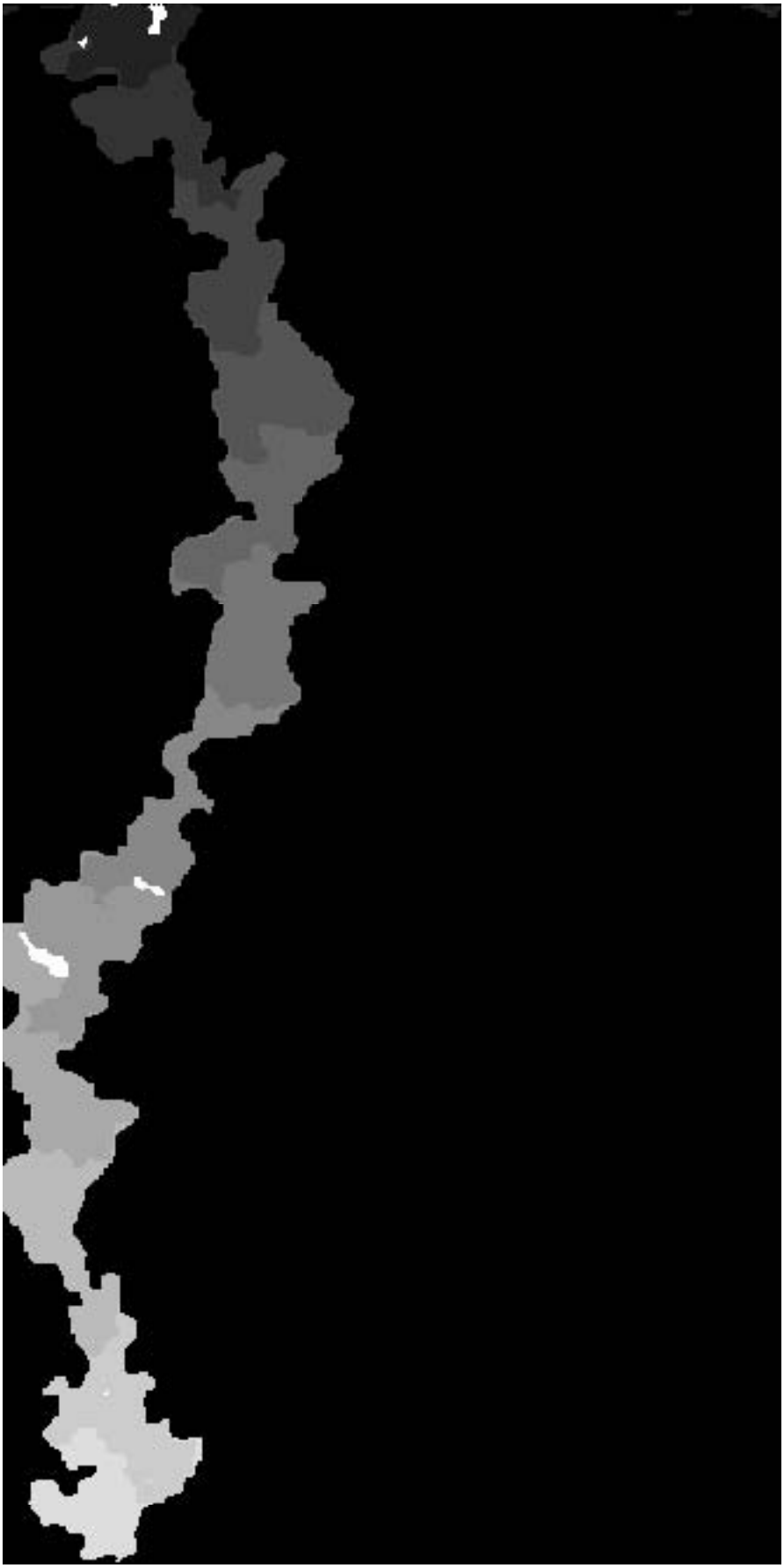

A21: Gravity-destabilized vertical invasion including in-plane curvature, r_2 ($\alpha = 0$).

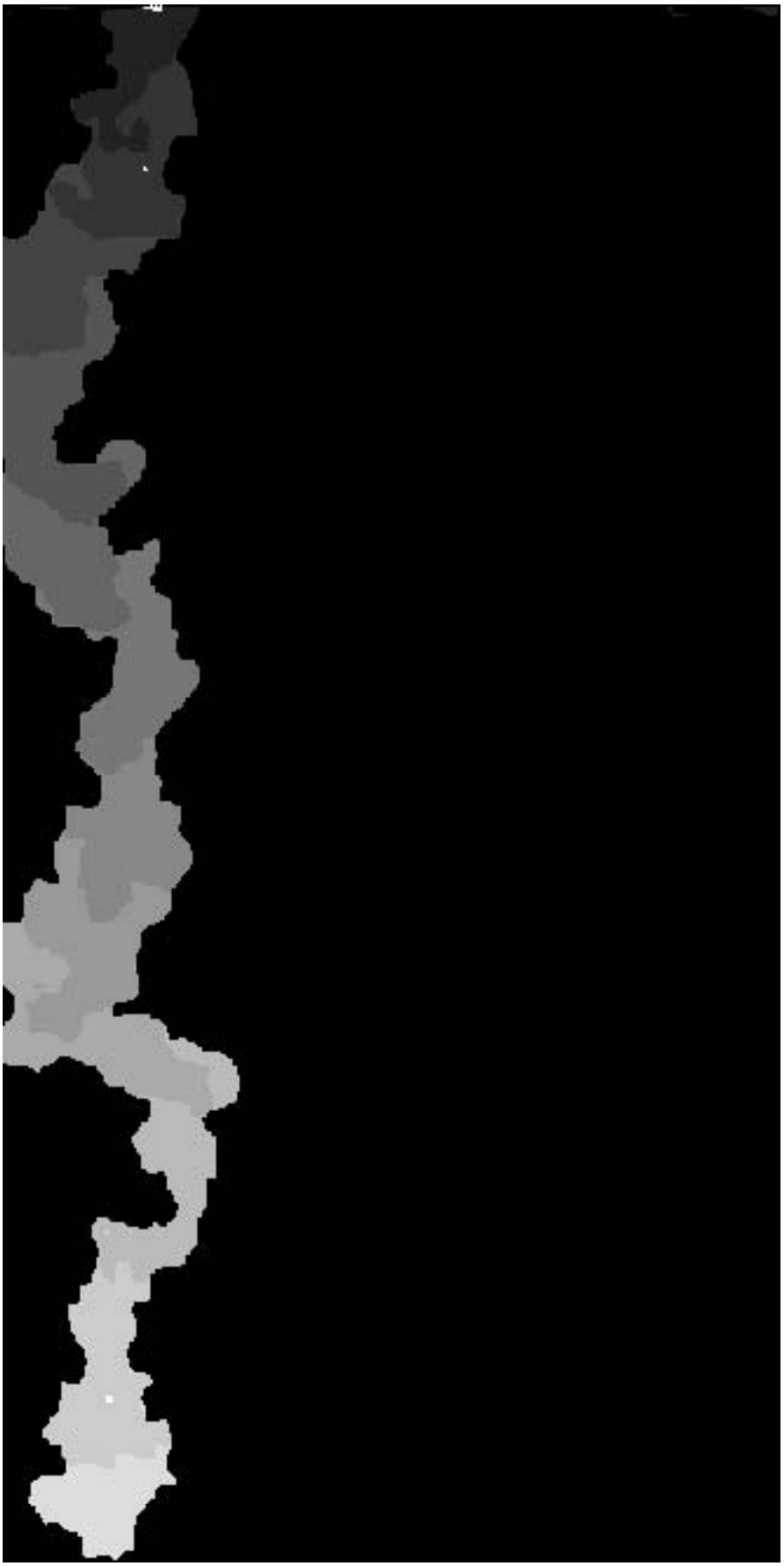

A22: Gravity-destabilized vertical invasion including in-plane curvature, r_2 ($\alpha = 41$).

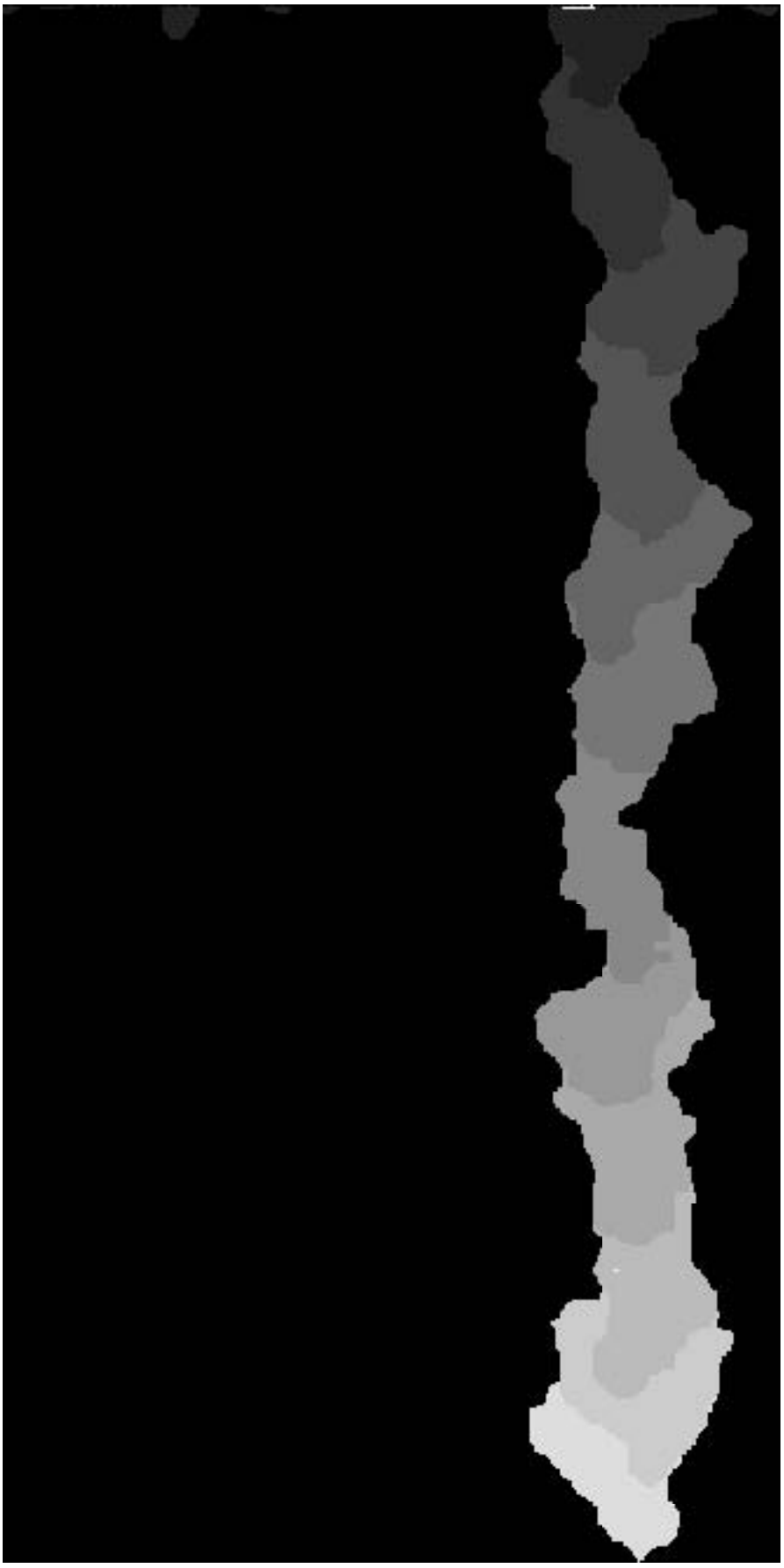

A23: Gravity-destabilized vertical invasion including in-plane curvature, r_2 ($\alpha = 60$).

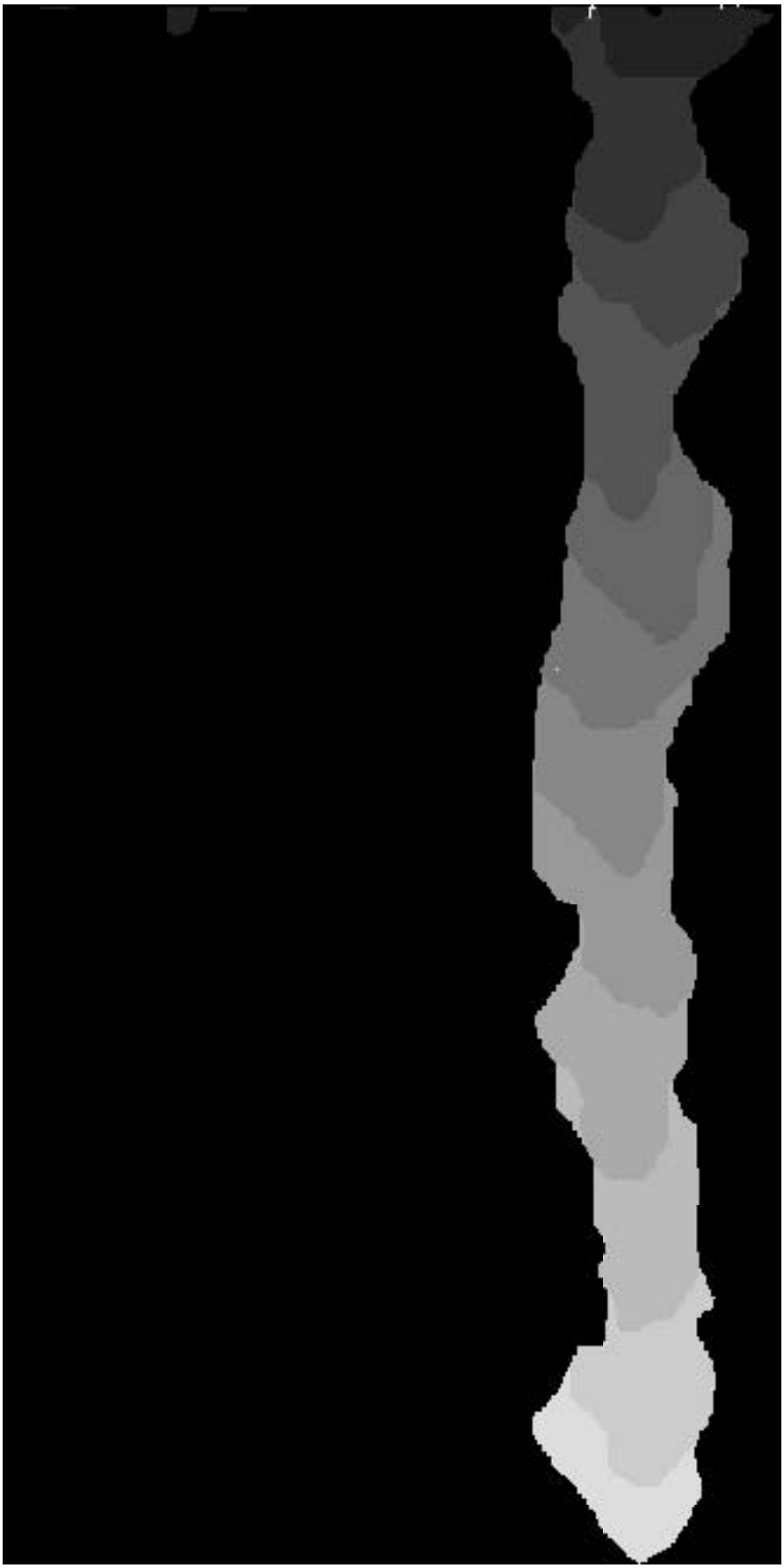

A24: Gravity-destabilized vertical invasion including in-plane curvature, r_2 ($\alpha = 76$).

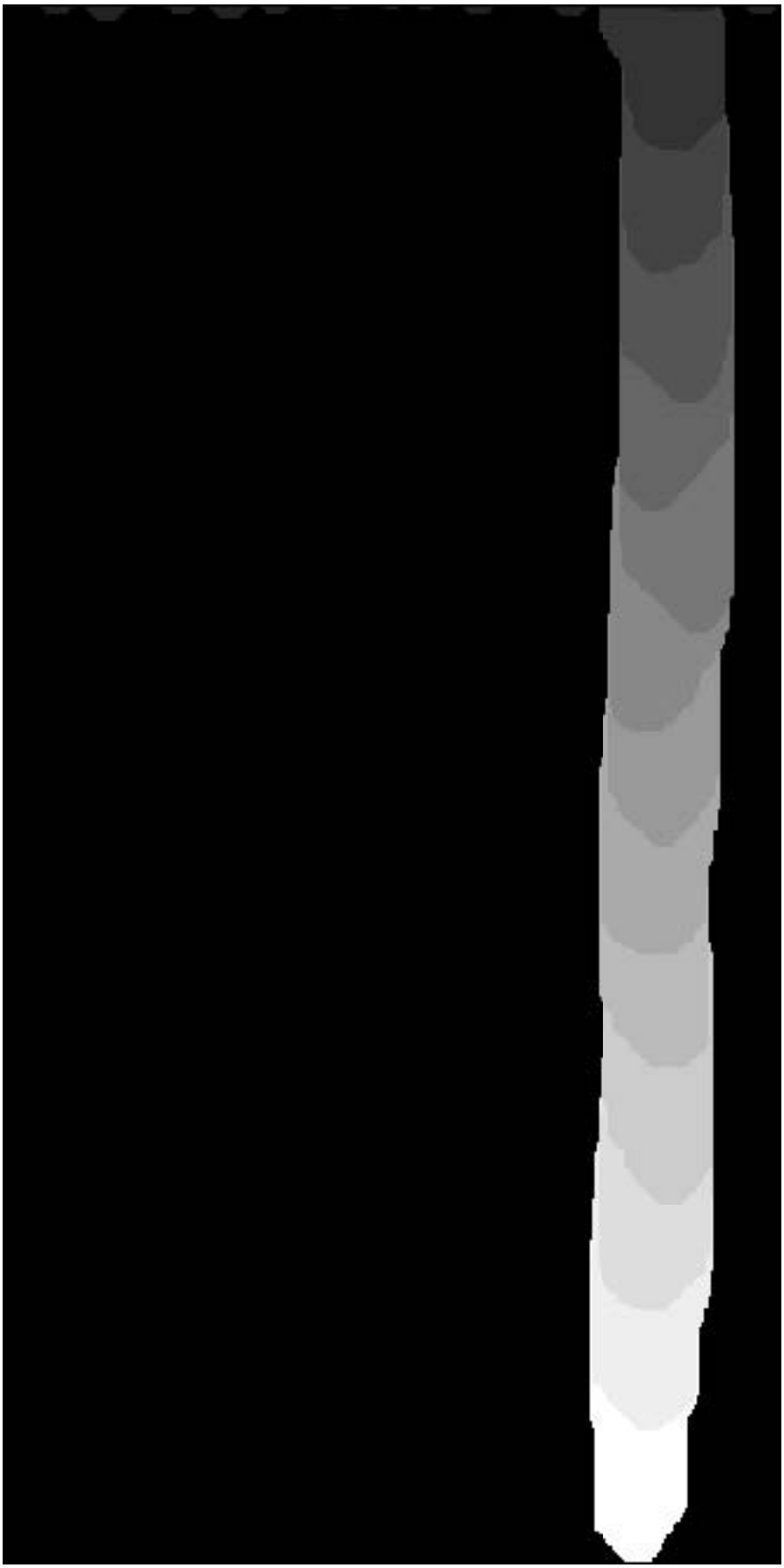

A25: Gravity-destabilized vertical invasion including in-plane curvature, r_2 ($\alpha = 90$).

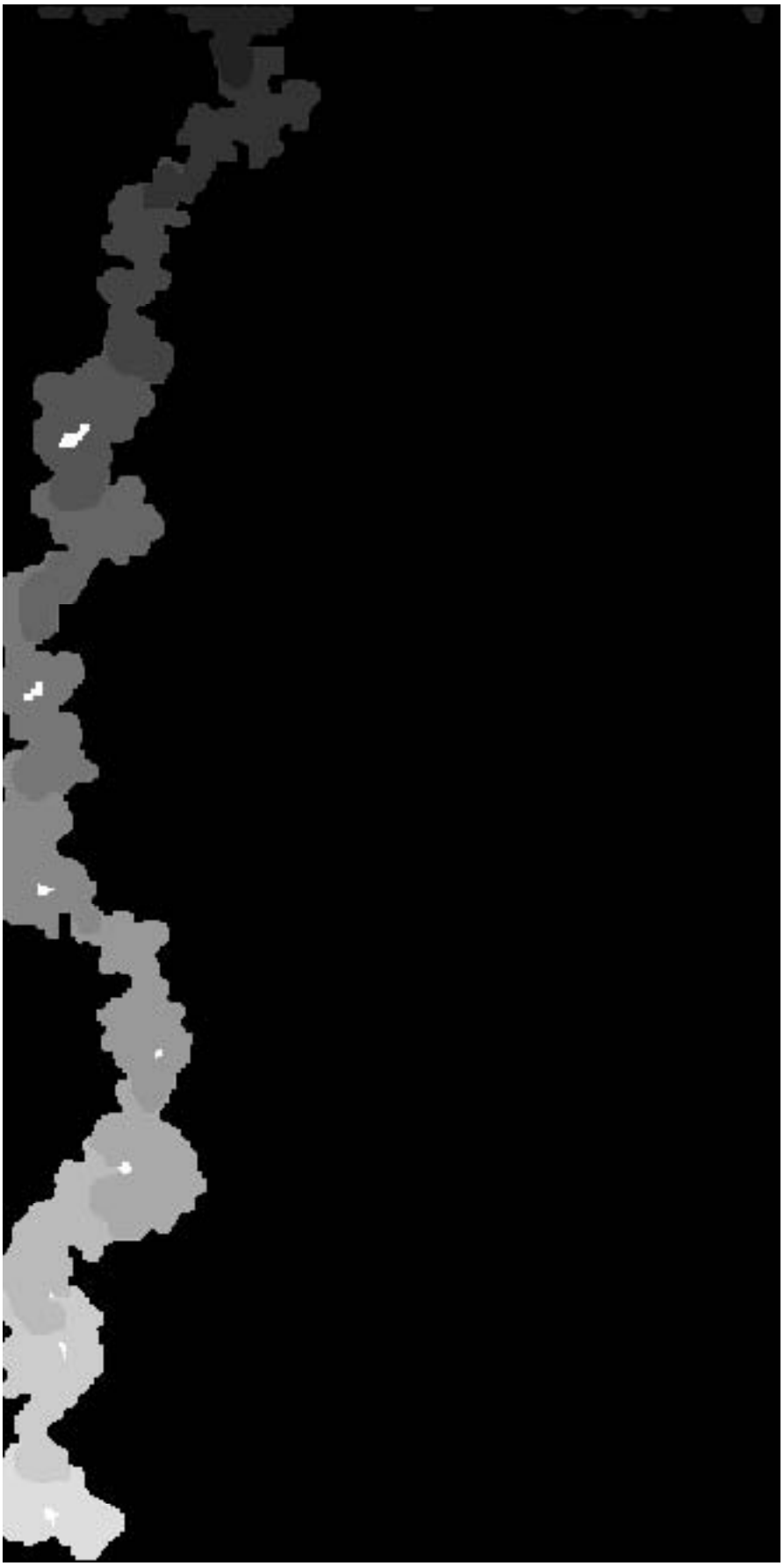

A26: Gravity-destabilized vertical invasion including in-plane curvature, r_2 ($\alpha = 104$).

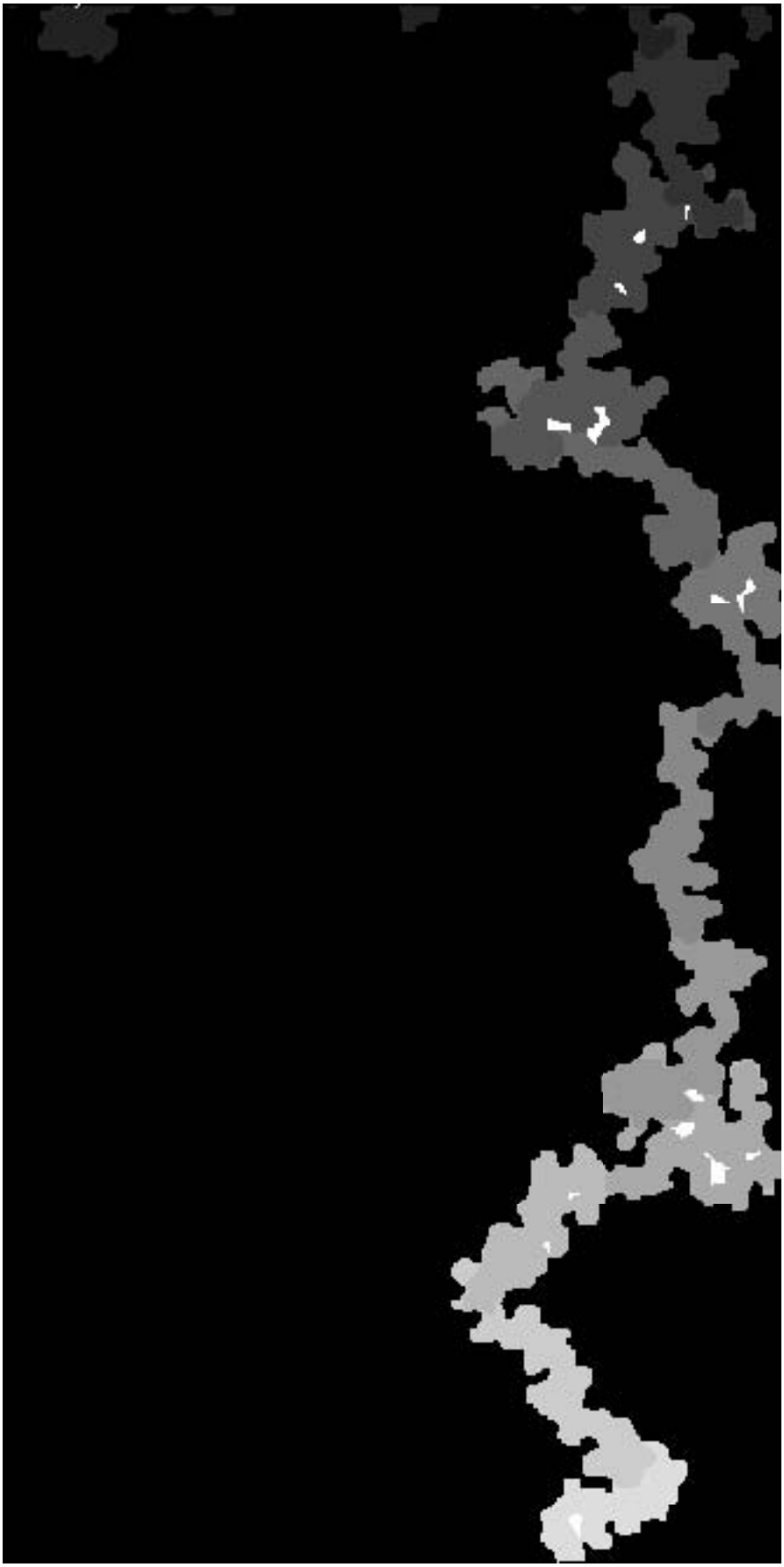

A27: Gravity-destabilized vertical invasion including in-plane curvature, r_2 ($\alpha = 120$).

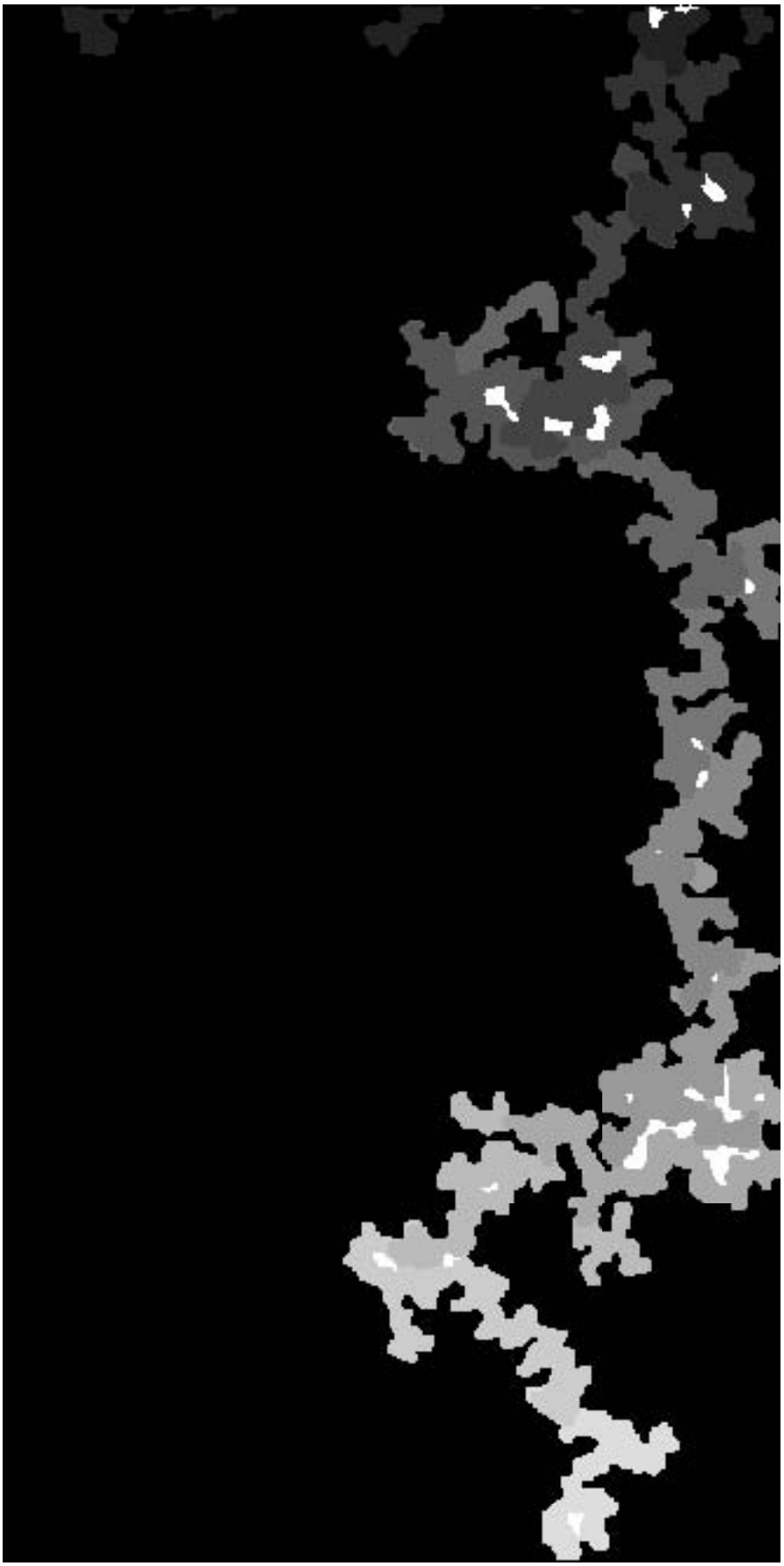

A28: Gravity-destabilized vertical invasion including in-plane curvature, r_2 ($\alpha = 139$).

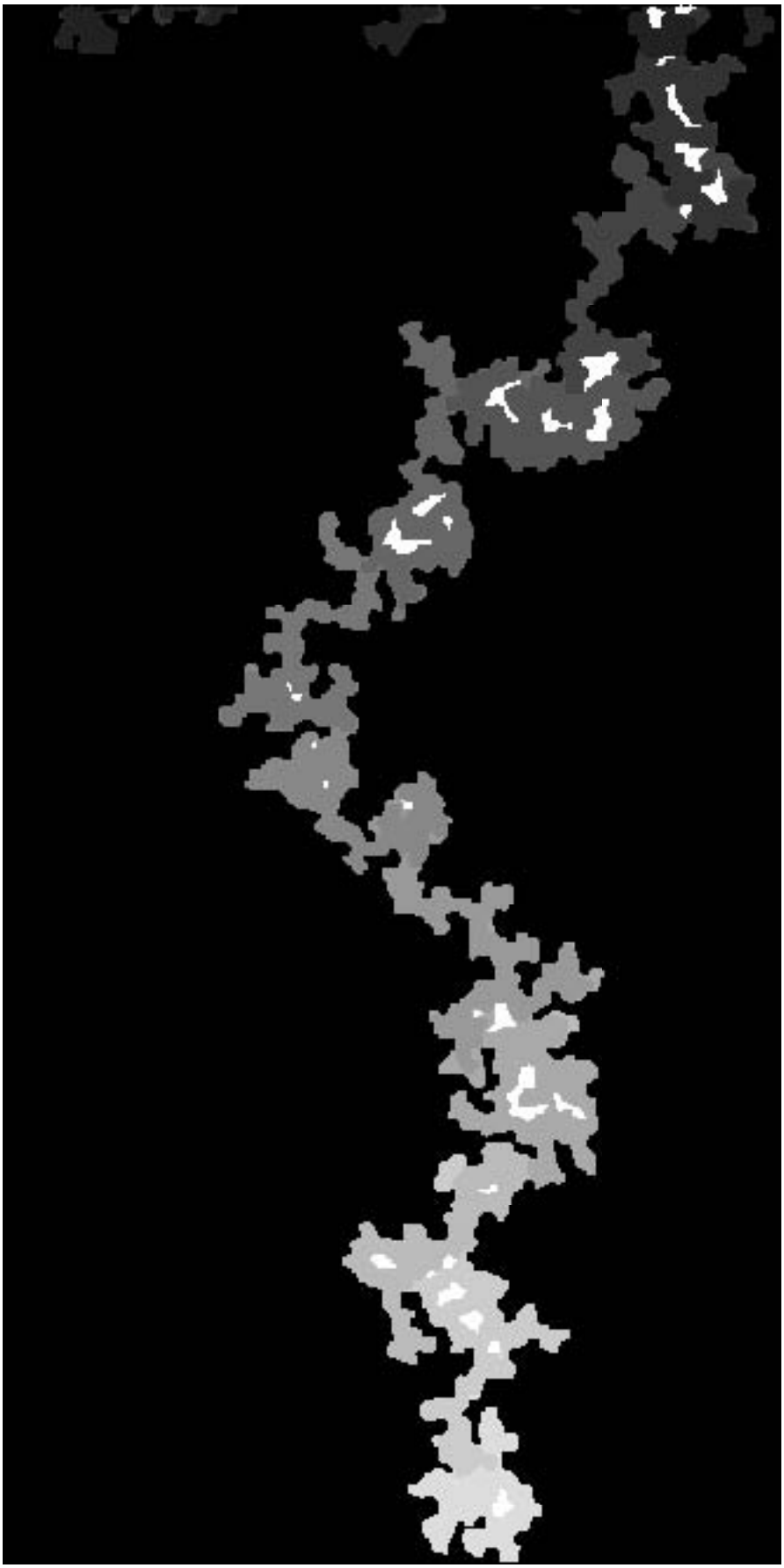

A29: Gravity-destabilized vertical invasion including in-plane curvature, r_2 ($\alpha = 180$).

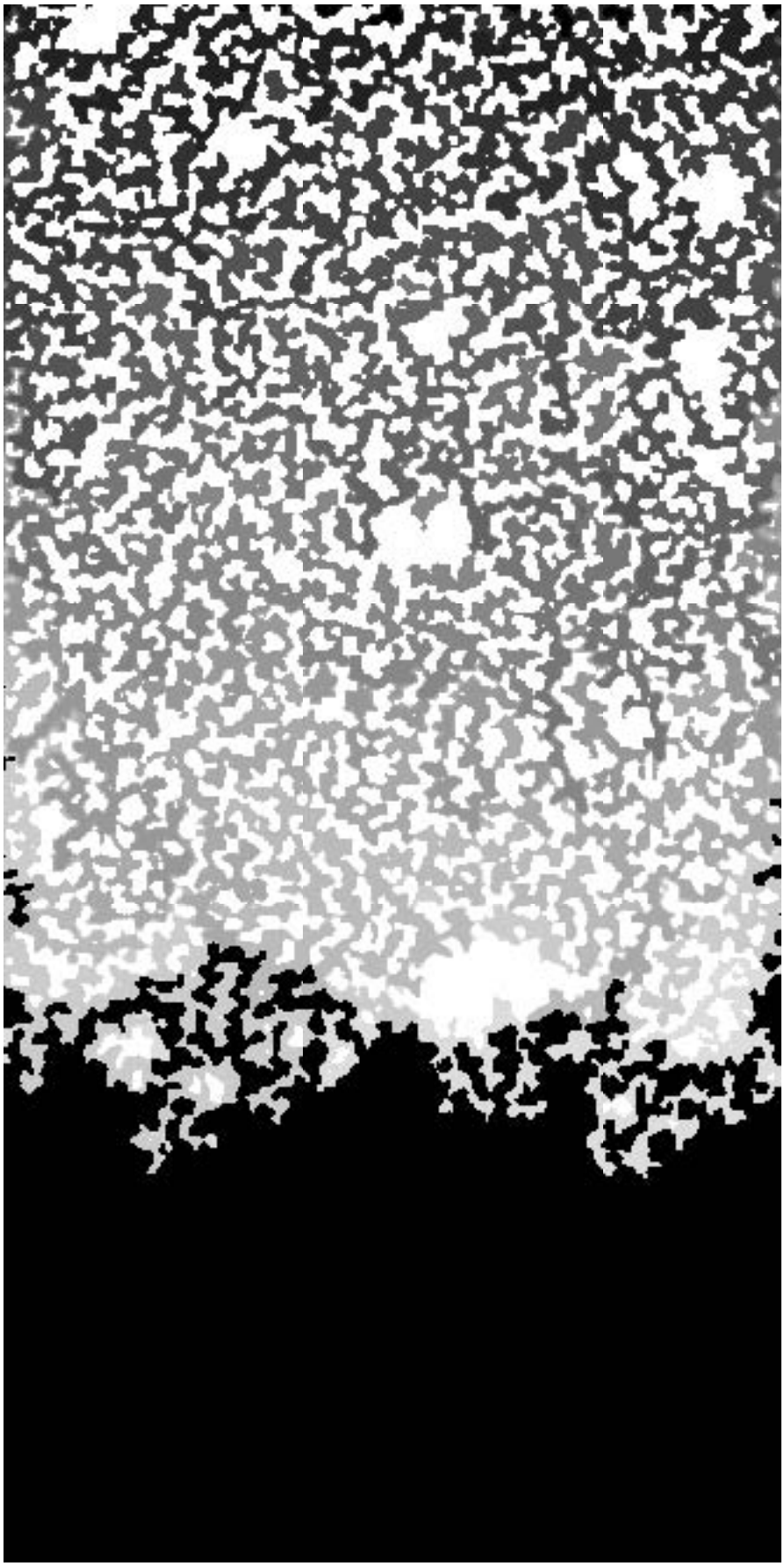

A30: Gravity-stabilized vertical invasion neglecting in-plane curvature, r_2 ($\alpha = 0$).

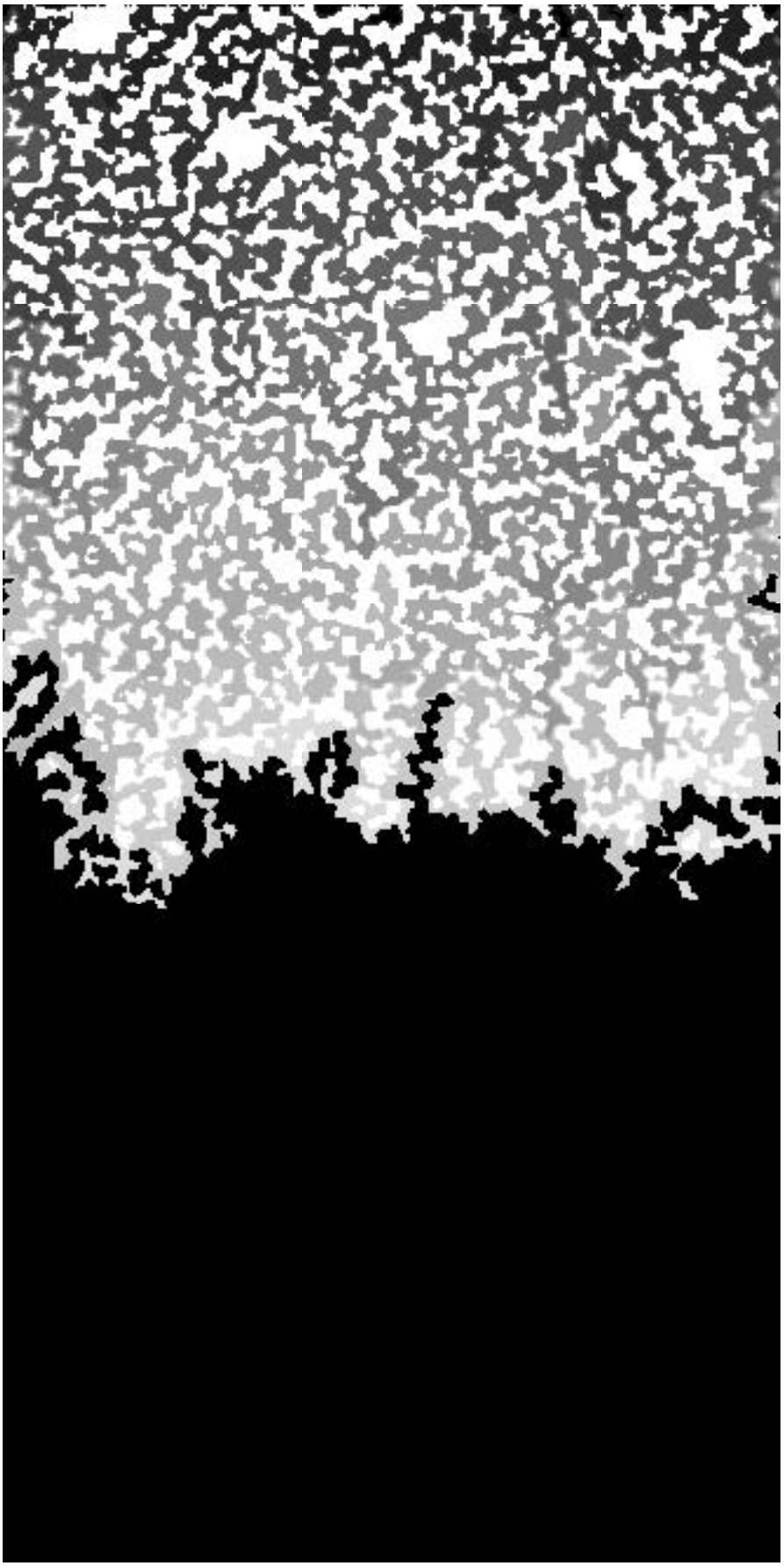

A31: Gravity-stabilized vertical invasion neglecting in-plane curvature, r_2 ($\alpha = 41$).

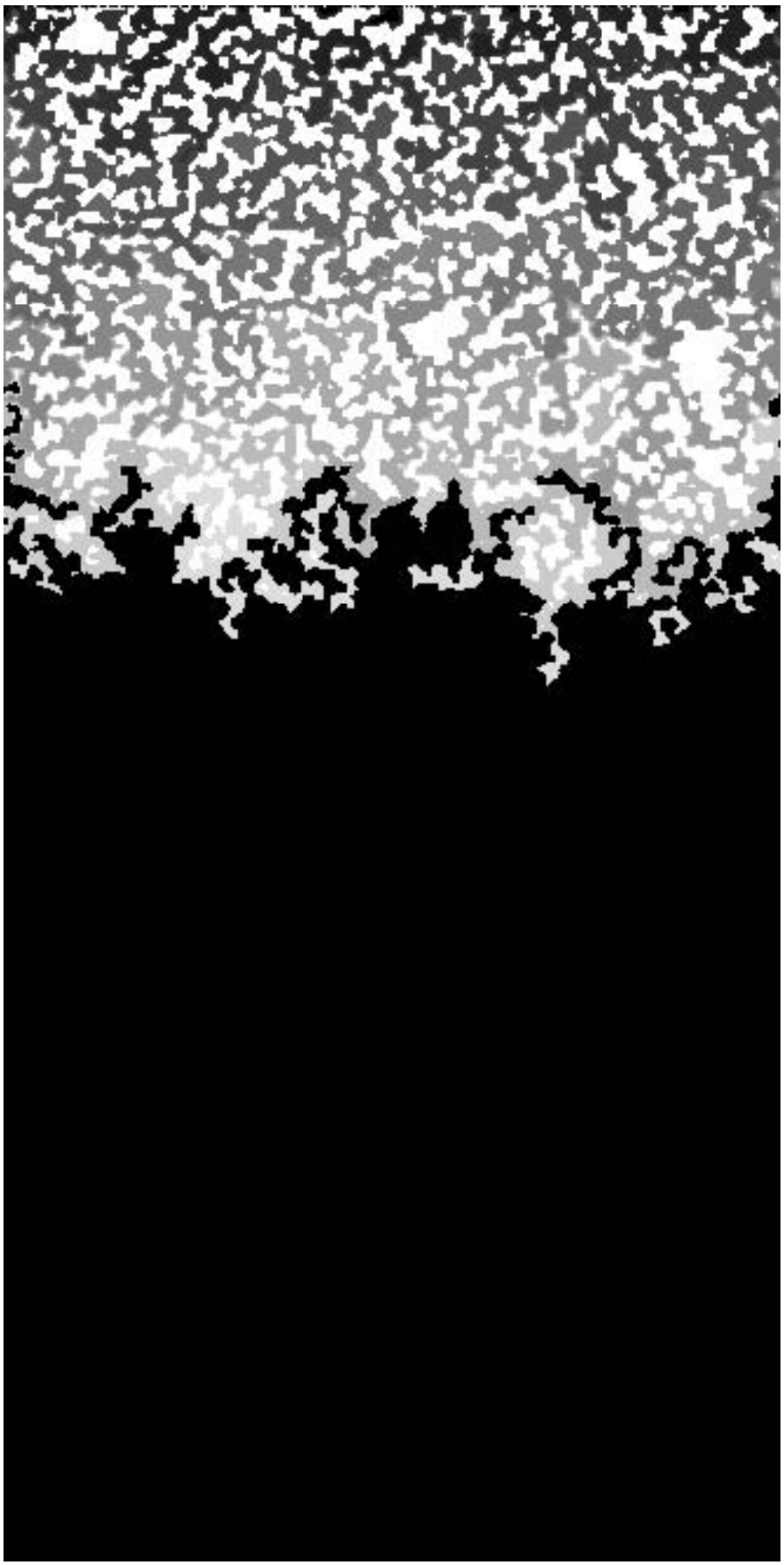

A32: Gravity-stabilized vertical invasion neglecting in-plane curvature, r_2 ($\alpha = 60$).

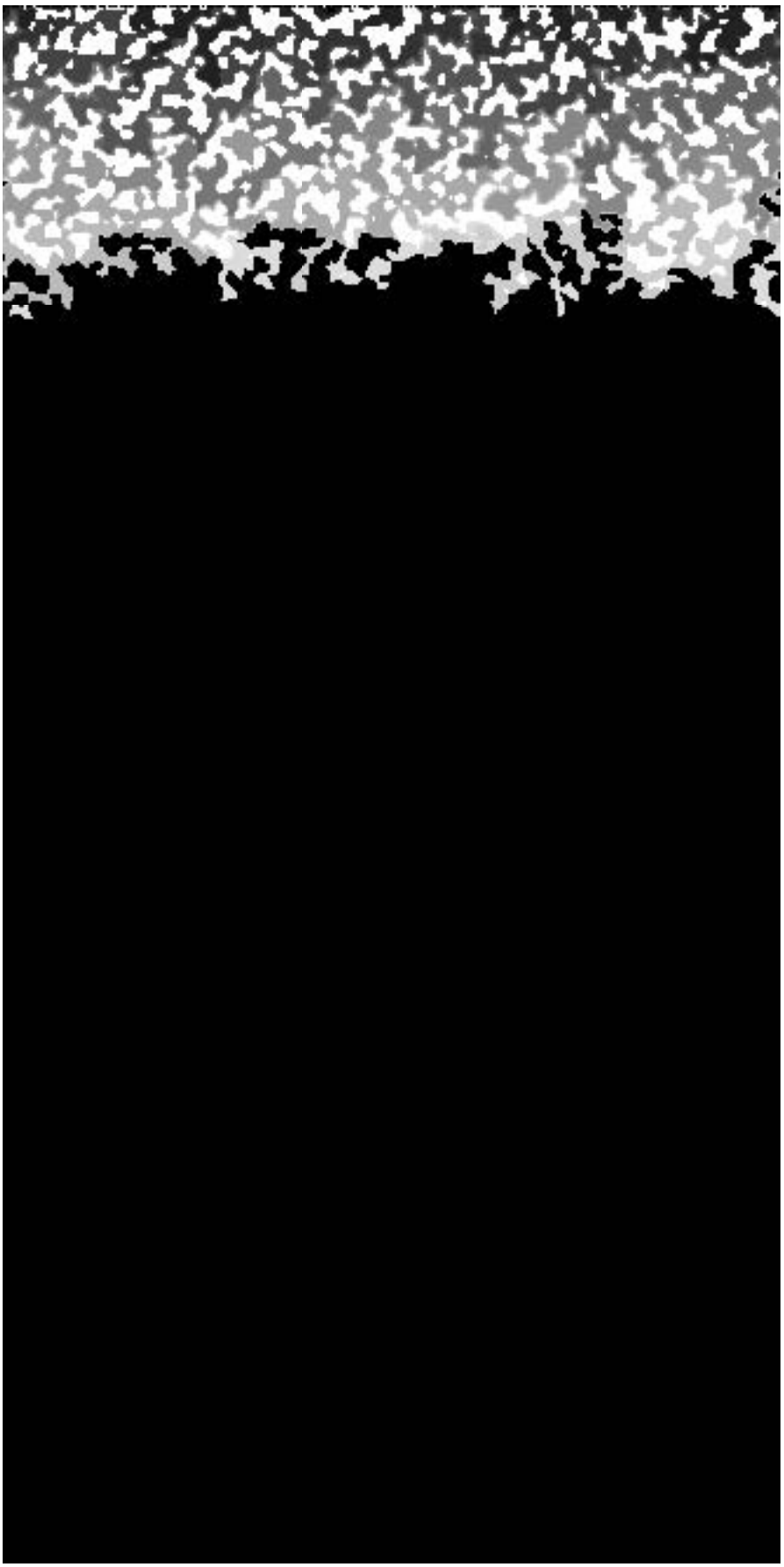

A33: Gravity-stabilized vertical invasion neglecting in-plane curvature, r_2 ($\alpha = 76$).

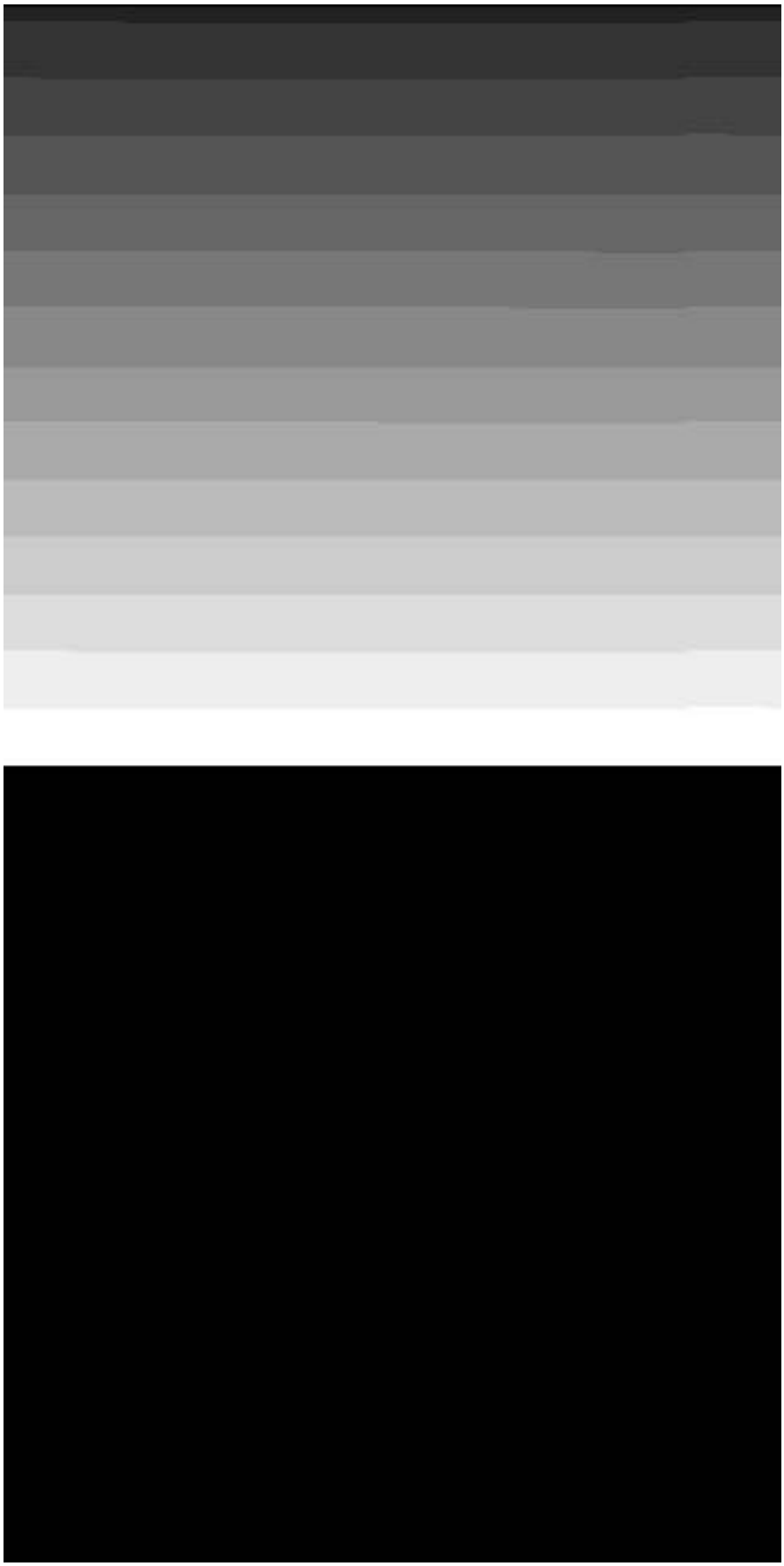

A34: Gravity-stabilized vertical invasion neglecting in-plane curvature, r_2 ($\alpha = 90$).

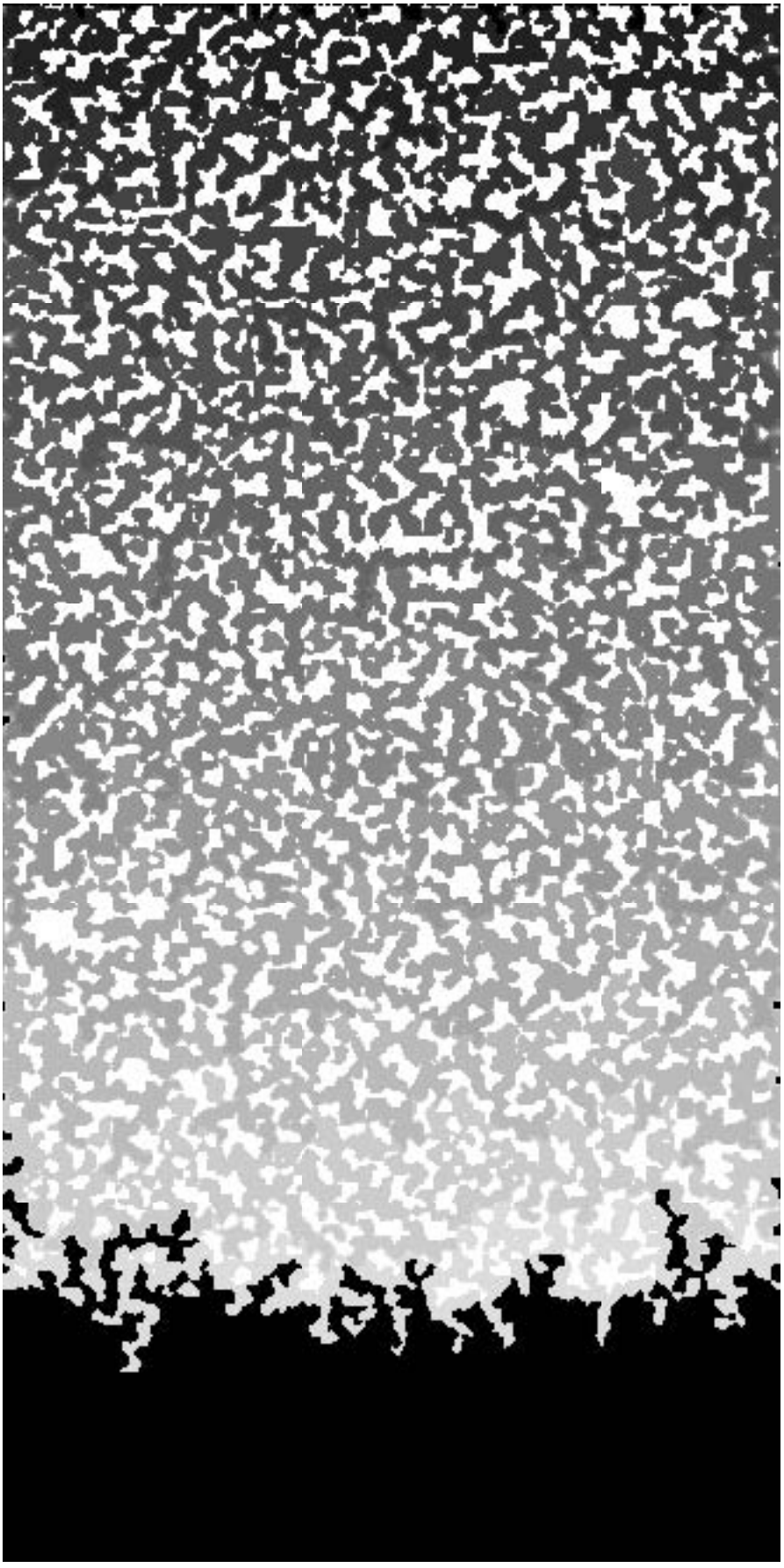

A35: Gravity-stabilized vertical invasion neglecting in-plane curvature, r_2 ($\alpha = 104$).

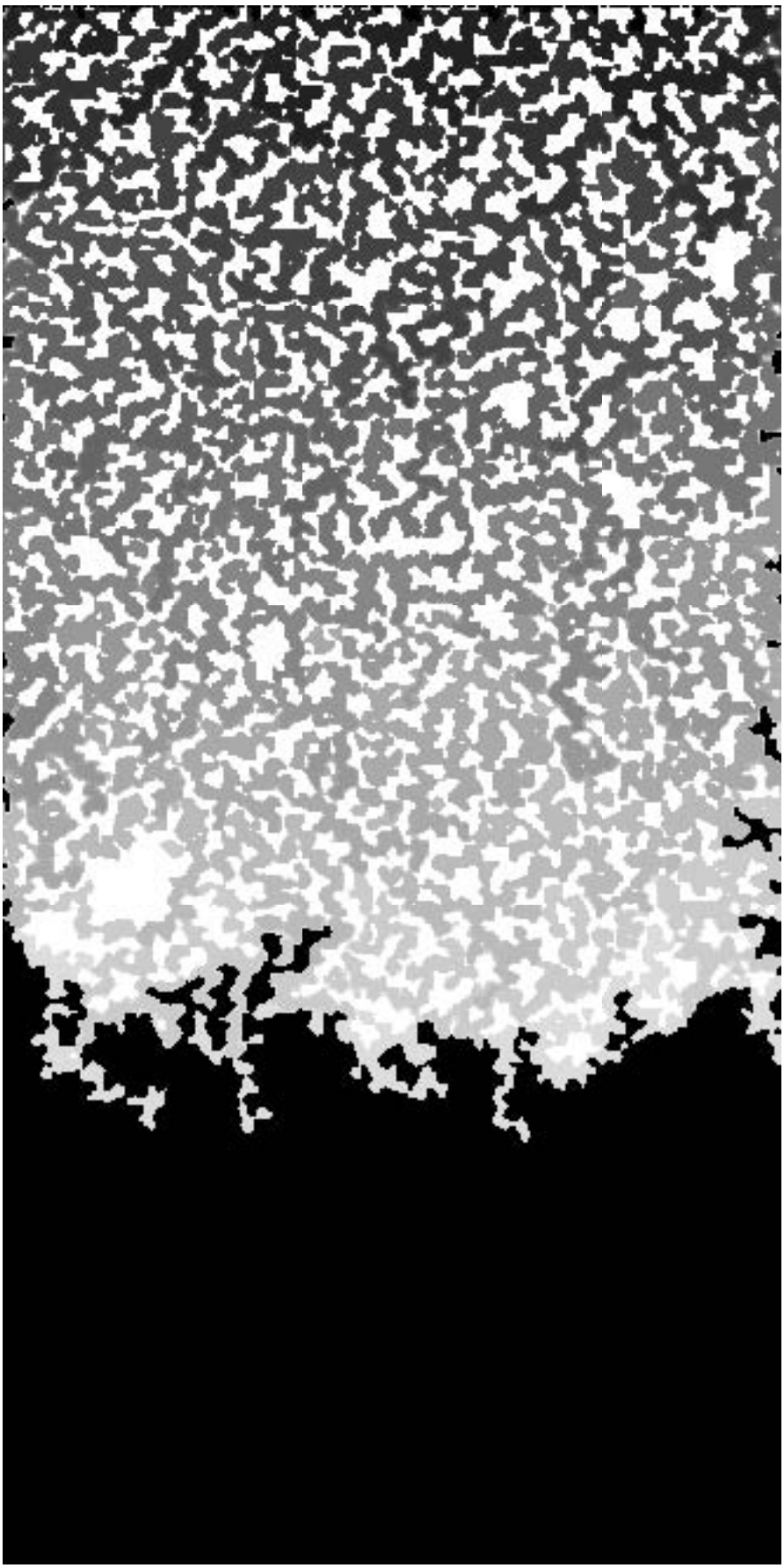

A36: Gravity-stabilized vertical invasion neglecting in-plane curvature, r_2 ($\alpha = 120$).

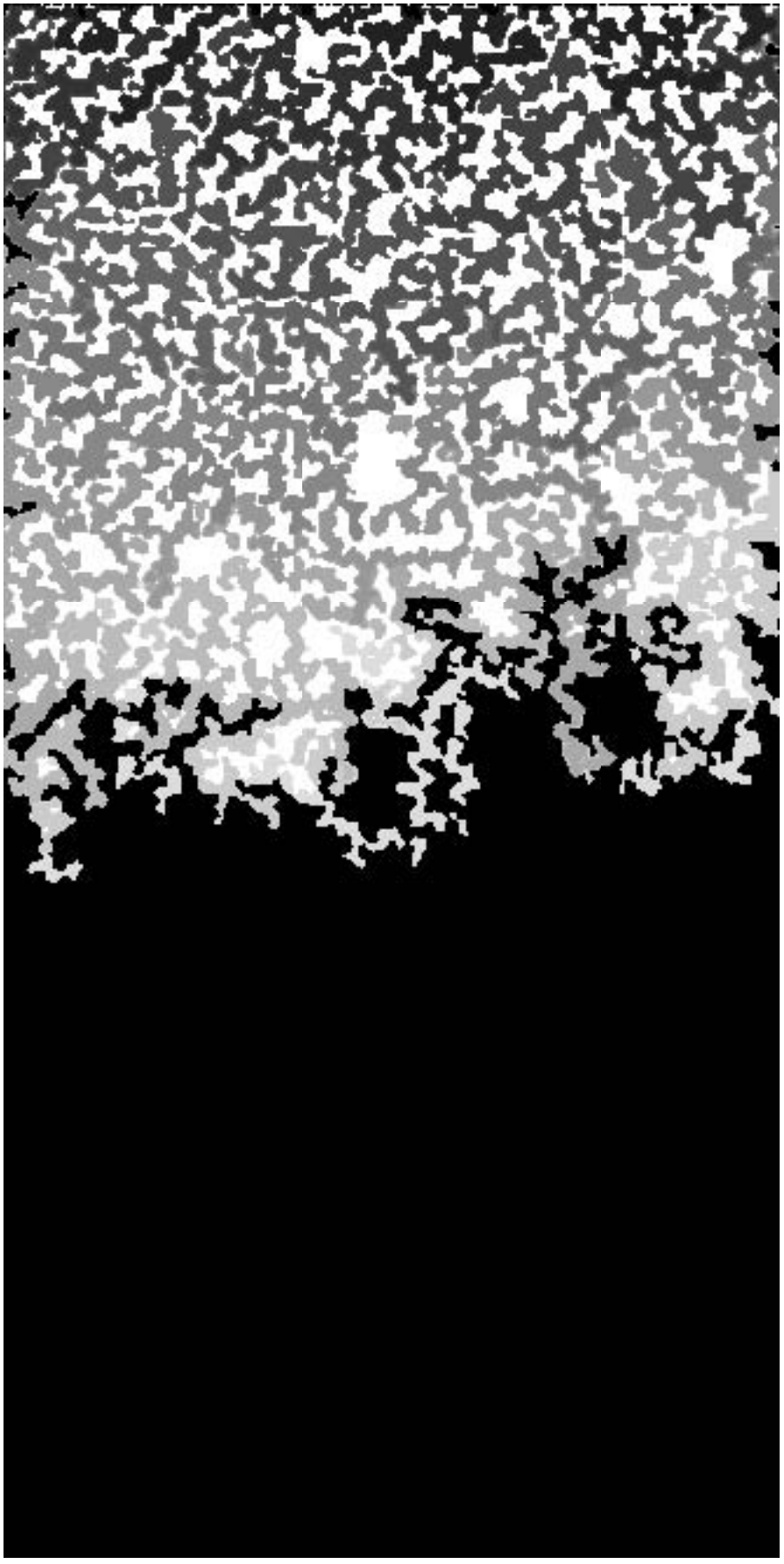

A37: Gravity-stabilized vertical invasion neglecting in-plane curvature, r_2 (α = 139).

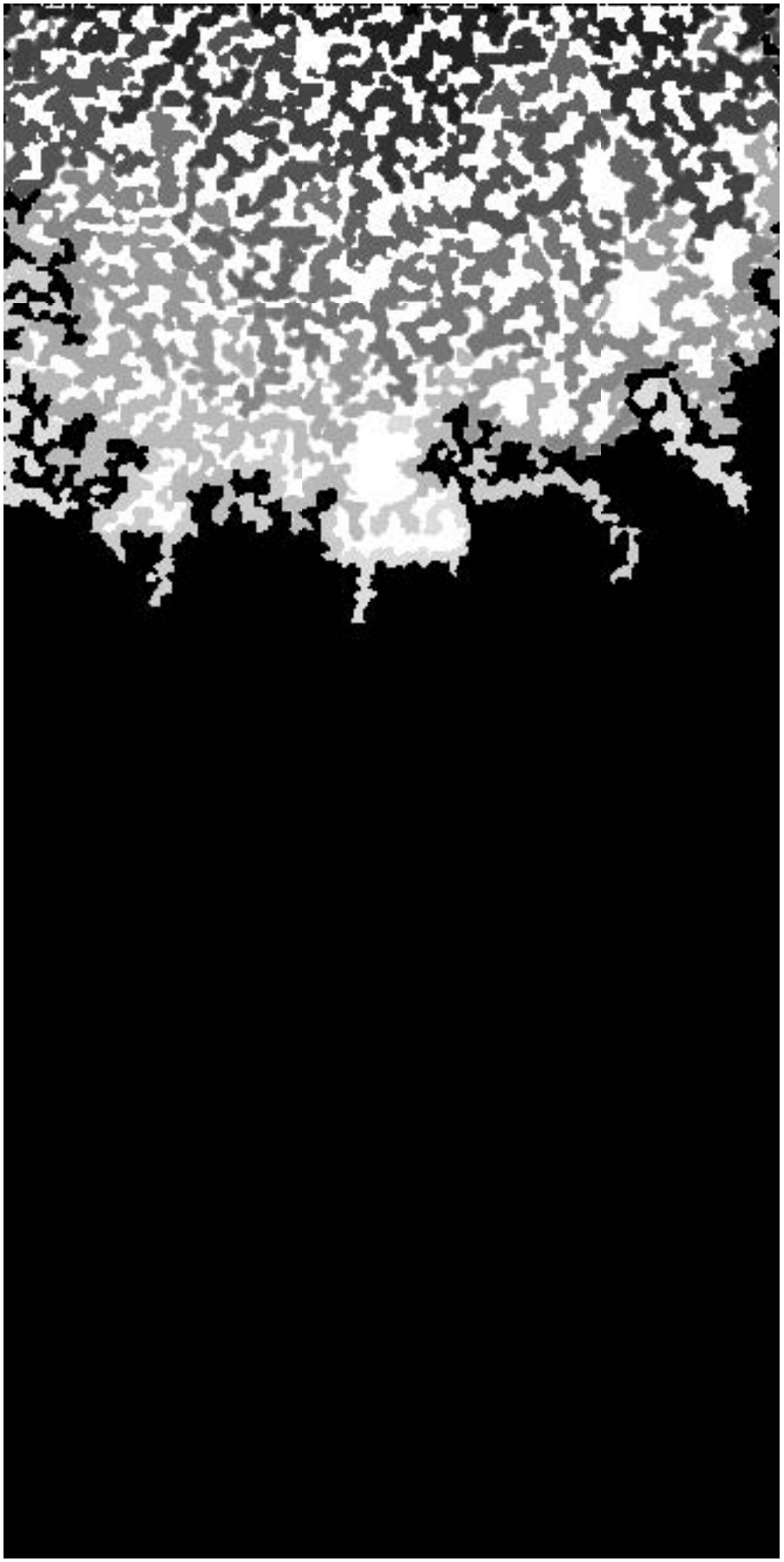

A38: Gravity-stabilized vertical invasion neglecting in-plane curvature, r_2 ($\alpha = 180$).

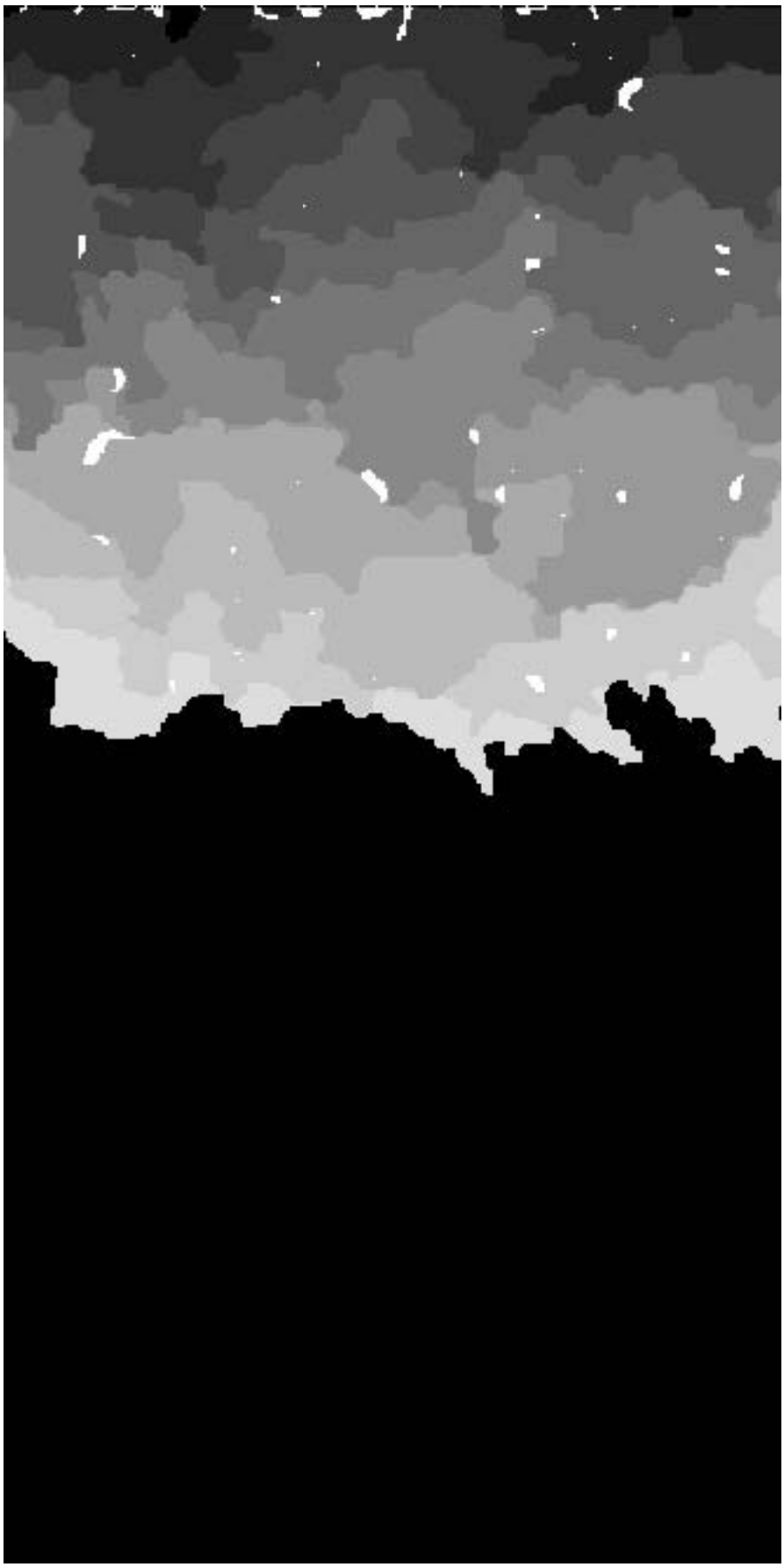

A39: Gravity-stabilized vertical invasion including in-plane curvature, r_2 ($\alpha = 0$)

A40: Gravity-stabilized vertical invasion including in-plane curvature, r_2 ($\alpha = 41$).

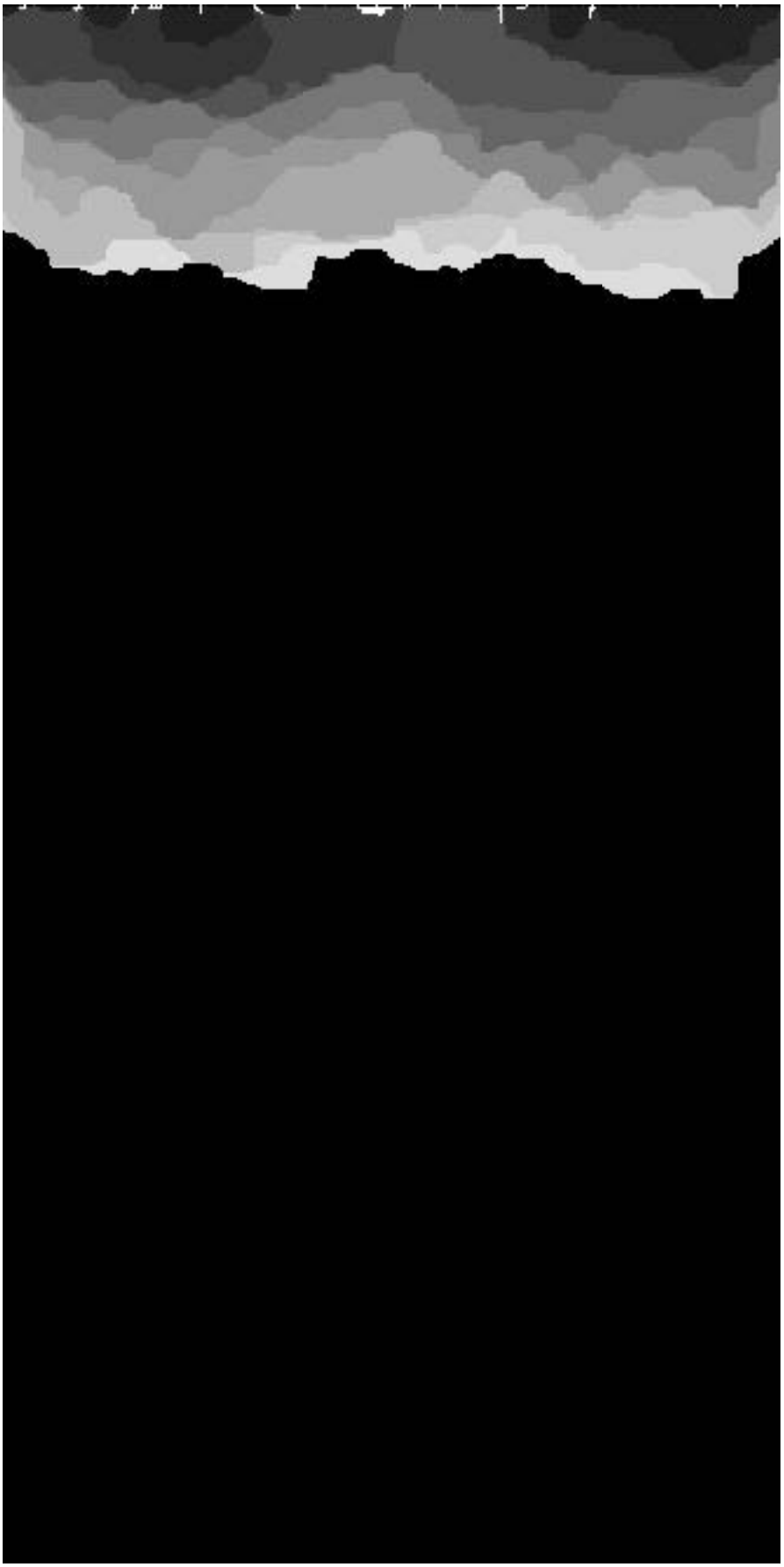

A41: Gravity-stabilized vertical invasion including in-plane curvature, r_2 ($\alpha = 60$).

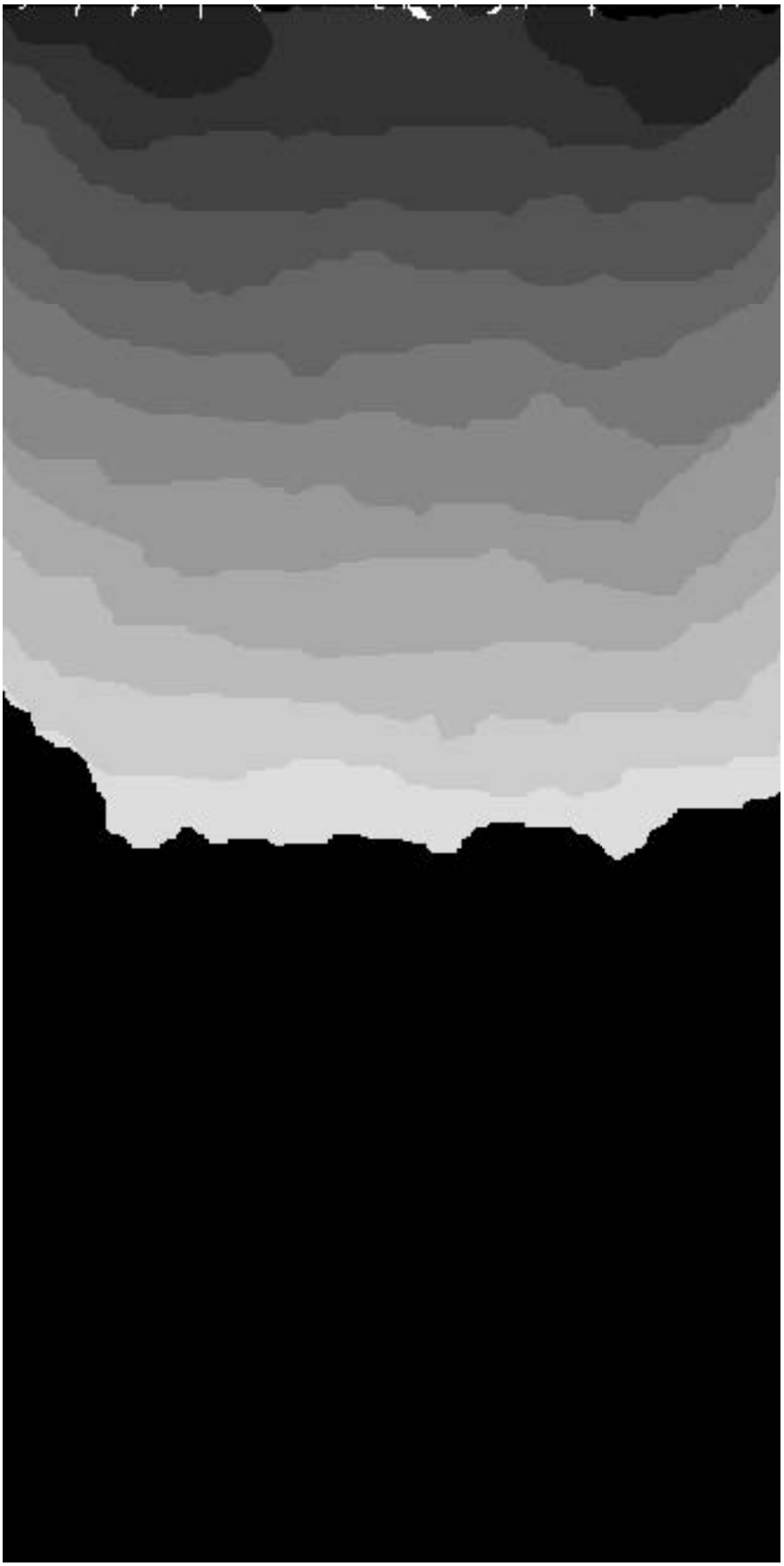

A42: Gravity-stabilized vertical invasion including in-plane curvature, r_2 ($\alpha = 76$).

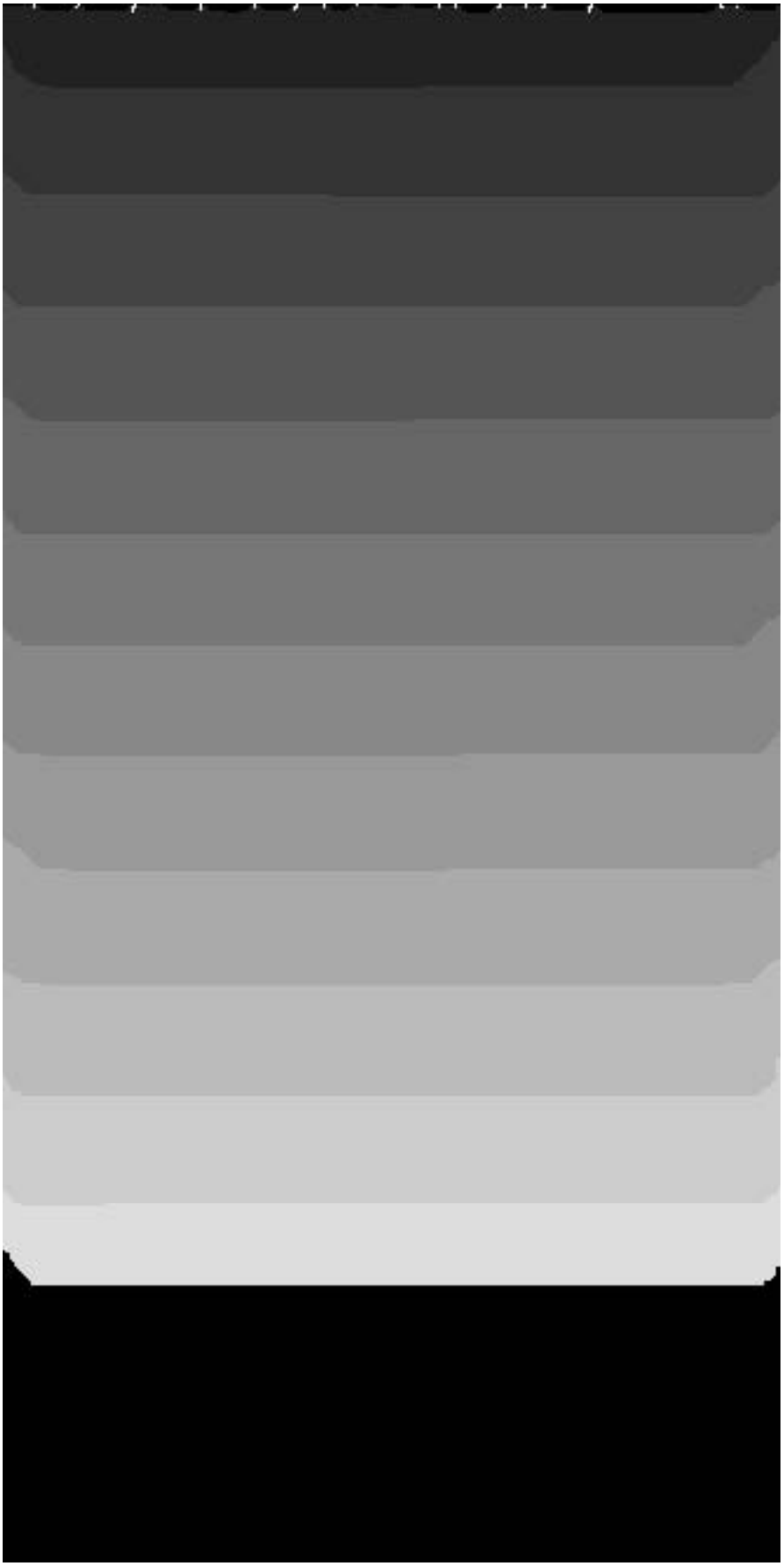

A43: Gravity-stabilized vertical invasion including in-plane curvature, r_2 ($\alpha = 90$).

A44: Gravity-stabilized vertical invasion including in-plane curvature, r_2 ($\alpha = 104$)

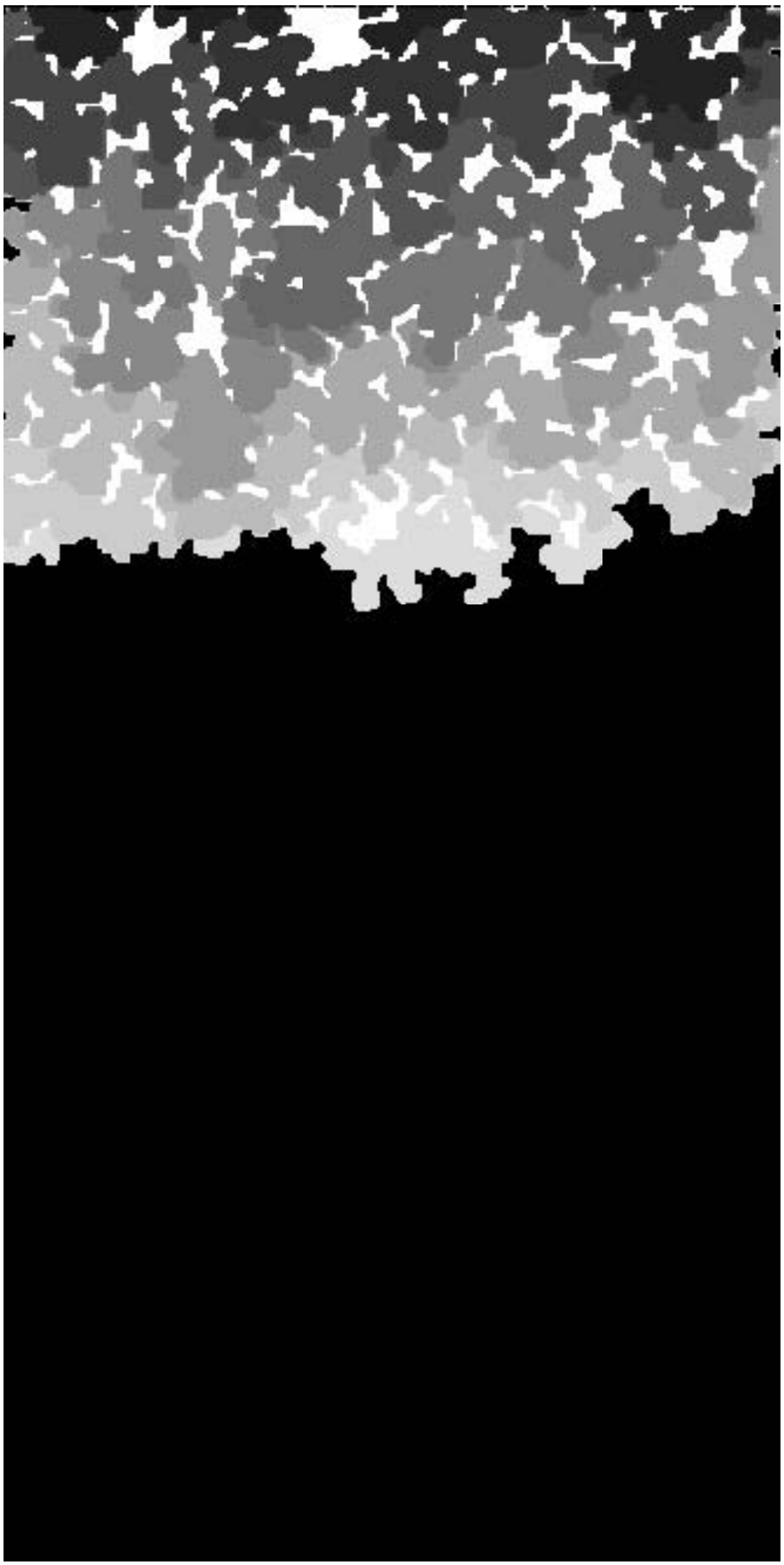

A45: Gravity-stabilized vertical invasion including in-plane curvature, r_2 (α = 120)

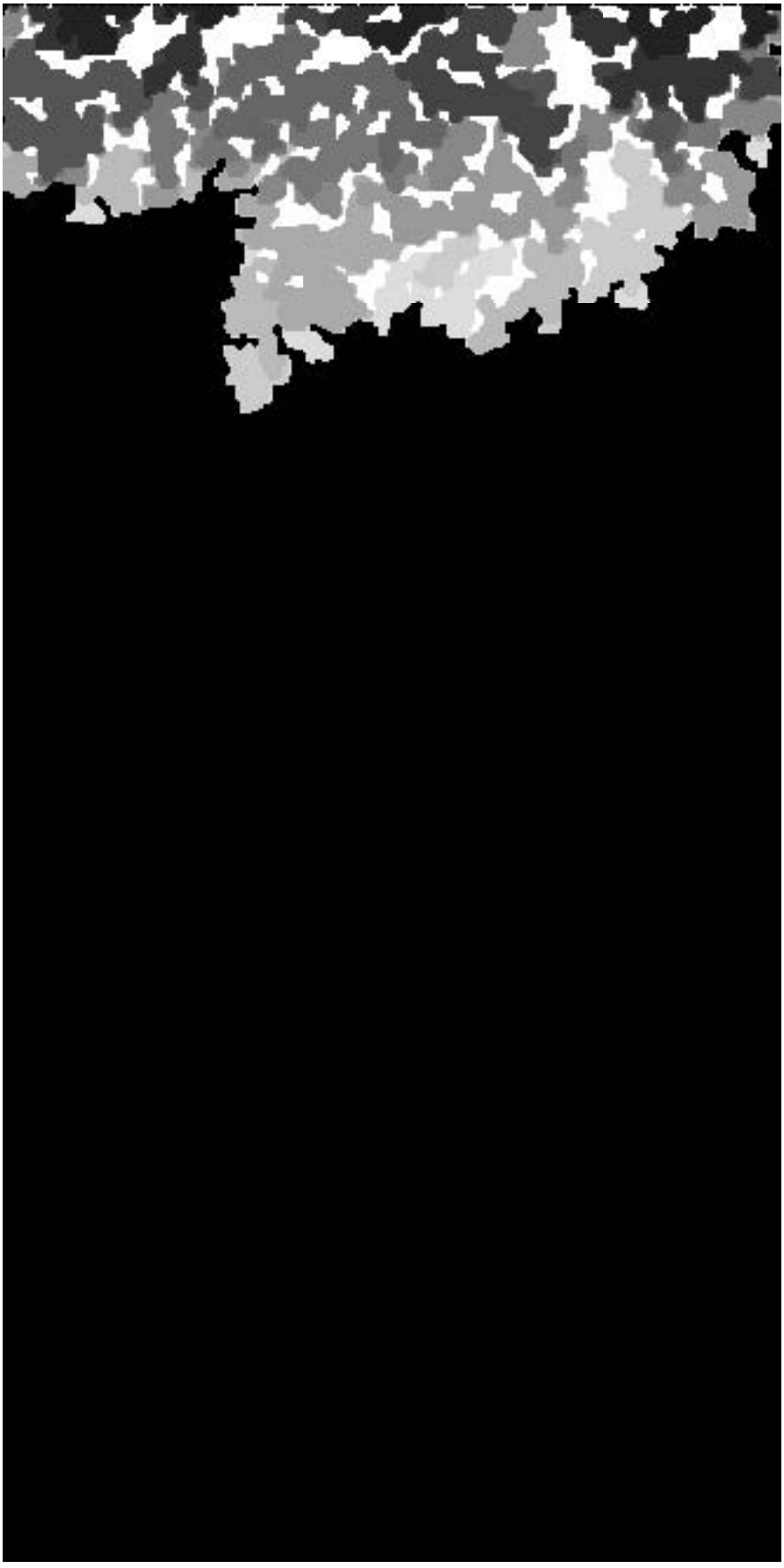

A46: Gravity-stabilized vertical invasion including in-plane curvature, r_2 (α = 139)

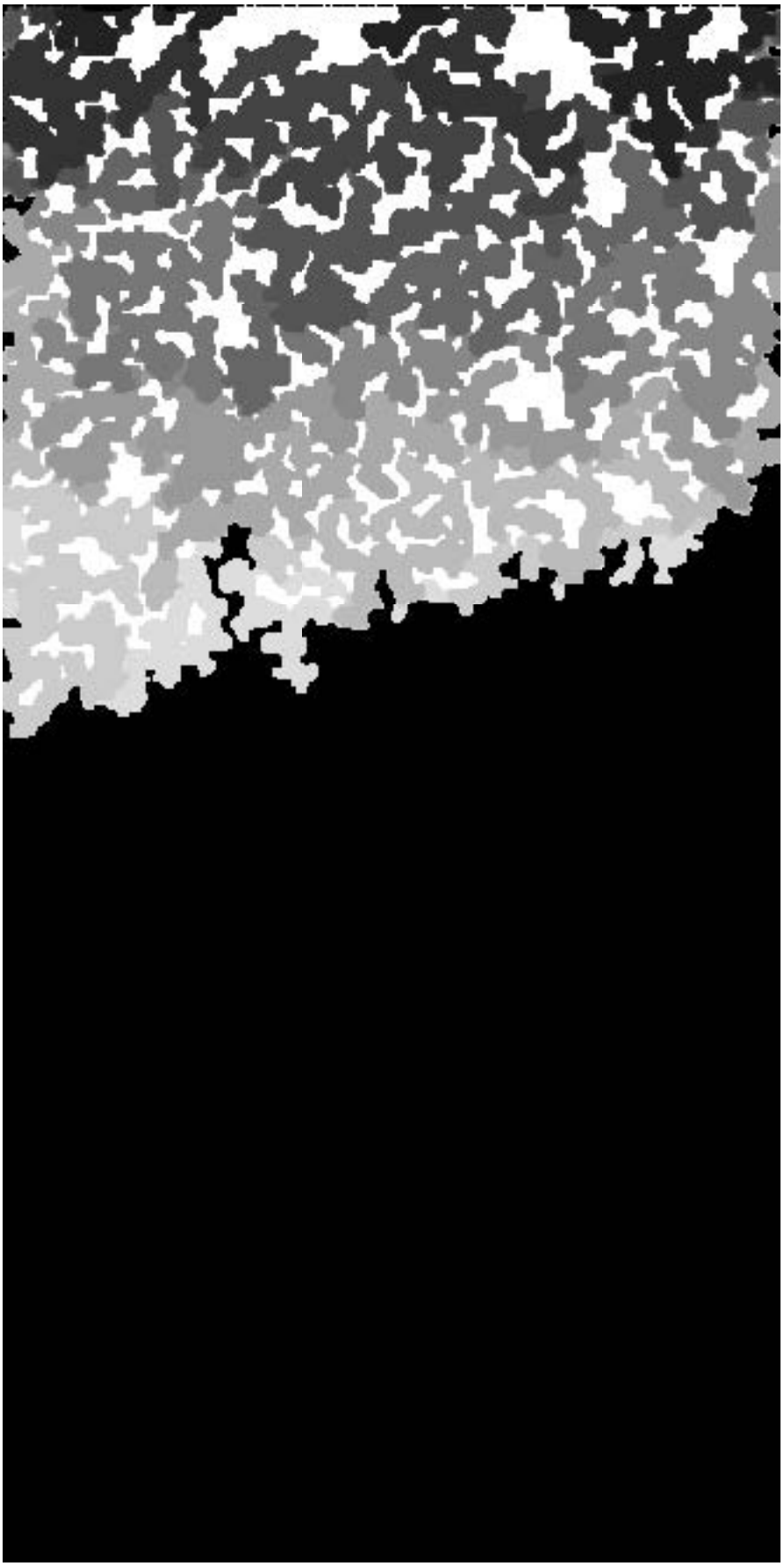

A47: Gravity-stabilized vertical invasion including in-plane curvature, r_2 ($\alpha = 180$).